공학박사 학위논문

Functional Multilayer Films with Controlled Nanostructures for *in vitro* Cell Studies

체외 세포거동 연구를 위한 기능성 다층박막의 나노구조 조절 및 분석

2013 년 8 월

서울대학교 대학원

화학생물공학부

장 영 선

Functional Multilayer Films with Controlled Nanostructures for *in vitro* Cell Studies

체외 세포거동 연구를 위한 기능성 다층박막의 나노구조 조절 및 분석

지도교수 차 국 헌

이 논문을 공학박사 학위논문으로 제출함

2013 년 4 월

서울대학교 대학원
화학생물공학부
장 영 선

장영선의 공학박사 학위논문을 인준함

2013 년 6 월

위 원 장 장 전 식 (인)
부 위 원 장 車 國 憲 (인)
위 원 조 건 한 (인)
위 원 남 과 민 (인)
위 원 황 석 연 (인)

Abstract

Functional Multilayer Films with Controlled Nanostructures for *in vitro* Cell Studies

Yeongseon Jang

School of Chemical and Biological Engineering

The Graduate School

Seoul National University

Functional polymer thin films are of great interest for diverse potential applications due to their excellent productivity and cost-efficiency. Thorough understandings on the relationship between structures and physicochemical properties of polymer thin films play pivotal roles in developing the films for the fine purpose. Among many different types of functional polymer thin films, the multilayer films with controlled nanostructures has been recently highlighted in many biomedical applications such as controlled release platforms, disease diagnosis platforms, and tissue engineering. Particularly, in order to develop such novel biomedical platforms based on the functional multilayer films, *in vitro* cell study has to be performed, which provides perspectives on regulating the cell behaviors.

In this thesis, we focus on the layer-by-layer (LbL) strategy for fine tuning of structures and properties of polymer thin films as well as for constructing polymer platforms for *in vitro* studies on metastatic cancer cell behavior. In particular, the external stimuli-triggered release

mechanism of polymer multilayer films has been systematically investigated, in terms of changes in internal structures and physicochemical properties, in order to establish the ground for designing the controlled release of target active materials from thin film coatings. Furthermore, the functionalization of multilayer films with controlled nanostructures has been carefully examined in the viewpoint of the control of cell-matrix or cell-cell interactions.

In Chapter 1, the control strategies for engineering internal structures and swelling properties of polymer multilayer films are introduced on the basis of the LbL deposition, because it has been the one of the most efficient methods for preparing functional multilayer platforms, taking advantage of various intermolecular interactions among paired species. The growth rates of bilayer thickness and the internal structures in multilayer films were greatly controlled by tuning the range of the intermolecular interactions between polymer chains (i.e., long-range electrostatic interactions or short-range hydrogen bonding) and by the film fabrication methods (i.e., dip- or spin-assisted LbL deposition). The internal structures of multilayer thin films in nanometer scale were systematically investigated by the neutron reflectivity (NR) measurements, as a function of LbL deposition techniques and the types of intermolecular interactions. Furthermore, it was demonstrated that the loop and tail conformations of partially charged weak PE chains preferentially capture water molecules within multilayer films as compared to fully charged and tightly bound PE chains with stretched conformations by NR along with quartz crystal microbalance with dissipation monitoring (QCM-D) measurements.

In Chapter 2, we have designed the controlled release platforms based on polyelectrolyte (PE) blend multilayer films to investigate the release mode and kinetics at the nanoscale level. The model blend multilayer films are composed of positively charged layers with weak PE (linear poly(ethylenimine), LPEI) and negatively charged blend layers with mixtures of

strong (poly(sodium 4-styrenesulfonic acid), PSS) and weak (poly-(methacrylic acid), PMAA) PEs. The blend multilayer films ($[LPEI/PSS:PMAA]_n$) with well-defined internal structure were prepared by the spin-assisted LbL deposition method. The changes in nanostructures and physicochemical properties of the blend multilayer films were systematically studied as a function of blend ratio by NR, ellipsometer, AFM, FT-IR spectroscopy, and QCM-D. Since PSS strong PEs serve as robust skeletons within the multilayer films independent of external pH variation, the burst disruption of pure weak PE multilayer films was dramatically suppressed, and the release kinetics could be accurately controlled by simply changing the PSS content within the blend films. These release properties of blend multilayer films form the basis for designing the controlled release of target active materials from surfaces.

In Chapter 3, we present the effect of molecular weight (MW) of PEs on the disintegration behavior of weak PE multilayer films consisting of LPEI and PMAA. The multilayer films prepared by the spin-assisted LbL deposition have well-ordered internal structures and also show the linear thickness growth behavior regardless of MWs of PMAA. The well-defined weak PE multilayer films were subject to disintegration into bulk solution when the electrostatic interactions between LPEI and PMAA layers were reduced by treatment at pH 2. However, we demonstrated the change in the disintegration mode and kinetics (i.e., from burst erosion to controlled surface erosion) as a function of MW of PMAA based on neutron reflectivity (NR) and quartz crystal microbalance with dissipation (QCM-D), revealing the correlation between the structural changes and the viscoelastic responses of the weak PE films upon pH treatment. Also, the unique swelling behavior as well as the significant increase in dissipation energy was monitored before the complete disintegration of the multilayer films containing high MW PMAA, which is believed to originate from their slow rearrangement kinetics within the film. We believe that the results shown in this study

provide chain-level understanding as to the MW-dependence on pH-triggered disintegration mechanism of weak PE multilayer films.

In Chapter 4, we have developed *in vitro* platforms for studying metastatic cancer cell behavior, based on the surface modification of LbL-assembled multilayer films with functional nanoparticles and biomolecules. The polymer multilayer platforms prepared by spin-assisted LbL deposition provide controlled surface charge and stable mechanical property in cell culture environments, which could offer easy surface modification with charged functional molecules while creating intimate cell-surface contacts. Gold nanoparticles (AuNPs) were employed to modify flat LbL surfaces and investigated the effect of nano-topographical cues on the metastatic cancer cell focal adhesion, shape and motility. Moreover, cellular signaling process with proteins in extracellular matrices (ECMs) was mimicked and analyzed by incorporating biomolecule-conjugated AuNPs onto LbL films. As a result, it is confirmed that the existence of nanotopographical features with a cell adhesion protein (fibroectin, Fn) is critical in inducing dramatic changes in metastatic cancer cell adhesion, protrusion, polarity and motility than the presence of the Fn on the flat multilayer surfaces. Also, the detachement signaling mediated by ephrinB3 was found to be more effective when the ephrinB3 were modified to the nanofeatured surfaces than flat surfaces. The results in this study would give insights on the basic understanding of tumor metastasis regulated by extracellular environmental signals.

In Chapter 5, we have developed novel multilayered co-culture platforms with nanoporous cellulose acetate (CA) membranes for efficient *in vitro* analysis of cell-cell communications. The CA films designed in this chapter have high number density of well-defined nanopores and unique natures of transparency and transferability in cell culture environments. The transparent, transferable and nanoporous (TTN) CA membrane platforms

allow for imaging and analyzing cells on each layer as well as mediating the paracrine communications between co-cultivated cells. The communications between human breast metastatic cancer cell (MDA-MB-231) and three different types of stromal cells [fibroblast (NIH-3T3), myoblast (C2C12), and human mesenchymal stem cell (hMSC)] via the TTN membrane were systematically investigated by cytokine and cell migration assays based on the high flexibility in stacking and destacking of the TTN platforms. The TTN membranes would address the issues from conventional membrane-separated cell co-culture platforms that lack the routes for cell-cell communications and direct cell-cell contact assay that does not offer the flexibility in studying cell-cell communications.

We strongly believe that the research work in this thesis as to the engineering of the nanostructures and physicochemical properties in polymer thin films could eventually contribute to explore new perspectives on functional multilayer films and could also open up new possibilities to design flexible and multifunctional structures for numerous biological applications such as controlled release platforms and *in vitro* disease cell assay platforms.

Keywords

Functional Polymer Thin Film(s), Multilayer Film(s), Nano-structure(s), Controlled Release, *in vitro* Cell Study, Cell-Extracellular Matrix Interaction(s), Cell-Cell Communication(s), Neutron Reflectivity, Quartz Crystal Microbalance with Dissipation

Student Number: 2008-21109

Contents

List of Tables

List of Figures

List of Schemes

Chapter 1.

Engineering Intermolecular Interactions for Controlling Nanostructures in Polymer Multilayer Thin Films

1.1. Introduction

The layer-by-layer (LbL) assembly technique is one of the most versatile methods to prepare multifunctional polymer thin films taking advantage of various intermolecular interactions among paired species. The concept of building up multilayer films has first been suggested by Iler, who reported the preparation of multilayer films by combining positively and negatively charged colloidal particles.[11] Some decades later, Decher and coworkers realized multilayer films with oppositely charged polyelectrolytes.[1,2] Afterward, an explosive number of publications dealing with the LbL multilayer films have emerged ranging from the basic principles addressing LbL deposition mechanism to numerous potential applications for the last two decades. The general introduction of the LbL assembly as well as various applications of the LbL-assembled multilayer thin films has already been well described in many reviews.[3-10]

Conventional LbL assembly is based on the dipping method (i.e., dip-assisted LbL assembly). In the case of the dip-assisted LbL assembly, a substrate is alternatively immersed into two different aqueous solutions containing pairing polymers, with rinsing steps in between. In this case, adsorbed species or polymeric chains diffuse to and adsorb on the substrate from aqueous solution mediated by various intermolecular interactions, followed by the slow molecular rearrangement on the surface (Scheme 1A). The conventional LbL

assembly based on the solution dipping has recently been extended to spin-assisted,[12] spray-assisted,[13] and microfluidic-assisted LbL assembly.[14] The alternative LbL deposition methods further expand control parameters of the conventional dip-assisted LbL assembly. In addition, detailed LbL deposition methods were also known to play an important role in terms of controlling final film characteristics. For example, the spin-assisted LbL deposition method has been of particular interest as opposed to the conventional dip-assisted LbL deposition because the spin method offers several merits such as drastically reduced process time for the preparation of well-defined multilayer films with highly ordered internal structure as well as minimal solvent usage and uniform surface morphology and properties (Scheme 1B).

The main driving forces to prepare multilayer thin films based on the LbL assembly are various molecular interactions. Those interactions are not simply limited to the electrostatic interactions but other intermolecular interactions such as hydrogen bonding, covalent bonding, donor-acceptor interaction (charge-transfer interaction), π-π interactions, and hydrophobic interactions have also been tested to prepare the multilayer films. These diverse intermolecular interactions also enable us to utilize functional nano-objects such as polymeric micelles, nanoparticles, and biomolecules (such as DNA, proteins, polysaccharides to name a few) to prepare functional LbL multilayer films. Apart from intermolecular interactions for LbL deposition, intrinsic properties of adsorbing species such as chemical structures, chain length and stiffness and physical and chemical characteristics of suspending medium such as pH and the amount and type of salts used have also been identified as important process parameters to control the multilayer formation.[15] This is to say that important features of LbL films such as thickness increment could be finely tuned by the adsorption conditions such as ionic strength, temperature, solution pH, solvent polarity and so on in addition to the range of interactions for a selected intermolecular interaction. Furthermore, the correlation between internal structure and functional properties of LbL multilayer films has keenly been

considered in order to design stimuli-responsive surfaces and/or novel polymeric platforms for diverse applications.[16]

In this study, we have investigated the effect of LbL deposition techniques and the types of intermolecular interactions on the multilayer growth behavior as well as the film internal structures. Based on the neutron reflectivity (NR) measurements which are advantageous for the investigation of buried structure and interfacial roughness in polymer multilayer films which has a weak electron density contrast between layers, we have further monitored relative humidity (RH)-driven changes in the film internal structures and absorption profile of water molecules into films as a function of types of polyelectrolyte (PE), along with quartz crystal microbalance (QCM-D) experiments for the analysis on the water absorption mass.

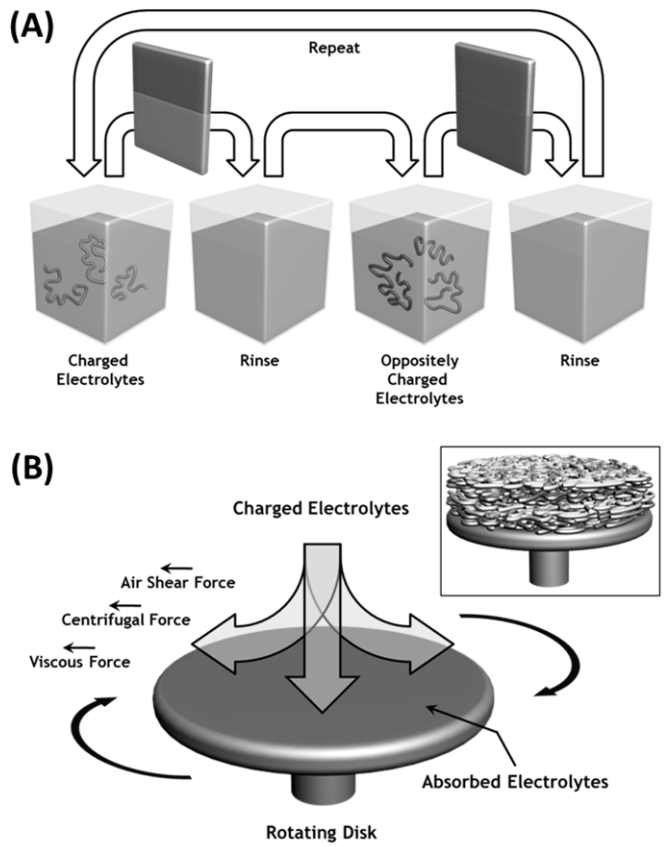

Scheme 1.1. Schematic representation on (A) dip-assisted Layer-by-Layer (LbL) deposition and (B) Spin-Assisted LbL deposition.

(illustrated by Mr. Jeongyeon Han)

1.2. Experimental Section

Materials. Poly(allylamine) hydrochloride (PAH, M_w = 70,000 g/mol, Aldrich), Poly(acrylic acid) (PAA, M_w = 100,000 g/mol, 30 wt% aqeous solution, Aldrich), Poly(ethylene oxide) (PEO, M_w = 4,000,000 g/mol, Aldrich), poly(methacrylic acid) (PMAA, M_w = 15,000 g/mol, 35 wt% aqueous solution, Polysciences), poly(sodium 4-styrenesulfonate) (PSS, M_w = 70,000 g/mol, Aldrich), deuterated PSS (d-PSS, M_n = 41,500 g/mol, Polymer Source) and PMAA (d-PMAA, M_n = 40,000 g/mol, Polymer Source) were used for the preparation of multilayer thin films without further purification. Silicon wafers, CaF_2 round crystal windows (Sigma Aldrich) and Au sensor crystals (QSX 301, Q-Sense) were used as substrates to build blend multilayer films for further characterization. Prior to the multilayer deposition, all the substrates were initially cleaned with piranha solution (mixtures of 70 vol % H_2SO_4 and 30 vol % H_2O_2) for 20 min at room temperature to remove any organic remnants and washed thoroughly with DI water, followed by drying under nitrogen stream. All the polymer solutions were prepared by dissolving polymers in deionized water with concentrations of 0.01 M based on the repeat units. By adding 1M HCl or 1M NaOH, the pH of polymer solutions was adjusted to the desired values.

Fabrication of Polymer Multilayer Thin Films. The polymer multilayer films, $[PAH/PAA]_n$, $[PEO/PAA]_n$, $[PAH/PMAA]_n$, $[PAH/PSS]_n$, were prepared by the dip-assisted or the spin-assisted layer-by-layer (LbL) deposition method. In the case of dip-assisted LbL deposition, the substrates first immersed into the positively charged polyelectrolyte (PE) solution (PAH solution) or the polymer solution containing hydrogen-bonding accepting groups (PEO solution) for 10 min and then immersed into two rinse baths of water for 2 min. Following this steps, the substrate was dried by gentle stream of nitrogen gas. The substrate was then immersed into the negatively charged PE or the hydrogen-bonding donor-containing

polymer solution (PSS, PMAA or PAA solution) followed by the same rinse and purging steps as mentioned above and all steps were repeated until the desired number of bilayers was obtained. In the case of spin-assisted LbL deposition, the multilayer films with different pair of polymers were also prepared on the piranha-treated hydrophilic substrates, with a spin-rate of 3000 rpm for 30 sec for each deposition, followed by two consecutive washing spin steps to remove excess polymers.

Characterization on the Polymer Multilayer Thin Films. The total film thicknesses were measured by a variable-angle multi-wavelength ellipsometer (Gaertner L2W16C830, Gaertner Scientific Corp. UV/Vis absorption spectra to characterize the growth behavior of blend multilayer films were obtained by a PerkinElmer Lambda 35 UV/Vis spectrophotometer. Every blend multilayer film was prepared onto quartz slides for UV/Vis measurements. The internal structures of the blend multilayer films (in-plane average coherent scattering length density (SLD) profile, surface and interface roughnesses, and total film and interlayer thicknesses) were characterized by neutron reflectivity (NR) measurements. The NR measurements were conducted at the NG7 horizontal reflectometer at National Institute of Standards and Technology (NIST) Center for Neutron Research (NCNR) using wavelength (λ) of 0.475 nm. Angular divergence of the beam was varied through the reflectivity measurement to get a constant footprint and a relative q_z resolution ($\Delta q_z/q_z$) ~ 0.04 where $q_z = 4\pi\sin\theta/\lambda$ and θ is the incident and exit angle of the beam with respect to plane of the sample. For all the samples NR data were collected up to $q_{z,max}$ of 0.15 $Å^{-1}$. The NR experiments were performed in a closed chamber with supersaturated salt solutions (LiBr, $CaCl_2$, NaBr, NaCl and KNO_3) to keep RH close to 6, 29, 58, 75 and 98 %, respectively. The swelling behavior of multilayer films was monitored by a quartz crystal microbalance with dissipation monitoring technique (QCM-D, D300, Q-Sense AB) measurements. The AT-cut

quartz crystal covered with gold electrodes has fundamental resonant frequency of 5 MHz (QSX 301, Q-Sense AB). The applied voltage is sequentially pulsed across the Au sensor crystal, allowing the shear wave to dissipate as well as the simultaneous measurements of absolute dissipation and absolute resonant frequency of the crystal for all four overtones (n = 1, 3, 5 and 7, i.e., 5, 15, 25 and 35 MHz). These overtones were used to characterize the viscoelastic properties of multilayer films adsorbed onto Au sensor crystals. . Since Δf_1 and ΔD_1 were typically noisy due to insufficient energy trapping, the 3rd overtone $\Delta f_3/3$ (Hz) were compared among the multilayer films with different blend ratios. The sample chamber was maintained at a constant temperature of 25.1 ± 0.1 °C for all measurements. Furthermore, to control relative humidity (RH) in the QCM-D chamber, humid air from supersaturated salt solutions (LiBr, $CaCl_2$, NaBr, NaCl and KNO_3) was injected to inlet of QCM-D chamber with air flow rate of 10 ml/min.

1.3. Results and Discussion

1.3.1. Effects of Deposition Techniques and Types of Molecular Interaction on the Polymer Adsorption into a Multilayer Film

The driving forces of the layer-by-layer (LbL) assembly to prepare multilayer thin films are based on various types of intermolecular interaction such as the electrostatic interaction, hydrogen bonding, covalent bonding, charge-transfer interaction, π-π interaction, to name a few.[17-18] These intermolecular interactions are generally separated into two groups: short range and long range attractions according to the operation distance between molecules. In this regard, the electrostatic interaction between oppositely charged polyelectrolyte (PE) chains is based on the long-ranged and strong charge-charge interaction ($U(r) \sim 1/r$), which has *Bjerrum length* in water at 298 K of 0.71 nm.[19] On the other hand, the hydrogen bond is considered as a relatively short-ranged and moderate intermolecular forces between molecules. The typical equilibrium distance between H and O atom in water is at 0.18 nm, which differs both from the H-O covalent distance (0.1 nm) as well as van der Waals distance (0.26 nm).[20]

Depending on the intermolecular interaction types used in the LbL assembly, the LBL deposition methods play an important role with respect to the final film characteristics. In particular, surface and interface properties of multilayer films can be tuned by the types of LbL deposition techniques. Therefore, to investigate the effect of LbL deposition methods on the bilayer thickness growth behavior as a function of intermolecular interactions, the growth behavior of the multilayer films based on electrostatic interactions or hydrogen bond was monitored when they are prepared by the dip and the spin-based LbL deposition.

First of all, we used poly(allylamine hydrochloride) (PAH) and poly(acrylic acid) (PAA) to monitor the growth behavior of multilayer films based on the electrostatic interaction as a function of the LbL deposition methods. The PAH and PAA are weak PEs of which charge density can be controlled by adjusting solution pH. PAH is a positively charged PE containing primary amine groups of which the pKa value is around 8, while PAA is a negatively charged PE containing carboxylic groups of which pKa value is around 4-5. Therefore, both of PAH and PAA are fully charged at deposition condition of pH 6.5, the $[PAH/PAA]_n$ (n: number of bilayers) multilayer films can be constructed based on the strong electrostatic interactions. As shown in Figure 1.1A, the spin-assisted LbL assembly shows the faster thickness growth as compared to the dip-assisted LbL assembly. The reason why the spin-assisted [PAH/PAA] multilayer films based on the electrostatic interaction have the thicker bilayers is that the spin-coating method provides the additional external forces for adhesion of PE chains (i.e., centrifugal force, air shear force, viscous force) that are helpful to suppress the inter- and/or intra- charge repulsion of same charged molecules.[12]

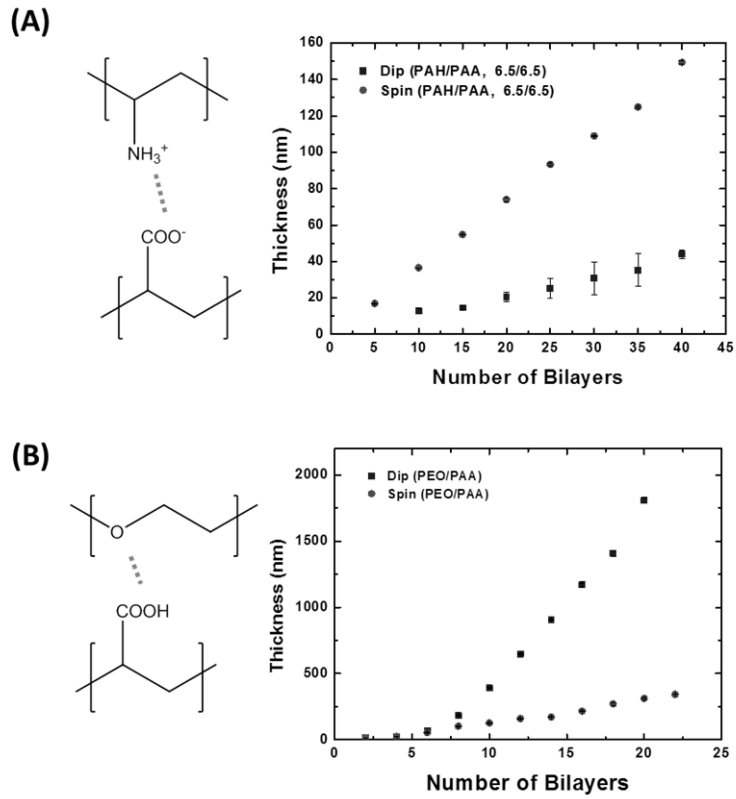

Figure 1.1. Growth curves for bilayer thickness of the multilayer films based on (A) electrostatic interactions and (B) hydrogen bond, prepared by the dip (blue square) and the spin (red circle) –assisted LbL deposition method.

On the other hand, poly(ethylene oxide) (PEO) and protonated PAA can construct the LbL multilayer films based on the hydrogen bond. In this case, the dip-assisted LbL assembly makes thicker bilayers of $[PEO/PAA]_n$ multilayer films than the spin-assisted LbL method (Figure 1.1B). Since the hydrogen bond is very short-range interaction and the energy of attraction strongly depends on the separation distance between two molecules,[20] the polymer chains which are very close to each other can only make the hydrogen bond. In this regard, the dip-assisted LbL deposition provides enough diffusion time for PEO and PAA pair to be self-assembled into a multilayered structure making the strong hydrogen bond between them in polar solvent (i.e., water), while the spin-assisted LbL method interrupts the efficient hydrogen bonding due to fast washing of solvents with strong external forces.

Not only the types of intermolecular interactions but the charge density of each PE chain has a great effect on the multilayer growth depending on the LbL deposition techniques, as shown in Figure 2. The [PAH/PAA] multilayer films are prepared at different solution pH conditions, pH 6.5/6.5 or pH 7.5/3.5, to control the charge densities of both of PAH and PAA, and their bilayer growths are monitored as a function of the LbL deposition methods. In the case of using fully charged PAH (pH 6.5) and PAA (pH 6.5) chains which have stretched conformations due to their intra- and inter-chain repulsions, the spin-assisted LbL multilayer film shows thicker bilayer as compared with the dip-assisted LbL assembly because the strong charge repulsion can act strongly as a desorption force during the dip-assisted LbL (Figure 1.2A). It originates from the fast elimination of water molecules during spinning, and the fast water removal facilitates attractive interactions between opposite charged PE layers and minimizes unfavorable long-range repulsive interactions among adsorbing same charged moieties. On the other hand, the thicker [PAH/PAA] multilayer films are constructed by the dip-assisted LbL assembly as compared to the spin-based method, with partially charged

weak PEs which have loopy and coiled conformations in an aqueous environment (Figure 1.2B). In addition, it is clearly noted that the bilayer thickness growth of dip-assisted LbL films is highly dependent on the charge density of PE chains while the spin-assisted LbL films demonstrate similar growth rate as compared to the dip-assisted case. This result indicates that loopy and tailed conformations of partially charged PE chains strongly affect the thickness growth in aqueous environment during dip-assisted LbL deposition on the contrary to spin-assisted LbL deposition.

It is clearly noticed that the types of intermolecular interactions as well as the conformation of polymer chains have a strong influence on the thickness growth of multilayer films, demonstrating the different adsorption behavior depending on the LbL deposition techniques. However, the internal structures of multilayer films are need to be further investigated to obviously demonstrate the adsorption mechanism of different polymer chains at different deposition conditions, especially by monitoring the interfaces of the multilayered structures. Neutron reflectivity (NR) is the most powerful technique to monitor internal structures of the polymer multilayer films.

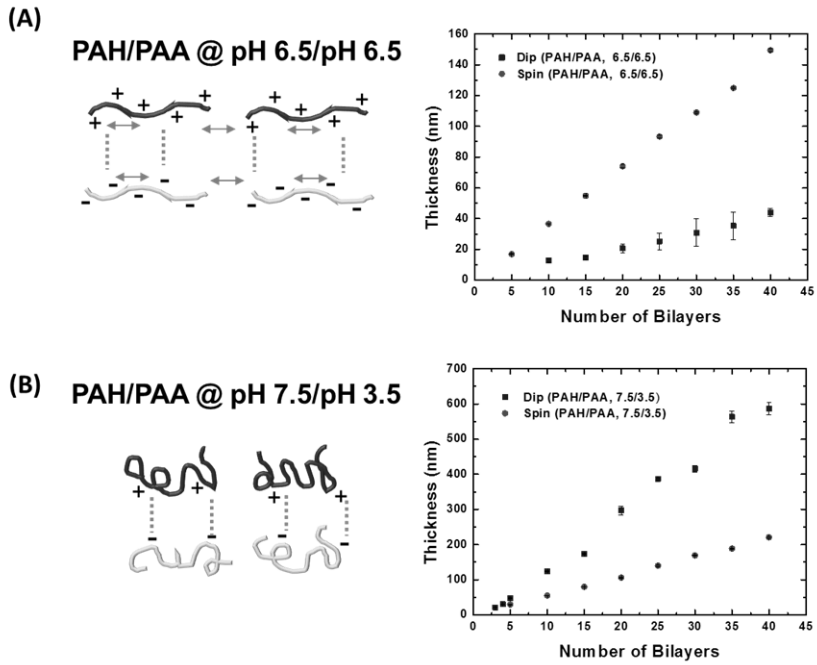

Figure 1.2. Growth curves for bilayer thickness of the [PAH/PAA] multilayer films prepared at (A) pH 6.5/pH 6.5 (fully charged) and (B) pH 7.5/ pH 3.5 (partially charged), by the dip (blue square) and the spin (red circle) –assisted LbL deposition method.

1.3.2. Investigation on the Internal Structures of Polymer Multilayer Thin Films by Neutron Reflectivity (NR)

NR is a neutron diffraction technique to measure the internal structure of thin films, as a complementary technique with X-ray reflectivity (XRR) and ellipsometry. The NR monitoring provide valuable information including polymer and surfactant adsorption, structure of thin film based on the magnetic systems, biological membranes, and so on. Since the NR is sensitive to the difference in coherent scattering length density (SLD) while the XRR is sensitive to electron density difference, NR is more advantageous for the investigation of buried structure and interfacial roughness in polymer multilayer films which has a weak electron density contrast between layers. The strong neutron scattering contrast between different isotopes of hydrogen and deuterium is exploited to inscribe layering features of interest within a PE multilayer film.[21-22]

The multilayer films containing strong or weak PEs are prepared by the dip- or spin-assisted LbL deposition and the internal structures of the films are monitored by NR.

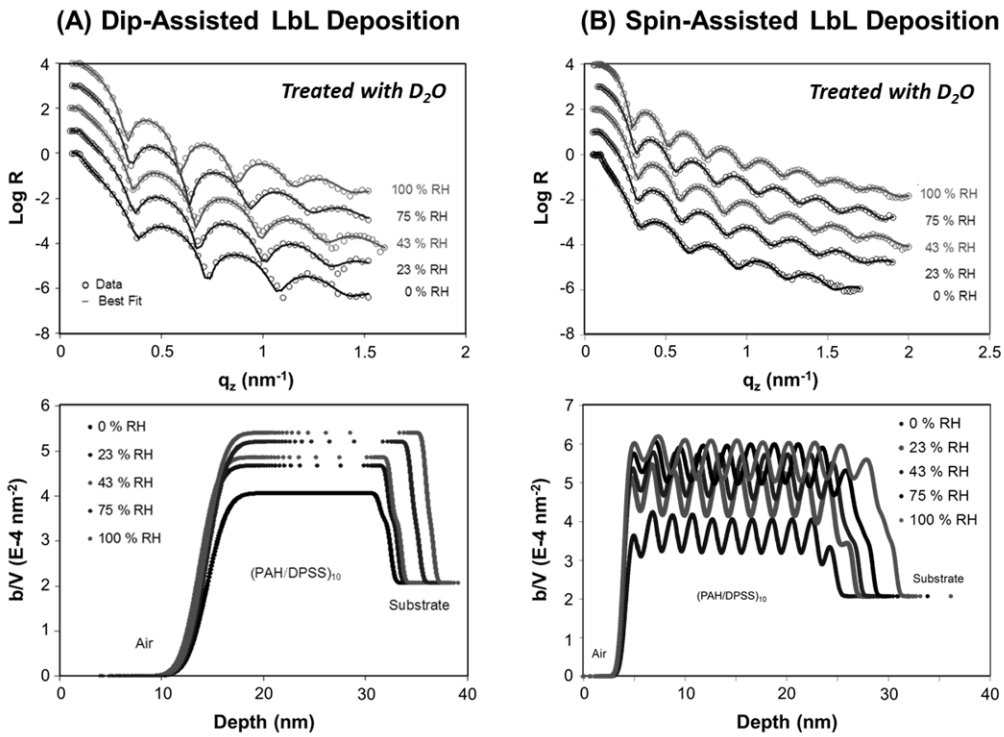

Figure 1.3. Neutron reflectivity (NR) curves with best fits and scattering length density (SLD) profiles of the multilayer films, $[PAH/d\text{-}PSS]_{10}$, prepared by (A) the dip-assisted and (B) the spin-assisted LbL deposition. The changes in the internal structure of model multilayer films were monitored as a function of relative humidity (RH) by NR.

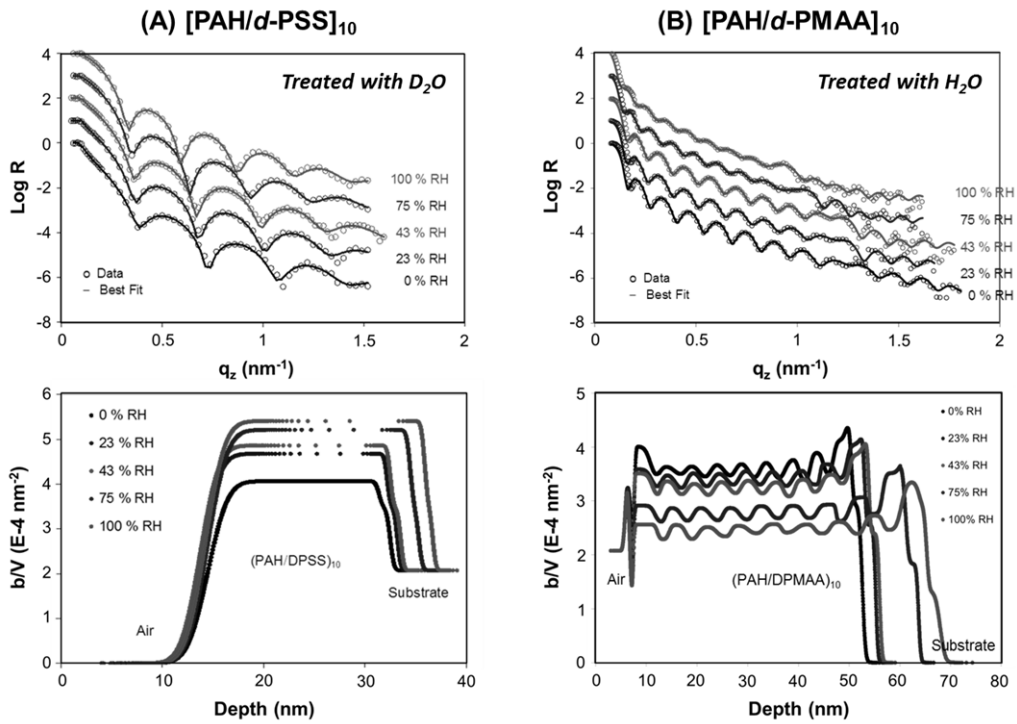

Figure 1.4. NR curves with best fits and scattering length density (SLD) profiles of the multilayer films, (A) [PAH/*d*-PSS]$_{10}$ and (B) [PAH/*d*-PMAA]$_{10}$ prepared by the dip-assisted LbL deposition. The changes in the internal structure of model multilayer films were monitored as a function of relative humidity (RH) by NR.

The multilayered structures of dip-assisted LbL films are hardly monitored by NR due to chain-chain interdigitation between adjacent layers and surface roughness, as compared to other LbL deposition such as spin- or spray-based methods. As shown in Figure 1.3A, the multilayer film prepared with strong polyelectrolyte (*d*-PSS) yields the uniform density profiles in entire film thickness because it is assembled in dipping condition, which enables the interlayer mixing during deposition. In the internal structures of the spin-assisted [PAH/*d*-PSS]$_{10}$ film (Figure 1.3B), it is found that the interdigitating behavior of PSS is rather prohibited owing to other driving forces such as air shear, viscous and centrifugal forces for polymer adsorption. This enhanced intermixing of strong PE (PSS) between the adjacent layers makes the internal layers of the film more compactly bounded with each other and thus serves as the strong skeleton to the external-stimuli such as pH changes or RH as compared to weak PE containing films. However, the [PAH/*d*-PMAA]$_{10}$ weak PE multilayer film shows well-defined internal structures with sharper interfaces than the [PAH/*d*-PSS]$_{10}$ film even when prepared by the conventional dip-assisted LbL deposition (Figure 1.4). The increases in total film thickness (%) are calculated by normalizing the difference in the film thickness measured at RH 100 % and RH 0 % to the dried thickness of RH 0 % condition. As the results, the [PAH/*d*-PSS]$_{10}$ film was increased around 28 % but the [PAH/*d*-PMAA]$_{10}$ film was swollen up to 38 %. More interestingly, it is found that the [PAH/*d*-PSS]$_{10}$ film swell uniformly like monolayer while water molecules preferentially segregate to air and substrate sides in the case of the [PAH/*d*-PMAA]$_{10}$ film. To monitor the swelling behavior of [PAH/*d*-PMAA]$_{10}$ film without disruption of well-defined SLD profiles in the direction normal to the surface, H_2O vapor was used instead of D_2O. Consequently, the broadening and the decrease in the SLD peaks is monitored especially at air and substrate sides due to preference of molecules absorption in free carboxylic groups at the air surface as well as buried water molecules within multilayer films.

In order to investigate the effect of PE types on the swelling behavior of multilayered film in more detail, the blended $[PAH/PSS_{50}:d\text{-}PMAA_{50}]_{10}$ multilayer film was monitored by NR as a function of RH (Figure 1.5). Incorporation of 10 wt % of PSS into the film significantly perturbs the well-defined *d*-PMAA density profiles and the intermixing is getting remarkable as the number of bilayers is increased. Accordingly, there is a gradient in swelling of the blend PE multilayer films and more water molecules are bounded at the substrate sides rather than toward the surface sides which contain more PSS chains. From the results of NR experiments, it is elucidated that weakly charged PMAA chains which have many free carboxylic groups can increase the extent of water binding site, maintaining their loops and tails structures within the films.

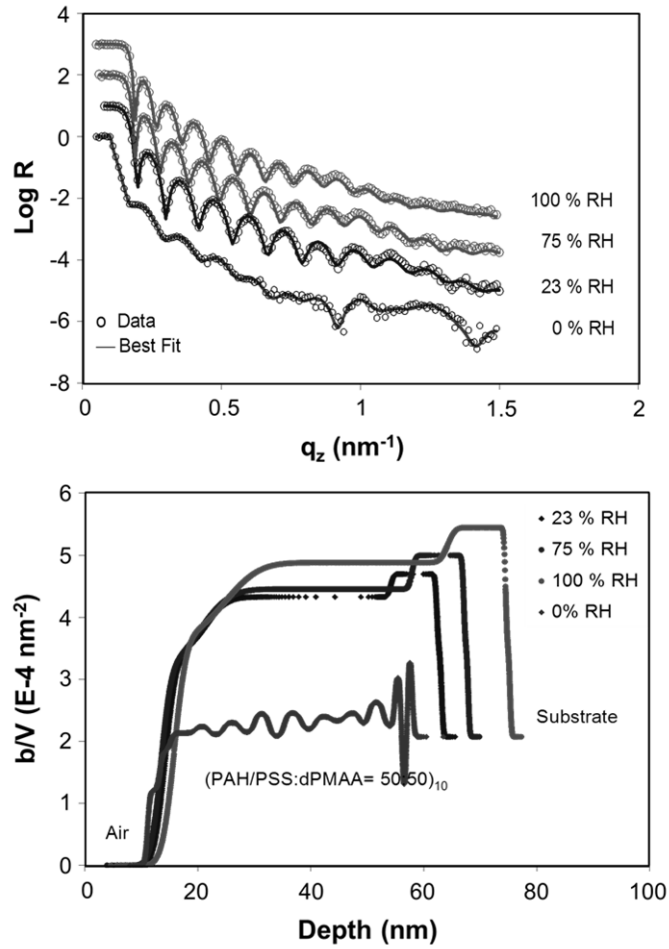

Figure 1.5. Neutron reflectivity (NR) curves with best fits and scattering length density (SLD) profiles of the multilayer films, [PAH/PSS$_{50}$:*d*-PMAA$_{50}$]$_{10}$ prepared by the dip-assisted LbL deposition. The changes in the internal structure of model multilayer films were monitored as a function of relative humidity (RH) by NR.

1.3.3. Relative Humidity-Driven Swelling Behavior of Polymer Multilayer Thin Films

The blended PE multilayer films, $[PAH/(PSS_x:PMAA_{100-x})]_n$ (x = 100, 90, 50, 0), were prepared by the dip-assisted LbL deposition in order to demonstrate the effect of blend ratio on the swelling behavior as a function of RH using quartz crystal microbalance with dissipation (QCM-D) monitoring.

The relative incorporation ratio of a strong polyanion (PSS) and a weak polyanion (PMAA) within the blend multilayer film shows different composition with prepared blend solutions (Table 1.1). The incorporation ratio of PSS and PMAA in $[PAH/PSS_x:PMAA_{100-x}]_{10}$ films was calculated from FT-IR and QCM measurements. Based on the characteristic IR absorbance peaks and QCM frequency changes of each of 100 wt % PSS and 100 wt % PMAA, the mass and IR absorbance of PSS and PMAA in blend multilayer films were normalized to the pure PSS and PMAA films and the incorporated ratio between PSS and PMAA within the blend film was calculated in terms of wt %. The area of characteristic absorbance peaks of PSS and PMAA was calculated by Gaussian-Lorentz method. The characteristic peaks of PSS are shown at 1034 and 1007 cm^{-1} due to SO_3^- symmetric vibration, and PMAA has the characteristic absorbance peaks at 1701 and 1671 cm^{-1} originated from uncharged carboxylic acid groups and 1552 cm^{-1} originated from asymmetric stretching vibration of carboxylate groups.

Table 1.1. The feed ratio of PSS and PMAA in blend polyanion solutions and the incorporation ratio of PSS and PMAA in multilayer films.

Feed Ratio (wt %) in Solutions	**Incorporation Ratio (wt %) in Multilayer Films**
PSS : PMAA	**PSS : PMAA**
100 : 0	**100 : 0**
90 : 10	**78 : 22**
50 : 50	**11 : 89**
0 : 100	**0 : 100**

The difference in the feed ratio and the incorporation ratio is originated from different charge density between weak and strong PEs at certain pH condition. At pH 3.5, PMAA chains, which pK_a value is reported about 5 to 5.5, has lower charge density than PSS chains which have permanent negative charges in every repeat unit. Therefore, in the pH 3.5 solution, PMAA chains have loops and tails conformations, while PSS chains have stretched conformations due to strong charge-charge repulsion. As these coiled structures of PMAA chains, adsorbed amounts of PMAA are increased in order to compensate for the positively charges from PAH chains on the surface. Therefore, the incorporated composition of PMAA in multilayer films is much higher than its feed ratio in blend solutions. Furthermore, the total amount of polyanions (PSS:PMAA) incorporated in multilayer films is rapidly increased as the feed ratio of PMAA in PE solution is increased. The total incorporated amount of polyanions in the multilayer films was compared as a function of blend ratio through measurements for the UV absorbance of PSS at 225 nm (Figure 1.6). The UV absorbance of PSS in the blend multilayer films is interestingly increased although the incorporation ratio of PSS to the PMAA is decreased. This result indicates that the PSS adsorption is also increased with adding PMAA chains because the charge screening effect of partially charged weak PEs to strong PEs. Inter- or intra- repulsion between fully charged PSS chains are reduced due to partially charged PMAA chains like adding ionic salts and the adsorbed amounts of PSS are increased. In addition, the linear growth behavior of the blend multilayer films was confirmed except for the early stage of deposition due to substrate effect. For a convenience of the description in this study, the blend ratio of PSS (i.e., x (wt %)) is regarded as the feed ratio in the blended solutions.

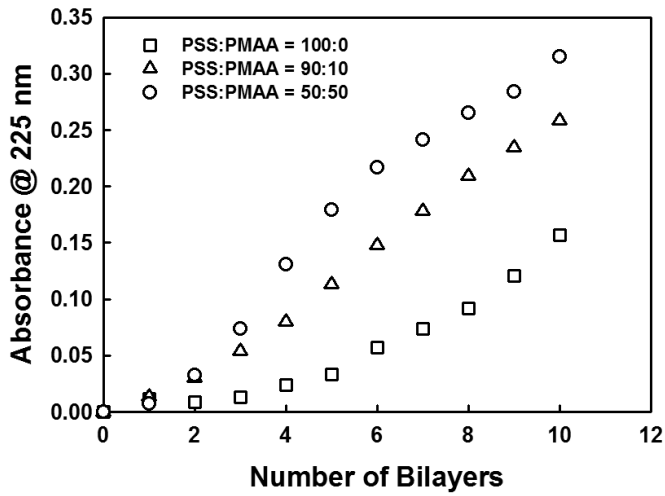

Figure 1.6. UV absorbance of $[PAH/PSS_x:PMAA_{100-x}]_n$ (x = 100, 90, 50) multilayer films with different blend ratios as a function of the number of bilayers (n).

The blend multilayer films generally offer versatility to control physical and chemical properties such as film thickness, morphology, composition, surface properties and film stability for diverse potential applications by simply changing the blend ratio. In this regard, we demonstrated the modulation of swelling behavior in the blend multilayer films as a function of the blend ratio and monitored the nano-scale changes in the film mass by QCM-D along with NR measurements to show the changes in internal structure of the blend film as a function of relative humidity (RH).

In order to investigate the swelling behavior of the $[PAH/PSS_x:PMAA_{100-x}]_{10}$ films (x = 100, 90, 50, 100) in terms of humid air absorption, the continuous humidified gas delivery system was combined with the QCM-D instrument (Figure 8). The moisture is introduced to the QCM-D chamber by running N_2 gas bubbles from the supersaturated salt solutions with fixed flow rate, 10 ml/min. The supersaturated salt solutions of LiBr, $CaCl_2$, NaBr, NaCl and KNO_3 control the RH of the QCM-D chamber with 6 %, 29 %, 58 %, 75 % and 98 %, respectively at 25 ºC. This humidified gas makes the multilayer film deposited onto a quartz crystal swollen, and the degree of swelling is monitored by the change in frequency (ΔF) of quartz crystal electrode.

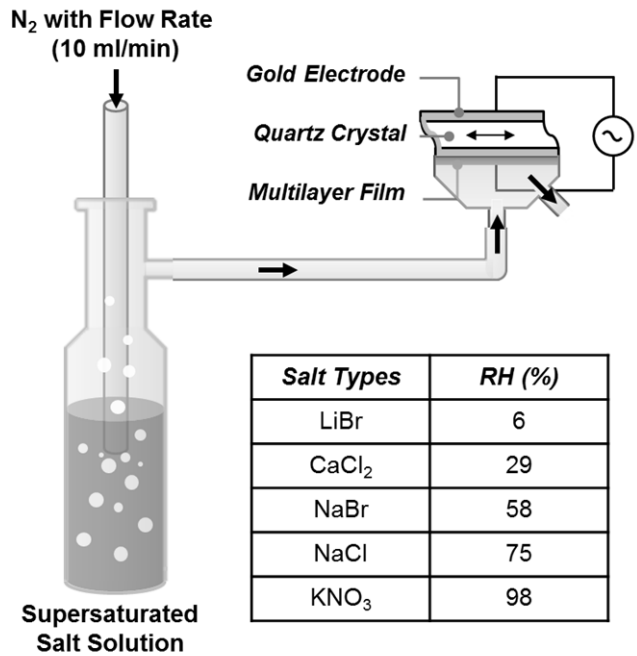

Salt Types	*RH (%)*
LiBr	6
$CaCl_2$	29
NaBr	58
NaCl	75
KNO_3	98

Scheme 1.2. Schematic representation of QCM-D measurements with different relative humidity (RH) at 25 ºC. The RH is controlled by different kinds of supersaturated salt solutions.

The change in frequency ($\Delta f_3/3$) of the $[PAH/PSS_{50}:PMAA_{50}]_{10}$ film as a function of the RH is shown in Figure 1.7A. The value of $\Delta f_3/3$ is calculated from the difference in the absolute frequency at RH 6 %. The supersaturated salt solution was changed after constant frequency is obtained, which indicates the equilibrium state of water adsorption process. As the RH is increased, the frequency is decreased as the moisture is absorbed into the blend multilayer film. Other blend multilayer films with different blend ratios (i.e., PSS:PMAA = 100:0, 90:10 and 0:100) have also similar tendency to RH but show different degree of swelling (Figure 1.7B) with each other. The increased mass originated from the moisture absorption is calculated by Sauerbrey equation:

$$\Delta m = - C \Delta f_n/n$$

C is the proportionality constant related to intrinsic properties of quartz (17.7 $ng \cdot cm^{-2} \cdot Hz^{-1}$ for a 5 MHz quartz crystal), and n represents the overtone number (n = 1, 3, 5, 7). The dissipation change of the elastic films is not sensitive to overtones and usually less than 2.0×10^{-6}. In the present study, the frequency changes ($\Delta f_n/n$) were superimposed with different overtone numbers as well as the dissipation energy of each multilayer was less than 2.0×10^{-6}, regardless of the blend ratio (Figure 1.8). Therefore, the increased masses of the blend multilayer films as a function of RH were calculated based on the Sauerbrey equation. The non-blended $[PAH/PSS]_{10}$ strong PE multilayer film shows the lowest degree of swelling compared with other weak or blended PE multilayer films. It is also confirmed that more water molecules are absorbed into the film as the incorporation ratio of PMAA within a film is increased. The similar amount of water molecules was absorbed into $[PAH/PSS_{50}: PMAA_{50}]_{10}$ films as compared to non-blended weak PE $[PAH/PMAA]_{10}$ multilayer films, and this results can be interpreted by the fact that the $[PAH/PSS_{50}:PMAA_{50}]_{10}$ multilayer film incorporates almost 90 wt% PMAA in polyanionic layers.

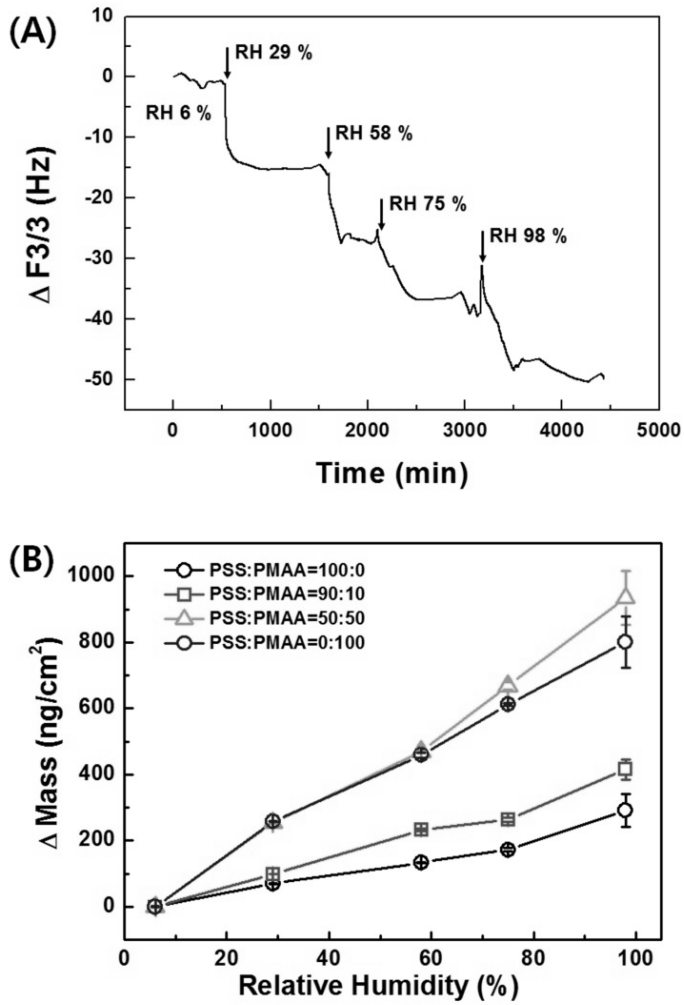

Figure 1.7. (A) QCM frequency change of $[PAH/PSS_{50}:PMAA_{50}]_{10}$ multilayer films with the different RH. Arrow points mean the time to change the different supersaturated solutions for controlling RH. **(B)** Mass changes of the blend multilayer films with different blend ratios (PSS:PMAA = 100:0, 90:10, 50:50, and 0:100) as a function of different RH.

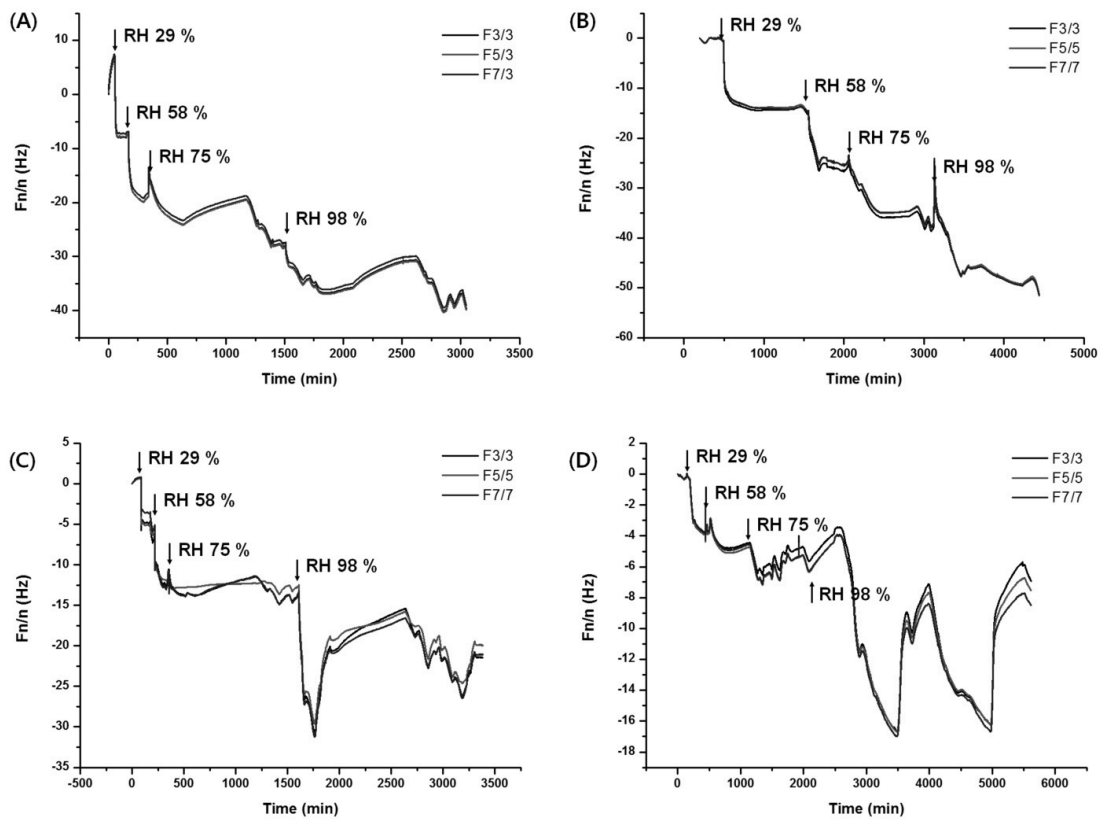

Figure 1.8. Raw data of QCM frequency changes of the blend multilayer films with different blend ratios, $[PAH/PSS_x:PMAA_{100-x}]_{10}$ (x = (A) 0, (B) 50, (C) 90, (D) 100) , as a function of RH. The QCM frequency shows unstable and oscillating signal at high RH 98 % due to low delivery capability of the efficient moisture with one supersaturated salt solution. In order to acquire the stable signal, two supersaturated solution chambers are connected with the QCM-D instrument and it somewhat increases the capability of the moisture delivery.

The swelling of multilayer films are strongly dependent on the internal structure such as chain conformation, free volume, and degree of uncomplexed charged groups as well as the characteristic of topmost layer such as hydrophilicity. The absorption of water vapor into multilayer films may be occurred by hydrogen bonding with uncomplexed functional groups, which is not bound with opposite charged species inside the multilayer. In the case of $[PAH/PSS]_{10}$ multilayers, strong electrostatic interactions between PAH and PSS is dominant and there are a few free charged groups in multilayer films thus the degree of swelling shows low level. However, weakly charged PMAA chains mixed with highly charged PSS chains can increase the extent of water binding site, indicating free carboxylic acid groups in blend multilayer films and their loops and tails structures can induce enough space to bind with water molecules inside the films. These effects make high degree of swelling in weak PE or blended multilayer films.

The swelling behavior of model blend multilayer films containing the mixtures of strong (PSS) and weak (PMAA) PEs, $[PAH/PSS_x:PMAA_{100-x}]_n$, has been systematically investigated as a function of the incorporated ratio between PSS and PMAA and relative humidity (RH) by analyzing moisture absorption-induced mass increase within the film as well as monitoring the humidity-triggered changes in the internal structures. The different adsorption behavior between PSS and PMAA in the dipping process was confirmed by the LbL growth behavior and the internal structure, which is originated from different conformation state according to their charge density. As the results, the dip-assisted $[PAH/d\text{-}PSS]_{10}$ film shows the uniform density profiles in the entire film thickness due to interlayer mixing between adjacent layers and tight electrostatic binding with stretched conformation. On the other hands, the dip-assisted $[PAH/d\text{-}PMAA]_{10}$ film yields well-defined internal structures with optimal distance between layers due to coiled structures of partially charged

PMAA chains. These free carboxylic groups and the loop and tail conformations of partially charged PMAA chains preferentially capture water molecules within multilayer films. Accordingly, the degree of swelling is larger in the case of the multilayer films dominantly incorporating PMAA chains than the case of PSS-dominantly blended-multilayer films.

1.4. Conclusion

In the present study, the methods to engineer internal structures and swelling properties of polymer multilayer thin film platforms are introduced based on the LbL deposition. The LbL assembly has been considered to be the one of the most efficient and practical methods for preparing multifunctional polymer thin film platforms, taking advantage of various intermolecular interactions among paired species. Depending on the range of the intermolecular interactions between polymer chains (i.e., long-range electrostatic interactions or short-range hydrogen bonding), the growth rate of bilayer thickness and the multilayer internal structure are greatly controlled by the LbL deposition methods. In the case of using short-ranged hydrogen bonding pairs and partially charged weak polyelectrolyte (PE) chains, the dip-assisted LbL deposition makes thicker bilayers and well-defined multilayer structures as compared to the spin-assisted LbL films, because the dipping method enables for polymer chains to adsorb onto a surface by self-diffusion process within aqueous environment. On the other hand, the spin-assisted LbL deposition makes well-defined internal structures within multilayer films, regardless of polymer types used, due to the additional centrifugal and air shear forces. Based on the NR measurements, the internal structures and RH-driven swelling behavior of LbL-assembled multilayer films are systematically investigated as a function of LbL deposition techniques and the types of intermolecular interactions. Furthermore, it is demonstrated that the loop and tail conformations of partially charged weak PE chains preferentially capture water molecules within multilayer films as compared to fully charged and tightly bound PE chains with stretched conformations by QCM-D measurements.

1.5. References

(1) G. Decher, *Science,* **277**, 1232-1237 (1997).

(2) G. Decher and J. D. Hong, *Makromolekulare Chemie-Macromolecular Symposia,* **46**, 321-327 (1991).

(3) P. T. Hammond, *Advanced Materials,* **16**, 1271-1293 (2004).

(4) J. A. Jaber and J. B. Schlenoff, *Current Opinion in Colloid & Interface Science,* **11**, 324-329 (2006).

(5) Z. Tang, Y. Wang, P. Podsiadlo, and N. A. Kotov, *Advanced Materials,* **18**, 3203-3224 (2006).

(6) C. Y. Jiang and V. V. Tsukruk, *Advanced Materials,* **18**, 829-840 (2006).

(7) A. Quinn, G. K. Such, J. F. Quinn, and F. Caruso, *Advanced Functional Materials,* **18**, 17-26 (2008).

(8) Y. Wang, A. S. Angelatos, and F. Caruso, *Chemistry of Materials,* **20**, 848-858 (2008).

(9) E. Kharlampieva, V. Kozlovskaya, and S. A. Sukhishvili, *Advanced Materials,* **21**, 3053-3065 (2009).

(10) J. B. Schlenoff, *Langmuir,* **25**, 14007-14010 (2009).

(11) R. K. Iler, *Journal of Colloid and Interface Science,* **21**, 569-594 (1966).

(12) J. Cho, K. Char, J. D. Hong, and K. B. Lee, *Advanced Materials,* **13**, 1076-+ (2001).

(13) J. B. Schlenoff, S. T. Dubas, and T. Farhat, *Langmuir,* **16**, 9968-9969 (2000).

(14) M. Lee, W. Park, C. Chung, J. Lim, S. Kwon, K. H. Ahn, S. J. Lee, and K. Char, *Lab on a Chip,* **10**, 1160-1166 (2010).

(15) T. Boudou, T. Crouzier, K. F. Ren, G. Blin, and C. Picart, *Advanced Materials,* **22**, 441-467 (2010).

(16) R. von Klitzing, *Physical Chemistry Chemical Physics,* **8**, 5012-5033 (2006).

(17) J. F. Quinn, A. P. Johnston, G. K. Such, A. N. Zelikin, and F. Caruso, *Chemical Society Reviews*, **36**, 707-718 (2007)

(18) X. Jhang, H. Chen, and H. Zhang, *Chemical Communications*, **14**, 1395-1405 (2007)

(19) W. B. Russel, D. A. Saville, W. R. Schowalter, R. William, *Colloidal Dispersions*, New York: Cambridge University Press, (1989)

(20) J. Israelachvili, *Intermolecular & Surface Forces*, 3nd Edition, Academic Press (2 011)

(21) Decher, G., *Science***,** *277*, 1232-1237 (1997).

(22) Losche, M.; Schmitt, J.; Decher, G.; Bouwman, W. G.; Kjaer, K., *Macromolecul es***,** *31*, 8893-8906 (1998).

Chapter 2.[*]

Controlled Release from Model Blend Multilayer Films Containing Mixtures of Strong and Weak Polyelectrolytes

2.1. Introduction

Great efforts have been devoted to develop thin film platforms for diverse biomedical applications. In particular, thin films which provide the controlled release of active biomolecules from the surfaces have the potentials to be used as bioactive coatings on implants. Among various techniques to prepare well-designed thin films, the layer-by-layer (LbL) deposition method has received great attention due to its versatility, biocompatible processing in aqueous environment and the ability to insert therapeutic biomolecules at a desired position within the multilayer thin film. Moreover, the LbL deposition technique facilitates the programming of the release sequence of active materials by adjusting the molecular interactions between layers.[1-7]

Various types of multilayer thin films have been investigated for the controlled release by tuning diverse parameters including intrinsically degradable properties of polymers employed as well as external stimuli such as ionic strength, temperature, light, enzyme, electrical signal and pH.[8-17] Particularly for pH-responsive release systems, multilayer films containing weak polyelectrolyte (PE) pairs have been exploited because the swelling and decomposition of multilayer films can easily be controlled by changing the solution pH. Most research on the

[*] This chapter is based on a paper from Yeongseon Jang, Bulent Akgun, Hosub Kim, Sushil Satija, and Kookheon Char, *Macromolecules* **2012**, 45, 3542-3549. Copyright 2012 American Chemical Society

weak PE multilayer films for biological applications has been focused on the structural change of the films at specific pH 7.4, the physiological condition in blood.[8-9] However, multilayer films solely composed of weak PEs show rapid morphological change within 20 min and subsequent disassembly when they are exposed to low pH solution ($1 \leq pH \leq 3$).[18-19] This rapid transition in the stability of weak PE multilayer films under acidic condition still remains as a critical obstacle for biomedical applications because pH in human body widely varies from 1.0 to 8.5.[20] Since most of drugs are rapidly degraded at pH 2, many material scientists and pharmacologists have focused on the design of controlled release systems to provide adequate release in gastric environment ($pH \leq 2$).[21-23] To overcome the film instability of weak PE multilayers in extreme pH conditions, blended solutions consisting of both weak and strong PEs can be used by taking advantage of pH-independent characteristic of strong PEs.[24] The PE blend multilayer films generally offer versatility to control physical and biochemical properties such as film thickness, morphology, composition, and film stability for diverse potential applications.[25-26] In addition, the LbL deposition with blend solutions enables to insert expensive bioactive molecules effectively at a desired position and to release them in a controlled manner.[9]

Herein, we report the release behavior of PE chains from model blend multilayer films containing mixtures of strong and weak anionic PEs (i.e., poly(styrenesulfonate) (PSS) and poly(methacrylic acid) (PMAA)). PSS is a strong anionic PE, which is always fully charged independent of pH of the solutions whereas, PMAA is a weak anionic PE and its charge density varies by the solution pH. Linear poly(ethylene imine) (LPEI) is used for weak cationic PE layers. The blend multilayer films ($[LPEI/PSS:PMAA]_n$) with well-defined internal structure are prepared by the spin-assisted LbL deposition method[27-28] and the release behavior of weak deuterated PMAA (*d*-PMAA) is systematically characterized by NR.

Regularly spaced *d*-PMAA layers result in equally spaced peaks in SLD profiles and the change in peak shape and position after post-treatment give the ability to monitor internal rearrangement of model blend film using NR. In addition to NR measurements, changes in thickness, surface morphology and film composition were thoroughly investigated as a function of blend ratio when the blend films were post-treated at pH 2 using ellipsometry, atomic force microscopy (AFM), and FT-IR. The *in-situ* release kinetics of the model blend films were analyzed by quartz crystal microbalance with dissipation (QCM-D) measurements, providing insightful information relevant to the changes in film mass with nanogram unit.[29] The approaches taken in the present study represent the controlled release platforms based on blend multilayer films to overcome the weakness of pH-sensitive weak PE films in acidic environment. Furthermore, the results shown here would give some insights on the improved release property of target active macromolecules from blend multilayer thin films, offering versatile, adjustable stimuli-responsive polymeric release platforms.

2.2. Experimental Section

Materials. Linear poly(ethyleneimine) (LPEI, M_w = 25,000 g/mol) and poly(methacrylic acid) (PMAA, M_w = 15,000 g/mol) were purchased from Polysciences.[30] Poly (sodium 4-styrene sulfonate) (PSS, M_w = 70,000 g/mol) and deuterated poly(methacrylic acid) (d-PMAA, M_w = 43,000 g/mol) were obtained from Aldrich[30] and Polymer Source,[30] respectively. All polymers were used as received. Silicon wafers, CaF_2 round crystal windows (Sigma Aldrich[30]) and Au sensor crystals (QSX 301, Q-Sense[30]) were used as substrates to build blend multilayer films for further characterization.

Fabrication of Blend Multilayer Films. A LPEI solution and mixed solutions of PSS and PMAA were chosen for cationic and anionic polyelectrolyte solutions to prepare blend multilayer films. All the polymer solutions were prepared by dissolving polymers in 18 MΩ Milli-Q water with concentrations of 0.01 M (based on repeat units) and solution pH was adjusted to pH 5.0 by adding diluted HCl or NaOH solution. The blend ratio of the polyanion mixtures was varied based on the molarity of each polymer (i.e., PSS (M):PMAA (M) = 0:100, 10:90, 30:70, 100:0). Prior to multilayer deposition, all the substrates were cleaned with piranha solution (mixtures of 70 vol % H_2SO_4 and 30 vol % H_2O_2) for 20 min at room temperature and washed thoroughly with DI water, followed by drying under nitrogen stream. The blend multilayer films, $[LPEI/PSS_x:PMAA_{100-x}]_n$ (x: mole % of PSS in an anionic PE solution, n: number of bilayers), were prepared by the spin-assisted LbL deposition method with a spin-rate of 4000 rpm for 40 sec for each deposition, followed by three consecutive washing steps for each polymer deposition with pH 5.0 DI water.

Post-Treatment of Blend Multilayer Films. The post-treatment for releasing multilayer films was performed by immersing the prepared multilayer films in pH 2.0 DI water for 10 min,

which was proven to provide the sufficient disruption of multilayer films solely prepared with weak polyelectrolytes $(LPEI/PMAA)_{16}$. The post-treated blend multilayer films were washed thoroughly with pH 2.0 water, followed by the relevant drying process under N_2 stream.

Neutron Reflectivity (NR) Measurements. The internal structures of the blend multilayer films were characterized by NR measurements conducted at the NG7 horizontal reflectometer at National Institute of Standards and Technology (NIST) Center for Neutron Research (NCNR). For all the samples NR data were collected up to $q_{z,max}$ of 0.15 $Å^{-1}$. The NR experiments were performed in a closed chamber with $CaSO_4$ platelets to keep relative humidity close to zero. Samples are equilibrated in the closed chamber at least for 1 h and then the measurements started. Previous experience with identical bilayers films showed that the 1 h is enough to reach equilibrium. Background subtraction and main beam normalization were made using the REFLPAK[31] software package provided by NIST. The structure of thin films in general cannot be determined by direct inversion of NR data to SLD profile due to the loss of phase information during the measurement. To obtain a real space depth profile first a candidate model was chosen and the parameters (thickness, roughness and SLD) of the model were varied using non-linear regression until a simulated reflectivity curve calculated from the model structure using Parratt[32] formalism agrees sufficiently well with the experimental data. All the data was fitted using Parratt 32 and Motofit reflectivity analysis packages. Even though this is an indirect analysis method if preliminary information is obtained by other characterization techniques (e.g. AFM, XRR and ellipsometer) thickness, roughness and SLD of the layers in the film can be obtained with great precision.

Characterization of Blend Multilayer Films. The total film thicknesses were measured by a variable-angle multiwavelength ellipsometer (Gaertner L2W16C830, Gaertner Scientific Corp.[30]) and the surface morphologies of films were obtained with atomic force microscope

(AFM) (Nanoscope IIIa, Digital Instrument[30]). Experimental results were reported by averaging the values of three independent measurements for film thickness and surface roughness. The changes in frequency (Δf_n) and dissipation (ΔD_n) of an Au sensor crystal (QSX301) coated with a blend multilayer film during the post-treatment were monitored by quartz crystal microbalance equipped with dissipation monitoring (QCM-D) (Q-Sense D300, Q-Sense[30]). For the QCM-D measurements, every blend multilayer film was deposited on a cleaned Au sensor crystal. Every film was stabilized in pH 5.0 water solution, which is the same pH condition for the film deposition. 0.8 ml of pH 2.0 water was then injected to the sample chamber to initiate the triggered release. The frequency changes ($\Delta f_n/n$) in all blend multilayer films triggered at pH 2 show the superimposed characteristics with different overtone numbers (n = 3, 5, 7) and dissipation energy less than 2.0×10^{-6}. Therefore, the released film masses ($ng \cdot cm^{-2}$) as a function of post-treatment time at pH 2.0 were calculated based on the Sauerbrey equation. Typically, Δf_1 and ΔD_1 were typically noisy due to insufficient energy trapping. Thus, frequency changes in the third overtone $\Delta f_3/3$ (Hz) were compared with different blend multilayer films. Burst in the release profile of non-blended multilayer film containing LPEI and PMAA only was developed when it triggered at pH 2.0. On the other hand, blended multilayer films containing 10 mol% and 30 mol% PSS have unique release profile followed by instant swelling. In order to normalize the QCM data of each blend multilayer film, the starting point of the release from the films is set to zero based on the absolute frequency stabilized at pH 5. The composition of blend multilayer films was characterized with FT-IR (FT-IR-200 spectrometer, JASCO Corp.[30]). The multilayer film for FT-IR measurement was prepared on a CaF_2 crystal, which is transparent to IR light.

2.3. Results and Discussion

The controlled release platforms based on blend multilayer films, $[LPEI/PSS_x:PMAA_{100-x}]_n$ (x = 0, 10, 30, 100) were prepared by the spin-assisted LbL deposition employing electrostatic interactions. To explore the pH-induced controlled release behavior of model blend multilayer films as a function of the blend ratio of weak (PMAA) and strong (PSS) PEs, film characteristics including thickness, internal structure, surface morphology, film mass, and film compositions before and after the post-treatment at pH 2.0 were investigated and discussed in detail in the following.

2.3.1. Growth Behavior of Spin-Assisted Polymer Blend Multilayer Films

Several studies using dip coating have reported that LbL films containing LPEI, in particular, exhibited the exponential growth behavior with the increase in bilayer number. Exponential growth phenomenon is based on the reversible internal rearrangement of mobile polymer chains such as LPEI.[33-34] Excess LPEI chains exhibit diffusion into the interior of a multilayer film as well as possessing chain mobility out to the film surface in each dipping process. Therefore, the dip-assisted LbL film containing LPEI shows the exponential growth behavior. However, in the case of the spin-assisted LbL deposition method, such interdiffusion behavior of LPEI chains is significantly suppressed and resulting films demonstrated linear growth behavior (Figure 2.1). The discrepancy between conventional dip-assisted and spin-assisted LbL deposition is the different adsorption mechanisms (i.e., self-diffusion vs forced-diffusion process). The spin-assisted LbL deposition incorporates strong centrifugal force, viscous force and air shear force along with intermolecular forces among adsorbing PE pairs.[27] In particular, the viscous force caused by fast solvent

evaporation dramatically decreases the mobility and interdiffusion of LPEI chains within a multilayer film. Therefore, the spin-assisted LbL deposition allows us to construct a well-defined internal structure across the film thickness compared with the intermixed phase often seen in the dip-assisted LbL deposition.[35]

The multilayers were assembled with LPEI and PSS:PMAA blend solutions at pH 5.0, which is close to pKa values of both weak PEs. The pK_a values of LPEI and PMAA weak PEs are around 4.8 ~ 5.0 and 5.5, respectively.[33,35] The electrostatic interactions between partially positive charges on LPEI chains and partially negative charges on PMAA chains form thick LbL-assembled multilayer films at pH 5.0 due to their coiled conformation. As has been well documented in the literature, the LbL film thickness can be controlled by simply changing the blend ratio of two anionic PEs in the adsorption solutions.[24-26, 37-38] A representative example of PE blend multilayer films is the LbL deposition of cationic poly(allylamine hydrochloride) (PAH) solution and blended anionic solution with poly(acrylic acid) (PAA) and PSS. In this example, the thickness of $(PAH/PSS:PAA)_8$ multilayers varies between 18 (PSS 100 %) and 220 nm (PAA 100%). The relatively large thickness observed with PAH/PAA weak multilayer films is attributed to partially charged nature of PAA under the deposition conditions of pH 3.5, where PAA adsorbs in a highly coiled conformation. In contrast, a permanently negative charged PSS adopts a more stretched conformation due to higher charge per molecule and intra-molecular electrostatic repulsions.[26] Similar to these $[PAH/PSS:PAA]_n$ blend multilayers, the decrease in the thickness growth rate of $[LPEI/PSS_x:PAA_{100-x}]_n$ films used in the present study was observed with increasing PSS fraction in the blend solutions. However, the linear growth of film thickness, regardless of the blend ratio between PSS and PMAA, is highly desirable for LbL systems in many occasions and the spin-assisted LbL deposition to grow multilayered films

circumvents problems typically associated with the dip-assisted LbL deposition: the spin-assisted LbL deposition yielding well-organized internal film structure considerably facilitates the monitoring of the changes in model deuterated PE layers inserted at desired position within multilayer films using NR.

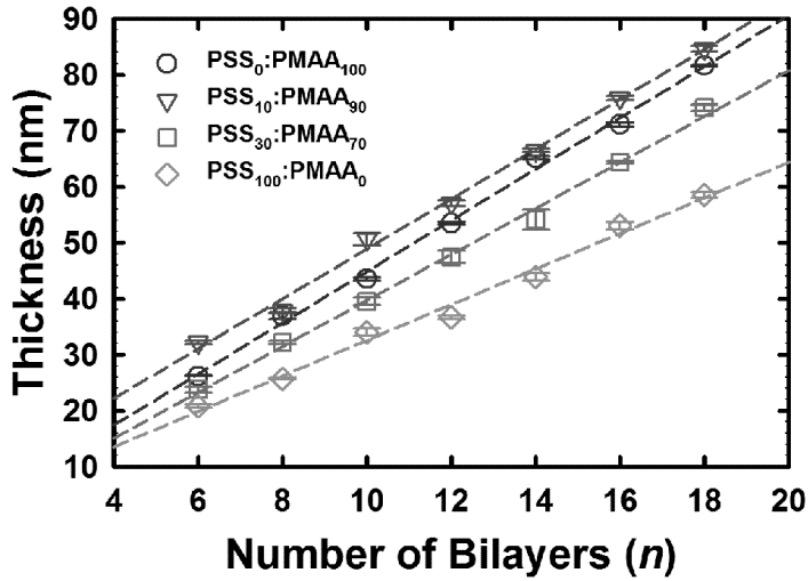

Figure 2.1. Thickness growth curves of blend multilayer films, $[LPEI/PSS_x:PMAA_{100-x}]_n$, as a function of number of bilayers. The films were assembled in pH 5.0 solutions and thickness measurements were taken in ambient air.

2.3.2. Changes in the Internal Film Structure Monitored by NR

NR experiments have been performed on model blend multilayer films to monitor the changes in internal structure before and after post-treatment. As schematically represented in Scheme 2.1, blend multilayer films for NR study were constructed by replacing PMAA with *d*-PMAA chains in the mixed polyanion solutions of PSS and PMAA in every 4th bilayer deposition to create neutron contrast. This configuration yields four spikes in the neutron SLD profile and the changes in the height and the position of these spikes in the direction normal to the surface yields information on the diffusion and release of d-PMAA chains.

In order to investigate the effect of the strong PE PSS on the release behavior of weak PE *d*-PMAA chains from the multilayer films, model $[(LPEI/PSS_x:PMAA_{100-x})_3(LPEI/PSS_x:d\text{-}PMAA_{100-x})_1]_3$ multilayer films were constructed with different ratios of PSS and PMAA (i.e., PSS (M):*h*- or *d*-PMAA (M) = 0:100, 10:90, and 30:70) in blend polyanion solutions. Prior to NR measurements, the incorporated amount of PMAA within the blend multilayer films was calculated using quartz crystal microbalance (QCM) and the FT-IR measurements.[24] When the fraction of PSS in the blend polyanion solution is varied from 0 to 30 mol%, PSS and PMAA are incorporated into the blend films with ratios similar to the feed ratios (Table 2.1). Therefore, herein, the blend ratios of PSS and PMAA in polyanion solutions can be considered as the ratios incorporated within the blended multilayer films.

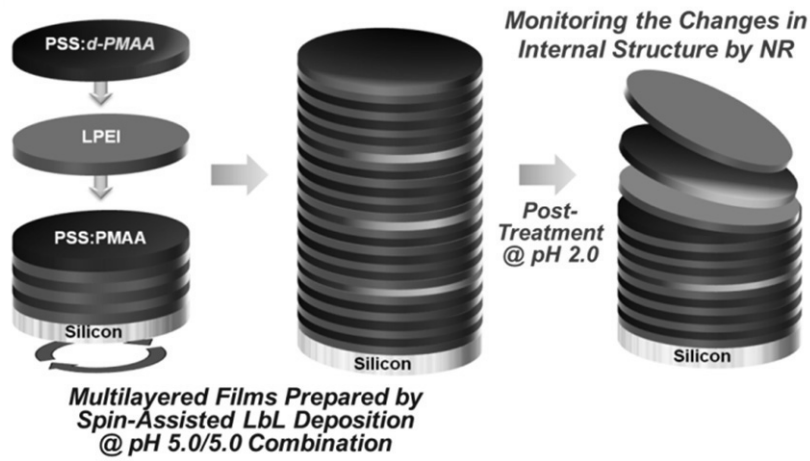

Scheme 2.1. A schematic on the LbL deposition and post-treatment process of model blend multilayer films, $[(\text{LPEI/PSS}_x\text{:PMAA}_{100\text{-}x})_3(\text{LPEI/PSS}_x\text{:}d\text{-PMAA}_{100\text{-}x})_1]_3$, and their changes in internal structure for NR study.

Table 2.1. Incorporation ratio of PMAA within the blend multilayer films calculated from the film mass obtained from QCM measurements and the IR absorbance peak areas of PMAA chains at 1540 and 1701 cm^{-1}.

Feed Ratio of PMAA in Anionic Solutions	**Incorporation Ratio of PMAA in Blend Multilayer Films**
100	100
90	91 ± 1.7
80	83.2 ± 3.1
70	73.3 ± 2.6

Figure 2.2 illustrates the dramatic changes in the internal structure of multilayer films before and after the post-treatment at pH 2.0 depending on the blend ratio. The NR data were fitted with a classic box model for polyelectrolyte multilayer films, as previously described in prior works.[28, 39-41] Each slab (protonated or deuterated layer) is characterized by SLD, thickness, and roughness in the fitting model. To fit the data, the model was constructed for an idealized LbL structure featuring sharp interfaces between adjacent layers. Initial individual layer thicknesses in the fitting model were taken from ellipsometry measurements and then adjusted to capture to the Bragg peaks in the NR data. This LbL model was then modified iteratively until the reflectivity curve was best fitted to minimize χ^2.

The entire multilayer film prepared only with weak PEs (i.e., $[(LPEI/PMAA)_3(LPEI/d\text{-}PMAA)_1]_4$) was immediately disrupted upon the acidic post-treatment at pH 2.0 (Figure 2.2A) due to the complete loss of electrostatic interactions between the carboxylic groups of PMAA and the secondary amine groups of LPEI. Only 4.5 nm thick layers remained on the substrate after post-treatment due to strong physical interaction of the polymer chains in the first few bilayers with the underlying substrate. Since the pK_a value of PMAA PE is around 5.5,[36] ionized carboxylate groups (COO^-) in PMAA chains are protonated to their corresponding carboxylic acids (COOH) at pH 2.0, losing their negative charges that enable the association with LPEI. Subsequently, the positive charges in LPEI chains increases and the degree of ionization approaches 100 % at pH 2.0 condition because the pK_a value of LPEI is approximately 4.8 ~ 5.0.[33] Therefore, the electrostatic interactions between negative charges on PMAA chains and positive charges on LPEI chains, which form well-ordered LbL-assembled multilayer films at pH 5.0, were significantly diminished during the post-treatment process, resulting in the precipitous disruption of the LbL film. Moreover, the disruption of the multilayer film is believed to be facilitated due to the long-ranged (inter and

intramolecular) electrostatic repulsive forces among increased positive charges of LPEI chains within the film.

However, rapid disruption of the entire multilayer film was prevented by incorporating 10 % of strong PE PSS into the polyanion mixtures, as well documented in Figure 2.2B. The multilayer film composed of $[(LPEI/PSS_{10}:PMAA_{90})_3(LPEI/PSS_{10}:d\text{-}PMAA_{90})_1]_4$ contains smeared Bragg peaks in the NR profile, implying that regularly spaced deuterated layers lose their neutron contrast to some extent within the film due to the mixing with protonated PE chains between the layers. The SLD profile for the blend multilayer film containing 10 % PSS in Figure 2.2B shows that the protonated layers are more mixed with the *d*-PMAA:PSS layers in the blend film when compared with non-blend films. As a consequence of the high degree of intermixing at the substrate side of blend films, the blend multilayer film containing 10 % PSS releases the weak PE d-PMAA from the surface, without showing the burst dissociation from the film. Since PSS chains are fully charged in aqueous solution in the pH range employed, permanent negative charges from the PSS chains are available to provide robust skeletons in blend multilayer films retaining the long-ranged electrostatic crosslinking with the positive charges of LPEI. Therefore, weak PE chains on the surface side move faster than those buried in the multilayer skeleton which is ionically crosslinked by PSS. This is consistent with the fact that the PE chains the surface of the film has a larger diffusion coefficient than those within the film.[10]

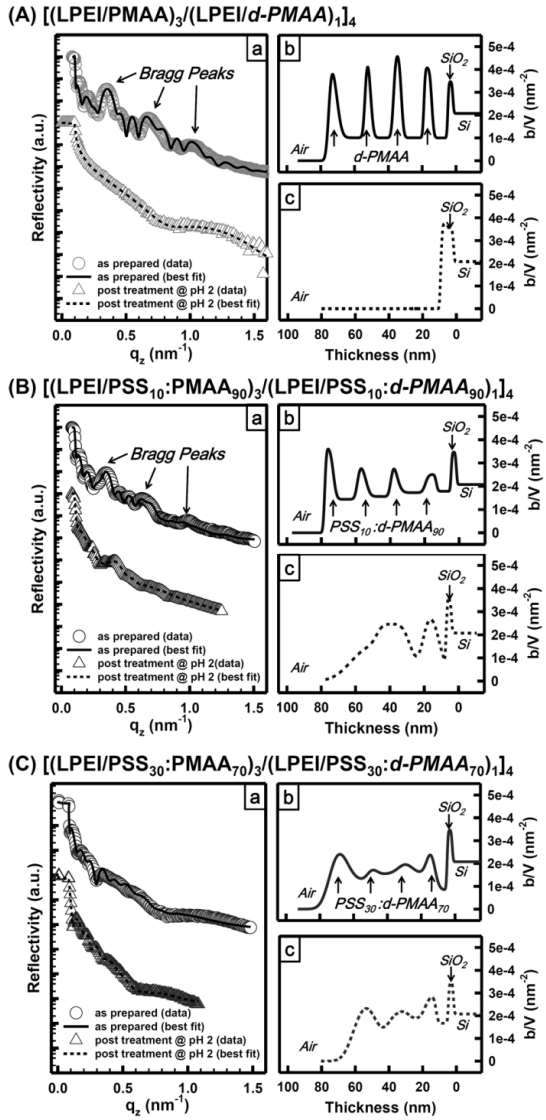

Figure 2.2. Neutron reflectivity (NR) curves with best fits and SLD profiles of blend multilayer films, $[(\text{LPEI/PSS:PMAA})_3(\text{LPEI/PSS:}d\text{-}PMAA)_1]_4$. The changes in the internal structure of model multilayer films with different blend ratios of PSS:PMAA ((A) 0:100, (B) 10:90, and (C) 30:70) were monitored by NR. Films initially deposited at pH 5 are represented by circle symbols in (a) the reflectivity panels and solid lines in (b) the SLD panels while the films post-treated at pH 2 for 10 min are represented by triangle symbols in (a) the reflectivity panels and dashed lines in (c) the SLD panels.

Consequently, the release of weak PE PMAA from the blend multilayer films slowly transforms from the initial burst disruption to the surface attrition by increasing the amount of strong PE PSS in the mixtures of polyanions. As shown in Figure 2.2C, only weak PEs residing at the top layer of the blend film are released while d-PMAA chains buried deep inside the blend multilayer film are virtually intact or immobile most likely due to the ionic crosslinking effect of PSS within the film even after the post-treatment, as shown in the SLD profile (NR data and the fitted SLD profile for the blend multilayer with 20 % PSS show the release behavior similar to the blend multilayer containing 30 % PSS).

The degree of intermixing between individual deposition layers increases with the increase of the fraction of PSS in the mixtures of polyanions. The evidence for this observation originates from the peak broadening of d-PMAA layers in the blend films as well as the increased SLD values of protonated LPEI layers. Another clue for the intimate intermixing mediated by PSS is found from the sharpest and highest peak of *d*-PMAA at the surface (i.e. in contact with air side), elucidating that there is no virtual interpenetration at the surface. The PSS chains embedded within the multilayer film easily capture d-PMAA molecules residing upper or adjacent to LPEI layers. Thus, the release of *d*-PMAA is controlled by the content of PSS in the blend multilayer film, allowing the transition from a burst disruption to the surface erosion. The controlled release behavior of blend multilayer films was also confirmed by complementary experiments with ellipsometer, AFM, QCM and FT-IR.

2.3.3. Changes in Film Thickness and Surface Morphology

The reduction in film thickness after the post-treatment was calculated as a function of the blend ratio of PSS and PMAA, based on the equation shown below:

$$\text{Thickness reduction (\%)} = \frac{t_i - t_f}{t_i} \times 100$$

where t_i and t_f are the initial as-prepared and final post-treated film thicknesses, respectively.

As shown in Figure 2.3, the $(LPEI/PMAA)_{16}$ multilayer film containing weak PMAA polyanions only is almost disassembled after the post-treatment at pH 2.0. However, the thickness reduction remarkably decreases as the PSS content is increased within the multilayer film. The reduction in film thickness estimated from the ellipsometric data coincides with the thickness measurements obtained from the fitting of NR data. Fitting of NR data yields information on film parameters including total film/interlayer thickness as well as internal/external roughness of blend multilayer films before and after post-treatment, as summarized in Table 2.2. (All the error bars in this paper represents +/- 1σ.).

Changes in surface roughness before and after the post-treatment were obtained by AFM (Figure 2.4A) and could also be compared with the film parameters obtained from the NR data. The surface roughness is also very important for the critical transition of surface release properties which could, in turn, be related to pore size and molecular diffusion.[42,43] We thus quantitatively analyzed the RMS surface roughness before and after the post-treatment, as a function of the blend ratio (Table 2.2 and Figure 2.4B). When a multilayer film is constructed with a pair of LPEI and PMAA, the roughness of the remaining very thin film is close to that of the Si substrate after the post-treatment because most likely the first few bilayers are conformal with the substrate. However, in the case of the blend multilayer film containing 10 %

PSS, some residual PEs remain with a roughened surface after the post-treatment, implying the appreciable release of polyelectrolyte chains (i.e., burst-out from the substrate but not entirely disrupted) with a small amount of PSS incorportated into the multilayer film. Consistent with the roughness values obtained by NR as well as the thickness reduction obtained from ellipsometer, the extent of surface morphological change during the pH treatment decreases as the content of PSS within the blend film is increased. We find that film stability against external pH has some correlations with the reduced change in film roughness (Figure 2.4B).

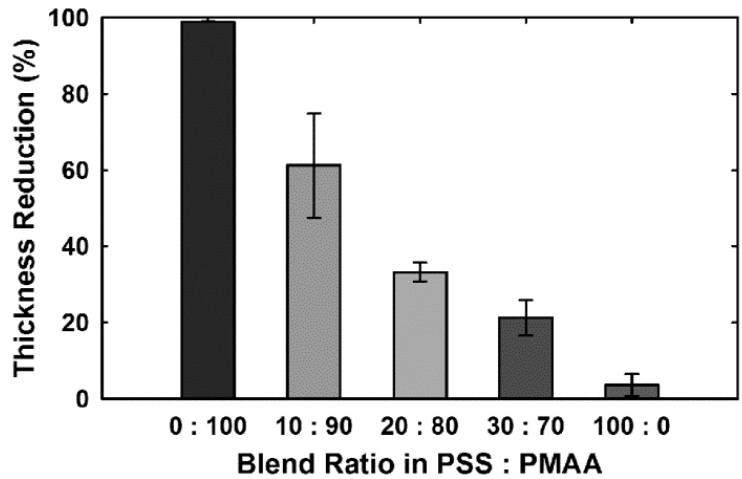

Figure 2.3. Thickness reduction (%) of blend multilayer films as a function of the blend ratio of PSS:PMAA polyanion mixtures, as measured by an ellipsometer.

Table 2.2. Film parameters determined from NR measurements for model blend multilayer films with different blend ratios of PSS:PMAA ((A) 0:100, (B) 10:90, and (C) 30:70) before and after treatment at pH 2

Model Blend Multilayer Films	**As-Prepared Films**			**Films Post-Treated @ pH 2**		
	Total Film Thickness (nm)	**External Roughness (nm)**	**Internal Roughness (nm)**	**Total Film Thickness (nm)**	**External Roughness (nm)**	**Internal Roughness (nm)**
(A)	70.5	1.4	1.3 ± 0.5	4.5	0.6	-±
(B)	73.4	0.8	1.5 ± 0.5	40.5	8.4	4.4 ± 2.3
(C)	69.5	4.2	3.5 ± 0.9	56.6	4.8	2.8 ± 1.1

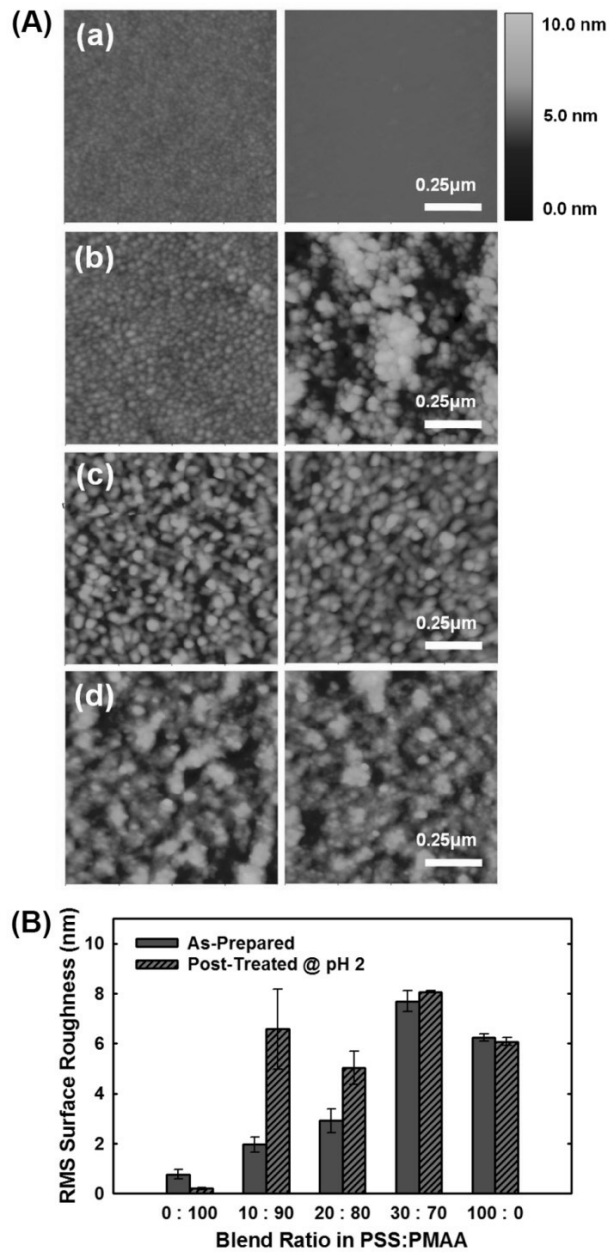

Figure 2.4. Changes in (A) surface morphology of as-deposited (left column) and post-treated (right column) blend multilayer films with different blend ratios of PSS: PMAA polyanions ((a) 0:100; (b) 10:90; (c) 30:70; (d) 100:0). (B) Changes in RMS surface roughness as a function of blend ratio.

2.3.4. Release Kinetics Monitored by Quartz Crystal Microbalance with Dissipation (QCM-D)

Release kinetics as a function of blend ratio of polyanions was monitored with *in-situ* quartz crystal microbalance with dissipation (QCM-D) measurements. In the present study, the released film masses ($ng \cdot cm^{-2}$) as a function of post-treatment time at pH 2.0 were calculated based on the Sauerbrey equation because the frequency changes ($\Delta f_n/n$) were superimposed with different overtone numbers (n = 3, 5, 7) as well as the dissipation energy of each multilayer was less than 2.0×10^{-6}, regardless of the blend ratio (Figure 2.6). The released film mass curves of blend multilayer films, shown in Figure 2.5, were calculated from the normalized frequency changes in third overtone ($\Delta f_3/3$). As shown in Figure 2.5, an initial burst in the release profile of non-blended multilayer film containing LPEI and PMAA only was observed when the film is subject to post-treatment at pH 2.0, implying that the release behavior is induced directly from the substrate due to the absence of PSS. On the other hand, blended multilayer films containing 10 % and 30 % PSS show more retarded release rates when compared with the non-blend weak PE film. In the case of $(LPEI/PSS)_{16}$ multilayer film, it is clearly demonstrated that there is no change in the film mass even after the post-treatment at pH 2.0 for more than 1,000 min.

The percentage of released film mass relative to the initial deposited mass was obtained from QCM measurements at different PSS blend ratios. The initial film masses were calculated using the Sauerbrey equation, based on the difference in absolute frequency (f_3) between a bare Au electrode and the electrodes coated with multilayer films. Compared with each initially deposited film mass, 81 % of the original film mass is released from the multilayer film consisting of weak PEs only while 37 % and 11 % of masses of blended multilayer films containing 10 % and 30 % of PSS are lost from the film surface during the

post-treatment at pH 2.0 for 1000 min. The differences in the released film masses with different strong PE content demonstrate that the blend multilayer systems have great potential to control the amount of materials delivered as well as the rate of attrition.

2.3.5. Analysis on Component Changes in Polymer Blend Multilayer Films during pH-Induced Release

The reason why the blended films containing PSS PEs show the controlled release behavior is that the strong PSS PEs provide permanent negatively charge density to associate with positive LPEI layer and it could serve as robust skeletons of the films against external pH change. In order to verify the skeleton effect of PSS PEs within the multilayer films, independent of external pH, the composition of blend multilayer films has been analyzed with FT-IR. Figure 2.7 shows the IR spectra of PSS in the blend multilayer films with different blend ratios of PSS and PMAA before (open symbols) and after (closed symbols) the post-treatment at pH 2.0 for 10 min. The FT-IR spectra of PSS shows the characteristic peak at 1035 cm^{-1} for the stretching vibration of SO_3^- groups.[44] The amount of PSS retained within the multilayer films is almost constant even after the post-treatment, regardless of the blend ratios of PSS and PMAA. On the other hand, weak PEs shows significant differences in IR absorbance when as-prepared films were subject to the post-treatment. Figure 2.8 shows that as the content of PSS is increased, the degree of decrease in the IR absorbance of PMAA is reduced and also more protonated PMAA chains confirmed by a peak at 1701 cm^{-1} remain within the blend film even after treatment. These results imply that every carboxylic group in PMAA chains is protonated at pH 2.0 but the protonated PMAA chains cannot easily escape from the blend multilayer films due to strong ionic crosslinking effect of PSS PEs. The remaining amount of LPEI also increases within the films as the PSS content within the

multilayer film is increased (Figure 2.9). These FT-IR analyses further support that pH-independent PSS chains serve as robust skeletons to resist the total disruption of $(LPEI/PMAA)_n$ weak PE multilayer films when the multilayer film is subject to treatment in acidic media. As a result, the burst disruption of multilayer films is dramatically suppressed and the release kinetics could be finely tuned simply by varying the PSS content within the multilayer films.

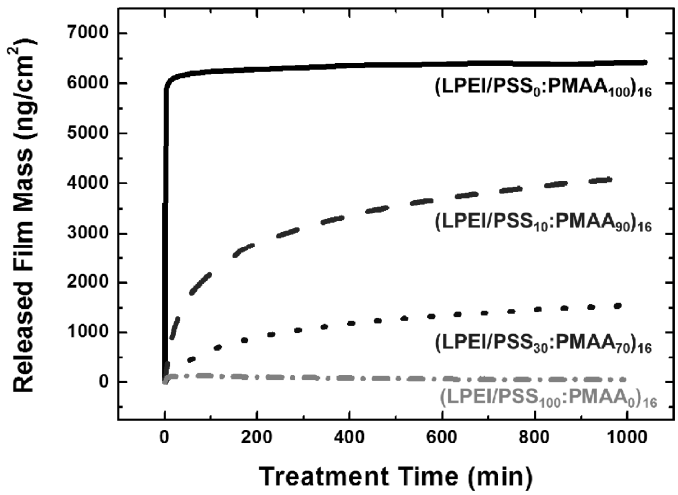

Figure 2.5. Release kinetics (released mass (ng/cm^2) plotted against time (min)) for blend multilayer films with different blend ratios of PSS and PMAA polyanions, monitored by QCM-D.

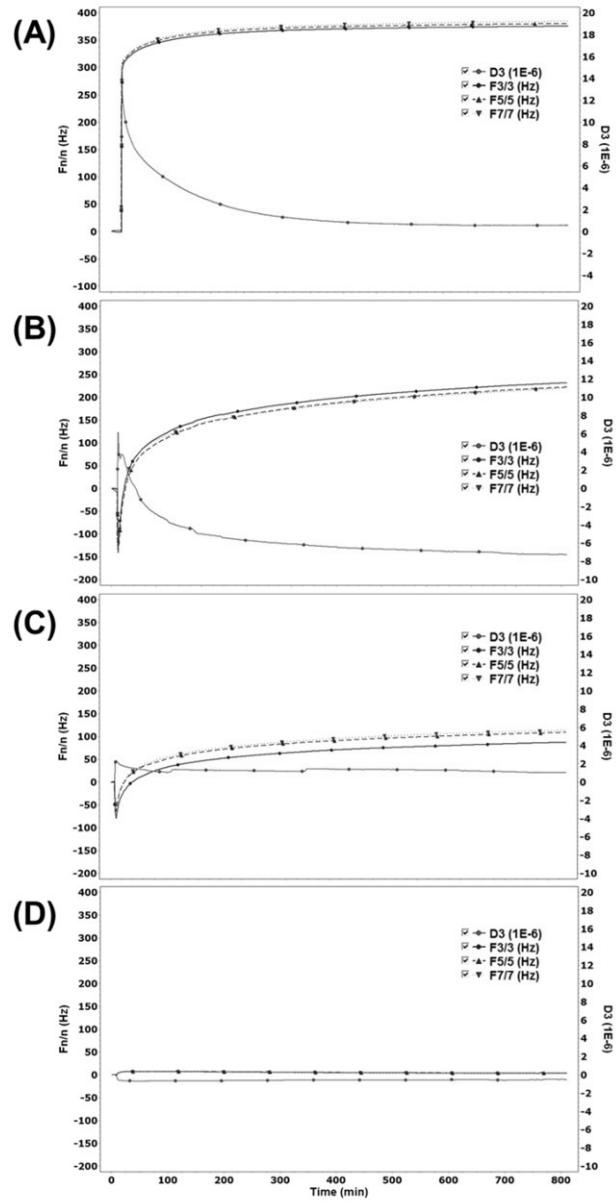

Figure 2.6. QCM raw data of blend multilayer films, $[LPEI/PSS:PMAA]_{16}$ with different blend ratios (PSS:PMAA = (A) 0:100, (B) 10:90, (C) 30:70 and (D) 100:0). Frequency changes (blue) with overtone numbers (n = 3 (circle, solid line), 5 (triangle, dash), 7 (down triangle, dots)) and dissipation changes (red) were monitored as a function of post-treatment time in pH 2.0 water.

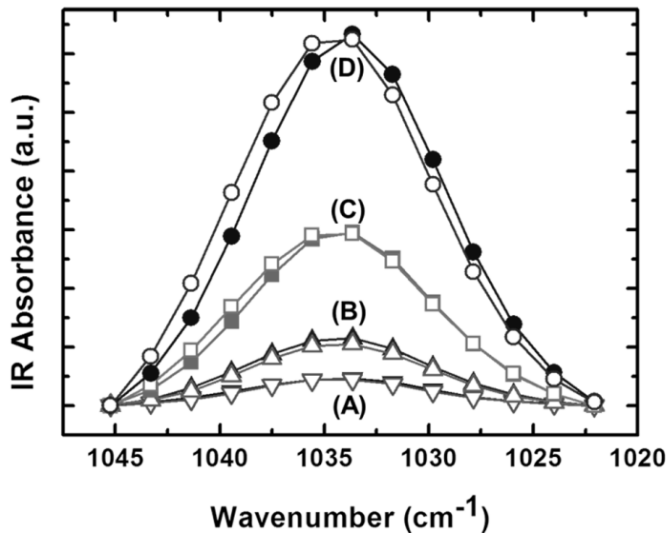

Figure 2.7. FT-IR spectra of PSS on the region of S=O symmetric stretching of SO_3^- for as-prepared films (open symbols) and the films post-treated at pH 2 (closed symbols) with different blend ratios in PSS:PMAA polyanion mixtures ((A)▼10:90, (B) ▲20:80, (C) ■30:70, and (D) ●100:0).

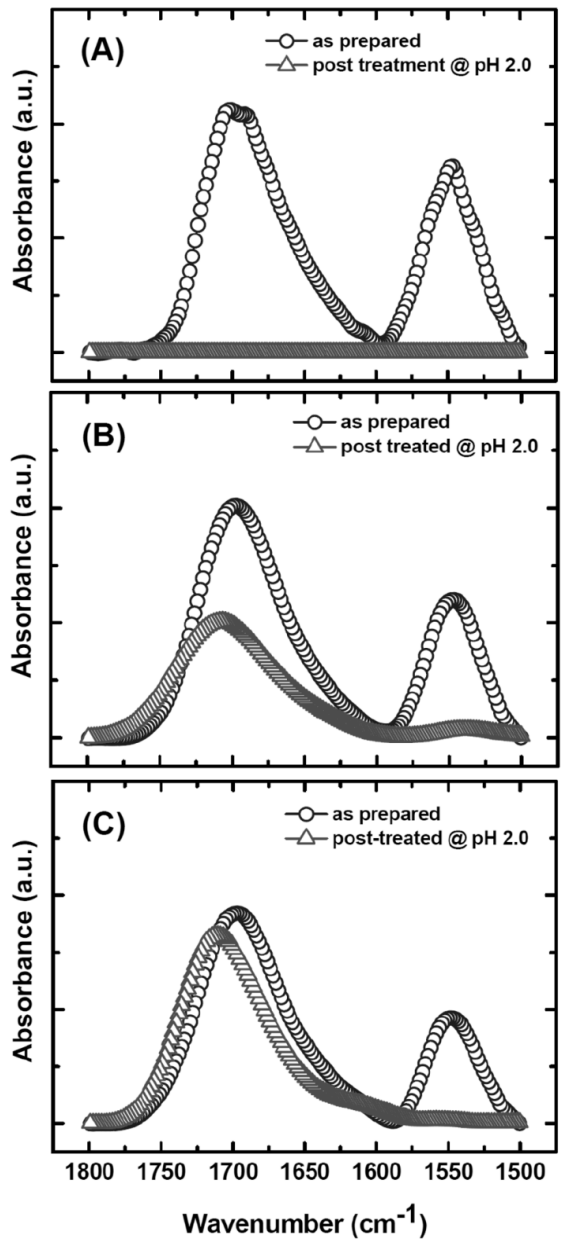

Figure 2.8. FT-IR absorption spectra of PMAA chains, in the regions at 1701 and 1540 cm^{-1} associated with COOH and COO^- groups, for as-prepared films (circle symbols) and the films post-treated at pH 2.0 (triangle symbols) at different blend ratios in PSS:PMAA polyanion mixtures ((A) 0:100; (B) 10:90; (C) 30:70).

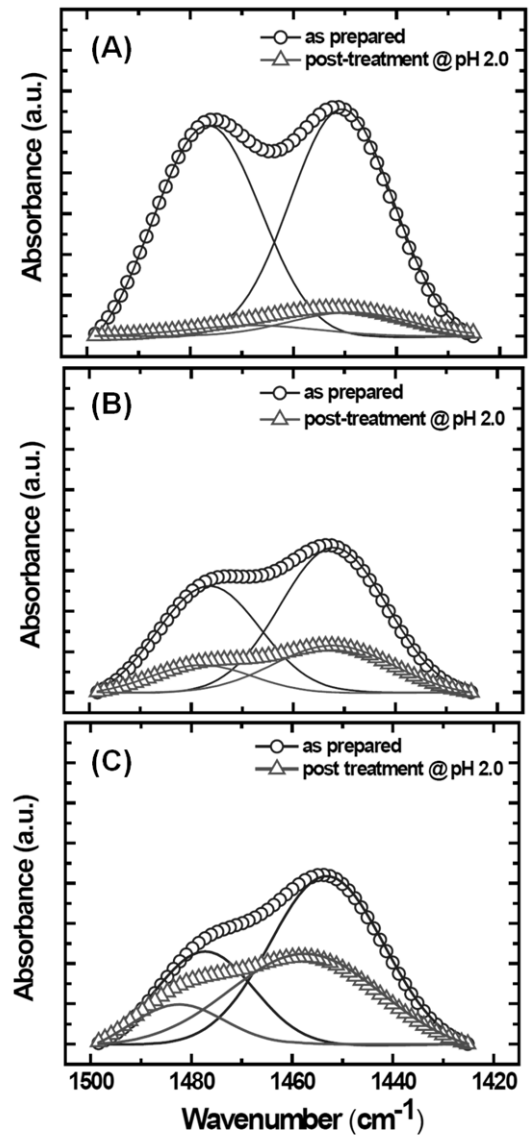

Figure 2.9. FT-IR spectra of LPEI chains, in the regions at 1450 and 1480 cm^{-1} associated with NH bending peak connected to CH_2 scissors, for as-prepared films (circle symbols) and the films post-treated at pH 2 (triangle symbols) at different blend ratios in PSS:PMAA polyanion mixtures ((A) 0:100; (B) 10:90; (C) 30:70).

2.4. Conclusion

A model controlled release platform triggered in acidic conditions (i.e., pH 2.0) has been developed based on blend multilayer films incorporating the mixtures of strong and weak PEs. LbL systems containing, $[LPEI/PSS_x:PMAA_{100-x}]_{16}$, have been prepared by the spin-assisted deposition method, which offers well-defined internal structure with linear growth behavior. The controlled release behavior as a function of blend ratio of PSS and PMAA has been investigated in terms of the changes in internal structure as well as the release kinetics at the nanoscale level. As the incorporation ratio of PSS is increased within the blend multilayer film, the precipitous disruption of a film solely composed of weak PEs is dramatically suppressed and switches to surface erosion. The released mass and kinetics of the film could be finely tuned as a function of the blend ratio. In addition, we have elucidated that PSS PEs provide the robust skeletons within the blend multilayer films, independent of pH variation, as shown by the comparison of the analysis of SLD profiles as well as FT-IR absorbance of model films before and after treatment. The approaches taken in the present study for the controlled release represent the improved release property of multilayer thin films. Therefore, the controlled release behavior of model blend multilayer systems triggered at low pH offers the opportunity to design versatile polymeric delivery platforms responding to external stimuli for various biomedical applications.

2.5. References

(1) Tang, Z. Y.; Wang, Y.; Podsiadlo, P.; Kotov, N. A., *Adv Mater* **2006,** *18* (24), 3203-3224.

(2) Boudou, T.; Crouzier, T.; Ren, K. F.; Blin, G.; Picart, C., *Adv Mater* **2010,** *22* (4), 441-467.

(3) Jang, Y.; Park, S.; Char, K., *Korean J Chem Eng* **2011,** *28* (5), 1149-1160.

(4) Swiston, A. J.; Cheng, C.; Um, S. H.; Irvine, D. J.; Cohen, R. E.; Rubner, M. F., *Nano Lett* **2008,** *8* (12), 4446-4453.

(5) Wood, K. C.; Boedicker, J. Q.; Lynn, D. M.; Hammond, P. T., *Langmuir* **2005,** *21* (4), 1603-1609.

(6) Ono, S. S.; Decher, G.; *Nano Lett* **2006,** 6 (4), 592-598.

(7) De Geest, B. G.; Sanders, N. N.; Sukhorukov, G. B.; Demeester, J.; De Smedt, S. C., *Chem Soc Rev* **2007,** *36* (4), 636-649.

(8) Kim, B. S.; Smith, R. C.; Poon, Z.; Hammond, P. T., *Langmuir* **2009,** *25* (24), 14086-14092.

(9) Hong, J.; Kim, B. S.; Char, K.; Hammond, P. T., *Biomacromolecules* **2011,** *12* (8), 2975-2981.

(10) Jomaa, H. W.; Schlenoff, J. B., *Macromolecules* **2005,** *38* (20), 8473-8480.

(11) Wong, J. E.; Gaharwar, A. K.; Muller-Schulte, D.; Bahadur, D.; Richtering, W., *J Colloid Interf Sci* **2008,** *324* (1-2), 47-54.

(12) Volodkin, D. V.; Madaboosi, N.; Blacklock, J.; Skirtach, A. G.; Mohwald, H., *Langmuir* **2009,** *25* (24), 14037-14043.

(13) Wood, K. C.; Zacharia, N. S.; Schmidt, D. J.; Wrightman, S. N.; Andaya, B. J.; Hammond, P. T., *P Natl Acad Sci USA* **2008,** *105* (7), 2280-2285.

(14) Etienne, O.; Schneider, A.; Taddei, C.; Richert, L.; Schaaf, P.; Voegel, J. C.; Egles, C.; Picart, C., *Biomacromolecules* **2005,** *6* (2), 726-733.

(15) Kharlampieva, E.; Ankner, J. F.; Rubinstein, M.; Sukhishvili, S. A., *Phys Rev Lett* **2008,** *100* (12), 128303.

(16) Jia, Y.; Fei, J.; Cui, Y.; Yang, Y.; Gao, L.; Li, J., *Chem Comm* **2011**, 47, 1175-1177.

(17) Song, W.; He, Q.; Mohwald, H.: Yang, Y.; Li, J., *J Control Release* **2009,** 139, 160-166.

(18) Mendelsohn, J. D.; Barrett, C. J.; Chan, V. V.; Pal, A. J.; Mayes, A. M.; Rubner, M. F., *Langmuir* **2000,** *16* (11), 5017-5023.

(19) Lutkenhaus, J. L.; McEnnis, K.; Hammond, P. T., *Macromolecules* **2008,** *41* (16), 6047-6054.

(20) Vander, A. J.; Sherman, J. H.; Luciano, D. S., *Human physiology: the mechanisms of body function*. McGraw-Hill: New York, 1994.

(21) Estey, T.; Kang, J.; Schwendeman, S. P.; Carpenter, J. F., *J Pharm Sci* **2006,** 95 (7), 1626-1639.

(22) Risbud, M. V.; Hardikar, A. A.; Bhat, S. V., Bhonde, R. R., *J Control Release* **2000,** 68, 23-30.

(23) Rao, V. M.; Engh, K.; Qiu, Y., *Int J Pharm* **2003,** 252, 81-86

(24) Cho, J. H.; Quinn, J. F.; Caruso, F., *J Am Chem Soc* **2004,** *126* (8), 2270-2271.

(25) Quinn, A.; Such, G. K.; Quinn, J. F.; Caruso, F., *Adv Funct Mater* **2008,** *18* (1), 17-26.

(26) Quinn, A.; Tjipto, E.; Yu, A. M.; Gengenbach, T. R.; Caruso, F., *Langmuir* **2007,** *23* (9), 4944-4949.

(27) Cho, J.; Char, K.; Hong, J. D.; Lee, K. B., *Adv Mater* **2001,** *13* (14), 1076-1078.

(28) Kharlampieva, E.; Kozlovskaya, V.; Chan, J.; Ankner, J. F.; Tsukruk, V. V., *Langmuir* **2009,** *25* (24), 14017-14024.

(29) Turon, X.; Rojas, O. J.; Deinhammer, R. S., *Langmuir* **2008,** *24* (8), 3880-3887.

(30) Commercial materials, instruments and equipment are identified in this paper in order to specify the experimental procedure as completely as possible. In no case does such identification imply a recommendation or endorsement by the National Institute of

Standards and Technology nor does it imply that the materials, instruments, or equipment identified are necessarily best available for the purpose.

(31) Kienzle, P. A.; O'Donovan, K. V.; Ankner, J. F.; Berk, N. F.; Majkrzak, C. F., http://www.ncnr.nist.gov/reflpak. 2000-2006.

(32) Parratt, L. G., *Phys Rev* **1954,** *95* (2), 359-369.

(33) Yoo, P. J.; Zacharia, N. S.; Doh, J.; Nam, K. T.; Belcher, A. M.; Hammond, P. T., *Acs Nano* **2008,** *2* (3), 561-571.

(34) Yoo, P. J.; Nam, K. T.; Qi, J. F.; Lee, S. K.; Park, J.; Belcher, A. M.; Hammond, P. T., *Nat Mater* **2006,** *5* (3), 234-240.

(35) Lee, Y. M.; Park, D. K.; Choe, W. S.; Cho, S. M.; Han, G. Y.; Park, J.; Yoo, P. J., *J Nanosci Nanotechno* **2009,** *9* (12), 7467-7472.

(36) Chao, G. T.; Deng, H. X.; Huang, Q.; Jia, W. J.; Huang, W. X.; Gu, Y. C.; Tan, H. P.; Fan, L. Y.; Liu, C. B.; Huang, A. L.; Lei, K.; Gong, C. Y.; Tu, M. J.; Qian, Z. Y., *J Polym Res* **2006,** *13* (5), 349-355.

(37) Hubsch, E.; Ball, V.; Senger, B.; Decher, G.; Voegel, J. C.; Schaaf, P., *Langmuir* **2004,** *20* (5), 1980-1985.

(38) Sui, Z. J.; Schlenoff, J. B., *Langmuir* **2004,** *20* (14), 6026-6031.

(39) Hiller, J.; Rubner, M. F., *Macromolecules* **2003,** *36* (11), 4078-4083.

(40) Kharlampieva, E.; Kozlovskaya, V.; Ankner, J. F.; Sukhishvili, S. A., *Langmuir* **2008,** *24* (20), 11346-11349.

(41) Fredin, N. J.; Zhang, J.; Lynn, D., *Langmuir* **2005,** 21, 5801-5811.

(42) Quinn J.; Caruso F., *Langmuir* **2004,** 20, 20-22.

(43) Felix, O.; Zheng, Z. Q.; Cousin, F.; Decher, G., *Cr Chim* **2009,** *12* (1-2), 225-234.

(44) Kuo, C.-W.; Wen, T.-C., *European Polymer Journal* **2008,** *44* (11), 3393-3401.

Chapter 3.[*]

Controlled Release of Model Multilayer Films Containing Weak Polyelectrolytes with Different Molecular Weights

3.1. Introduction

The layer-by-layer (LbL) deposition is a powerful method to engineer functionalities of multilayer thin films by controlling intermolecular interactions between internal layers. Since the fundamental concept of the LbL assembly of oppositely charged polyelectrolytes (PEs) was introduced,[1] many researchers have investigated the adsorption behavior of diverse polymer chains into multilayer films as a function of deposition parameters and types of intermolecular interactions.[2-6] Consequently, many functional multilayer platforms based on the LbL assembly have been developed for extensive applications, as well documented in several review articles.[5-12]

In addition to the adsorption behavior of polymers into multilayer films, the release of active ingredients and/or the disintegration mechanism of multilayer films have recently received much attention to develop functional controlled release platforms.[12-14] In particular, stimuli-triggered release platforms based on the LbL assembly have been realized as a function of external stimuli such as pH,[15-16] temperature[17-18] or ionic strength[19-21] to name a few, because the responses to such stimuli could increase functionalities and applications of the multilayer films. Furthermore, many research groups have made several attempts to

[*] This chapter is based on a paper from Yeongseon Jang, Jooyeon Seo, Bulent Akgun, Sushil Satija, and Kookheon Char, *Macromolecules* **2013**, 46, 4580-4588. Copyright 2013 American Chemical Society

control the stimuli-triggered disintegration behavior of LbL multilayer films through thermal or chemical crosslinking,[22] the insertion of diffusion barrier layers[23] or blending with strongly binding materials[24] into each bilayer. However, such post-treatment and the incorporation of strong binding materials could cause problems such as the decrease in ingredient activity or the interfacial disruption between internal layers.[24]

In this regard, the molecular weight (MW) of PE chains could be one of critical and intrinsic control parameters to tune the disintegration behavior of multilayer films without additional post-treatments or the insertion of other strongly binding molecules. It has been reported that the PE MW has a great effect on the surface characteristics and adsorption properties of the multilayer films[25-28] as well as on the pH-triggered pore formation of multilayer films.[29-30] However, to our knowledge, there are few reports dealing with the disintegration mechanism of multilayer films as a function of MW of PE chains incorporated,[31] especially with quantitative analysis that provides both chain- and thin film structural-level of understanding.[32] We believe that more detailed analysis on the internal structure of multilayered films upon external stimuli, such as swelling, rearrangements, and disintegration modes, is still lacking in the case of well-defined multilayers prepared by the spin-assisted LbL deposition based on the electrostatic interactions between weak PE pairs. Furthermore, revealing the correlations between structural changes and viscoelastic responses of the multilayer films as a function of PE MW could provide further insights on the controlled disintegration of designed multilayer films.

Herein, we have studied the MW-dependent disintegration of weak PE multilayer films consisting of linear poly(ethylene imine) (LPEI) and poly(methacrylic acid) (PMAA), when the electrostatic interactions between LPEI and PMAA layers were diminished by post-treatment at low pH. We demonstrate that the controlled disintegration of the $[LPEI/PMAA]_n$

multilayer film is possible by controlling PMAA MW, based on NR, and the corresponding dissipation energy of the multilayer films during the post-treatment was also monitored by QCM-D. QCM-D is useful for monitoring the dynamics of adsorption or desorption of materials deposited on quartz crystal substrates and the changes in viscoelastic properties of adsorbed films in aqueous environment,[33-35] allowing us to quantitatively analyze the *in-situ* disintegration behavior of the multilayer films in the present study. By combining both NR and QCM-D measurements and analyses, the different disintegration modes of multilayer films were identified concomitantly with the changes in the energy dissipation within the films as a function of PE MW. The results reported in the present study would provide both chain- and structural-level of understanding as to the effect of PE MWs on the disintegration modes and kinetics of multilayer films, giving insights for the development of functional controlled release platforms based on the spin-assisted LbL deposition.

3.2. Experimental Section

Materials.[36] Linear poly(ethyleneimine) (LPEI, M_w = 25,000 g/mol) and poly(methacrylic acid)s (PMAA, M_w = 15,000 g/mol and M_w = 100,000 g/mol) were purchased from Polysciences. PMAAs with different molecular weights (M_w = 32,400 g/mol (PDI = 1.08) and M_w = 226,000 g/mol (PDI = 1.08)) and deuterated PMAA (d-PMAA, M_w = 43,000 g/mol (PDI = 1.08) and M_w = 180,000 g/mol (PDI = 1.10)) were purchased from Polymer Source. All polymers were used as received. Silicon wafers and Au sensor crystals (QSX 301, Q-Sense) were used as substrates to prepare blend multilayer films for further characterization.

Preparation of Weak Polyelectrolyte Multilayer Films. Weak polyelectrolytes (PEs), LPEI and PMAA, were chosen for cationic and anionic polymer solutions to prepare LbL multilayer films based on the electrostatic interactions. All the polymers were initially dissolved in 18 MΩ Milli-Q water with concentrations of 0.01 M based on repeat units and then the polymer solutions were adjusted to pH 5.0 by adding diluted HCl or NaOH solutions. All the substrates were treated with piranha solution, mixtures of 70 vol % H_2SO_4 and 30 vol % H_2O_2, for 20 min at room temperature, followed by thorough washing with DI water and drying under nitrogen stream. The multilayer films with different molecular weights (MWs) of PMAA, $[LPEI/PMAA_{MW}]_n$ (n: number of bilayers), were prepared on the piranha-treated hydrophilic substrates by the spin-assisted LbL deposition method with a spin-rate of 3000 rpm for 30 sec for each deposition, followed by two consecutive washing spin steps to remove excess PEs with pH 5.0 DI water. To check the effect of LbL deposition method on the adsorption behavior of PMAAs with different MWs, we also prepared the multilayer films by the dip-assisted LbL deposition: dipping into each PE solution for 15 min, followed by three consecutive washing steps for 2 min, 1 min, 1 min with gentle agitation as programmed in a Carl Zeiss DS50 slide stainer.

Characterization and Post-Treatment of Weak PE Multilayer Films. Total film thicknesses in dried condition were measured by a variable-angle multiwavelength ellipsometer (Gaertner L2W15S830, Gaertner Scientific Corp.). The pH-triggered changes in the internal structure of the multilayered films were monitored by neutron reflectivity (NR) as described in our previous report.[24] In order to secure enough neutron contrast as well as to facilitate the monitoring of the film internal structure based on NR, the multilayer films were constructed by replacing protonated PMAA layers with *d*-PMAA chains which have similar MW in every 4th bilayer deposition. These multilayer structures yield four peaks in the neutron scattering length density (SLD) profiles and all the NR data were fitted with the LbL box model, as also described in details in our previous paper.[24] From the changes in the position, width, and amplitude of the peaks in the SLD profiles, we obtained the information on the disintegrated amount (%) and reduced thickness (%) of the post-treated films as compared to the as-casted films. To trigger the internal structural changes in the multilayer films, as-prepared films were immersed in pH 2.0 water for 10 min and then gently washed with same water used for the post-treatment, followed by relevant drying process under N_2 stream. The degree of ionization (%) of PMAA PEs incorporated into the multilayer films was characterized with FT-IR (FT-IR-200 spectrometer, JASCO Corp.). The multilayer films for FT-IR measurements were prepared on CaF_2 crystals, which are transparent to IR light. Furthermore, the release and swelling kinetics based on the corresponding changes in viscoelastic properties of multilayer films were monitored by QCM-D and Q-Tools analysis.

Quartz Crystal Microbalance with Dissipation Monitoring (QCM-D). The pH-triggered changes in both frequency (Δf_n) and dissipation (ΔD_n) of a multilayer film deposited on an Au sensor crystal (QSX301) were monitored by QCM-D (Q-Sense D300, Q-Sense AB). In the QCM-D measurements, the changes in the resonance frequency (Δf) and the dissipation

factor (ΔD) are mainly related to mass uptake or loss at the surface of a quartz sensor and viscoelasticity of the film, respectively. The basic principle and measurement techniques of QCM-D measurements have been described in detail elsewhere.[33-35, 37-38] Every multilayer film was stabilized in pH 5.0 water, which is the same pH for the initial film deposition, for more than 100 min in order to set the baseline to monitor the pH-triggered changes in QCM frequency as well as dissipation energy in water setting. After stabilization, 0.8 ml of low pH water (i.e., pH 3.0, 2.5, 2.2 or 2.0) was injected to the sample chamber. The applied voltage is sequentially pulsed across the Au sensor crystal, allowing the shear wave to dissipate as well as the simultaneous measurements of absolute dissipation and absolute resonant frequency of the crystal for all four overtones (n = 1, 3, 5 and 7, i.e., 5, 15, 25 and 35 MHz). These overtones were used to characterize the viscoelastic properties of multilayer films adsorbed onto Au sensor crystals. All the measurements were taken at 25 ± 0.02 ^{0}C. Since Δf_1 and ΔD_1 were typically noisy due to insufficient energy trapping, frequency changes in the 3rd overtone $\Delta f_3/3$ (Hz) were compared among the multilayer films with different MWs. Particularly, in order to compare the disintegration kinetics of multilayer films with different MWs, the $\Delta f_3/3$ (Hz) as a function of post-treatment time was converted into the relative percentage (%) of the final stabilized frequency after sufficient disintegration of films because the adsorbed film mass is slightly different in each sample.

3.3. Results and Discussion

The model weak PE multilayer films, $[LPEI_{25k}/PMAA_{MW}]_n$ (n = number of bilayers), were composed of positively charged linear poly(ethylene imine) (LPEI) with MW of 25,000 g/mol and negatively charged poly(methacrylic acid) (PMAA) with different weight average MWs of 15,000, 32,400, 100,000 and 226,000 g/mol. The detailed characteristics of PEs used in the present study are summarized in **Table S1** in Supporting Information.

3.3.1. Adsorption Behavior of Weak Polyelectrolyte (PE) Multilayer Films with Different Molecular Weights (MWs)

Weak PE LbL films show different bilayer thickness growth depending on the deposition methods. The multilayer films deposited by the spin-assisted LbL deposition demonstrated the similar growth rate for PMAA chains with different MWs (Figure 3.1A), while the ones created by the dip-assisted LbL deposition showed considerably different growth rate depending on MW of PMAA chains (Figure 3.1B). In the case of the spin-assisted LbL deposition, the adsorption of PE chains and the elimination of water molecules are almost simultaneously achieved in a short time as well as the external centrifugal and air shear force at a high spinning rate have an effect on the thin film formation.[39] In particular, the air shear force driven by the spinning significantly enhances the surface planarization of the LbL films, and the PE chains are adsorbed onto oppositely charged surfaces with collapsed and tightly bound conformation regardless of their MWs. This more laterally stretched conformation causes the film to be thinner, as shown in Figure 3.1. The spin-assisted LbL films based on the electrostatic interactions have the persistent layers with the least internal mixing and smooth air surfaces when compared with the dip-assisted LbL films.[40]

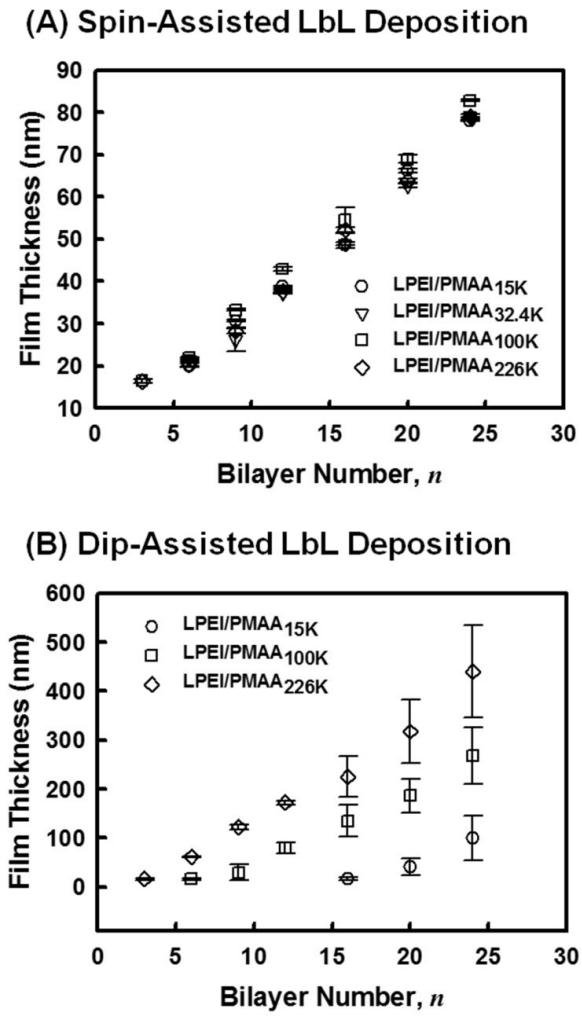

Figure 3.1. Growth curves in the bilayer thickness of weak polyelectrolyte multilayer films, $[LPEI_{25k}/PMAA_{MW}]_n$, with different molecular weights (○15k, ▽32.4k, □100k and ◇226k) of PMAA prepared by the (A) spin- and (B) dip-assisted LbL deposition. Error bars denote ±1 standard deviations.

On the other hand, in the dip-assisted LbL films, the MW of the PMAA chains has a significant effect on the growth of bilayer thickness and total film thickness due to their different characteristic size (i.e., radius of gyration (<R_g>)) in dilute solutions as well as the different conformational state depending on MW and charge density.[41] The PE chains of which diffusion is driven by the electrostatic interactions are adsorbed onto a substrate by almost maintaining their own conformation and characteristic size in dilute dipping solutions because any other external forces do not have an effect on the adsorption of the PE chains in contrast to the spin-assisted LbL deposition. Since the weak PE chains, LPEI and PMAA investigated in this study, were deposited at pH 5.0 close to their pK_a values (i.e., 4.8 – 5.0 for LPEI[42] and 5.5 – 6.0 for PMAA[43]), the partially charged weak PE chains typically take loop and tail conformations during the dipping-based LbL deposition. It is well-known that the polymer chains adopting more loopy conformations yield thicker layers.[44] As a result, in the present study, every PMAA chain adopts the coiled conformation at deposition pH 5.0 with different characteristic size depending on the PE MW.[45] Therefore, in the dip-assisted LbL deposition, the bilayer growth increases with the increase in MW of PMAA chains deposited within the multilayered film.

From the comparison of multilayer growth behavior between the dip- and spin-assisted LbL deposition methods, it is confirmed that the MW of PE chains employed for the LbL deposition significantly influences the interaction between polyanion and polycation layers, particularly in aqueous media. Therefore, in order to investigate the MW effect on the disintegration of LbL films, we prepared model weak PE multilayer films by the spin-assisted LbL deposition, showing the similar growth rate and conformations, independent of PE MW, in adsorbed state between samples (i.e., multilayered films prepared with different PE MWs). The different adsorption behavior with different PE MWs, as shown in the dip-based

deposition, could be an additional parameter to be considered to interpret the disintegration behavior of multilayer films. In addition, the spin-assisted LbL films provide well-ordered internal structures, which, in turn, facilitate the monitoring of the changes in internal structure using neutron reflectivity (NR), as well demonstrated in Figure 3.2.

3.3.2. Changes in the Internal Film Structures Monitored by NR

NR measurements have been performed to investigate the disintegration characteristics by monitoring the structural changes in the internal layers of weak PE multilayer films as a function of MWs. As shown in Figure 3.2, every spin-assisted $[(LPEI_{25k}/PMAA_{MW})_3(LPEI_{25k}/d\text{-}PMAA_{MW})_1]_4$ multilayer film has a well-organized internal structure, which is confirmed by regularly spaced Bragg peaks in the NR data as well as well-defined four sharp peaks clearly evident in the SLD profiles. The alterations in the internal structures of these well-defined weak PE multilayer films were induced simply by changing the external solution pH.

Recently,[24] we have observed that the multilayer films with low MW, $[(LPEI/PMAA_{15k})_3(LPEI/d\text{-}PMAA_{43k})_1]_4$, led to burst erosion at pH 2 due to the complete dissociation of electrostatic binding sites between LPEI and low MW PMAA, which have a small number of repeat units in a single chain. However, the multilayer films composed of higher MW (i.e., 32.4k, 100k and 226k) PMAA chains demonstrate the maintained multilayer structures with different characteristics as a function of PMAA MW. In the case of the $[(LPEI/PMAA_{32.4k})_3(LPEI/d\text{-}PMAA_{43k})_1]_4$ multilayer film, the post-treated film loses approximately 30 % of its original mass, mostly from the top surface, along with 38 % reduction in film thickness without disrupting the well-ordered structure close to the substrate.

This result indicates that protonated PMAA chains and loosely bound LPEI chains rapidly disintegrate and are released all together from the top film surface due to faster diffusion of the chains near air interface into bulk solution when compared with the chains buried deep into the film.[46] It is also confirmed that the remaining layers on the substrate side are more mixed (Figure 3.2A) than as-prepared state, which is confirmed by the fact that the neutron SLD values for protonated layers are increased while the amplitude of the deuterated marker layers is decreased with broader interlayer roughness.

On the other hand, the post-treated multilayer film with higher MW, $[(\text{LPEI/PMAA}_{100k})_3(\text{LPEI/}d\text{-PMAA}_{198k})_1]_4$, almost maintained its internal structure and lost only about 3 % of its original mass from the top surface (Figure 3.2B). The total film thickness after the post-treatment is reduced only 11 % of its initial thickness. In addition, we noticed that the bottom layers were almost intact after the post-treatment while there is some mixing between protonated layers and the deuterated marker layer near the top surface when compared with the as-prepared film. Overall, it seems that the internal rearrangements of PE chains are more dominant, during the same post-treatment time of 10 min, when compared to the fast disintegration of multilayer films containing shorter PMAA chains (15k and 32.4k). The difference in the film profile after the post-treatment could be explained by the slower desorption and dissolution kinetics of high MW PE chains.

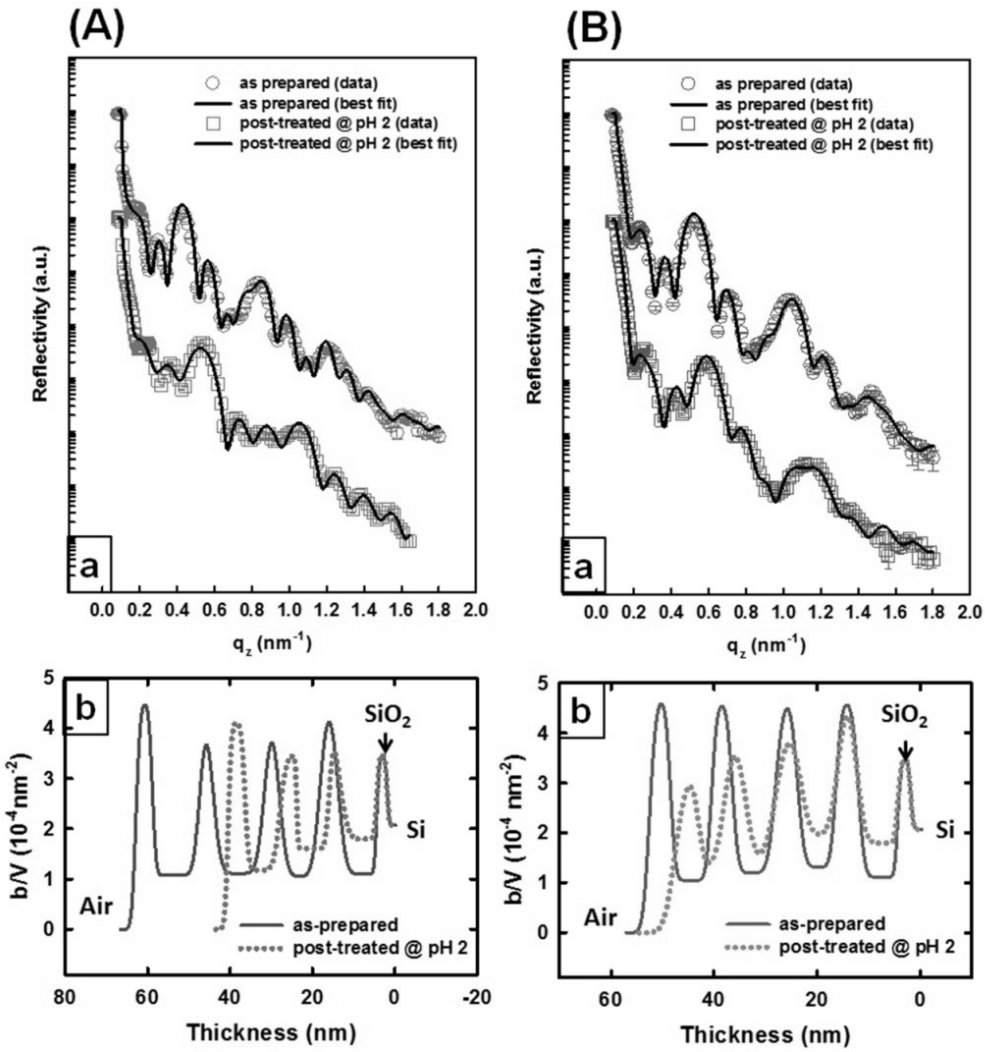

Figure 3.2. Neutron reflectivity (NR) curves with best fits in panel a and SLD profiles in panel b of weak PE multilayer films with (A) low MWs, $[(LPEI_{25k}/PMAA_{32.4k})_3/(LPEI_{25k}/d\text{-}PMAA_{43k})_1]_4$ and (B) high MWs, $[(LPEI_{25k}/PMAA_{100k})_3/(LPEI_{25k}/d\text{-}PMAA_{198k})_1]_4$. Films initially deposited at pH 5 are represented by circle symbols in the reflectivity panels and by solid lines in the SLD panels while the films post-treated at pH 2 for 10 min are represented by square symbols in the reflectivity panels and by dotted lines in the SLD panels.

Since the initial number of electrostatic binding sites per single PMAA chain interacting with LPEI chains is believed to be the predominant factor controlling the film disintegration kinetics, the well-ordered multilayer film with higher PMAA MW demonstrates the preference toward maintaining its internal structures before it is fully disintegrated into bulk solution. From the maintenance of the Bragg peaks in the raw neutron reflectivity data and the SLD profile after post-treatment, we also safely confirm that the main skeleton of the $[(LPEI/PMAA_{100k})_3(LPEI/d\text{-}PMAA_{198k})_1]_4$ multilayer film is almost protected with well-ordered internal layers even though some LPEI and PMAA chains disintegrate from top surface, as compared to $[(LPEI/PMAA_{32.4k})_3(LPEI/d\text{-}PMAA_{43k})_1]_4$ film post-treated at same condition.

Based on the NR results, it is clearly demonstrated that the protonation of PMAA chains and corresponding charge misbalance which was triggered by post-treatment at pH 2 induce the disintegration of weak PE multilayer films from the top surface but the simple increase in PMAA MW of the multilayer films could transform from the burst erosion (i.e., immediate film disintegration) to the surface erosion (i.e., delayed disintegration from top film surface) in more controlled manner.

3.3.3. Disintegration Kinetics and Corresponding Changes in Dissipation Energy Monitored by QCM-D

NR measurements provide useful information on the structural changes within multilayer films but usually take long time to obtain data, thus not feasible to measure short time release kinetics. As a complementary technique, QCM-D was employed to investigate the film disintegration kinetics and to obtain information on film properties and structural

transformations during the post-treatment.

The time for the complete disintegration of $[LPEI/PMAA_{MW}]_{16}$ multilayer film masses dramatically changes ranging from 2 min to 5 days, depending on the MW of PMAA chains incorporated into the multilayer films (Figure 3.3A). An initial burst in the release profile was observed when a low MW $[LPEI_{25k}/PMAA_{15k}]_{16}$ film was subject to post-treatment with pH 2.0. The charge imbalance, triggered by the post-treatment at low pH, between adjacent layers (i.e., the increase in positive charges of LPEI chains at the expense of the decrease in negative charges of PMAA chains) causes the significant reduction in binding interactions, allowing the PE chains to disintegrate into bulk solution. However, the disintegration kinetics became slower as the MW of PE chains incorporated into the multilayer film was increased. In addition, we were able to monitor the considerable swelling of the films for longer time before the complete disintegration of the films when higher MW PMAA chains were incorporated into the multilayer films. The negative sign in frequency shifts which is clearly shown for the cases of the $[LPEI_{25k}/PMAA_{100k}]_{16}$ and $[LPEI_{25k}/PMAA_{226k}]_{16}$ multilayer films implies that the films gain some weight relative to the initial state deposited at pH 5.0. Such additional swelling, typically observed with high MW PE multilayer films, indicates that the multilayer films containing higher MW PEs tend to retain the well-ordered internal structure before full disintegration into bulk solution partly due to relatively high penalty for conformational change. Nevertheless, the masses of multilayer films containing high MW PMAA chains, $[LPEI_{25k}/PMAA_{100k}]_{16}$ and $[LPEI_{25k}/PMAA_{226k}]_{16}$, gradually decrease in the swelling region, which corresponds to the NR results measured after drying the film show the small disintegration in top surface with rearranged internal layers after the post-treatment for 10 min. Such slow disintegration kinetics of the multilayer films containing high MW PMAA chains are also hinted from the changes in dissipation energy (ΔD_n) as a function of post-

treatment time. The ΔD_n indicates the loss of energy stored in a vibration cycle, which yields useful information on the changes in viscoelasticity as well as structural transformation of the adsorbed film. The dissipation energy typically increases when a viscoelastic film is strained during oscillation or when a liquid is trapped in or moves out of the films due to the deformation of the films.[33-35] As shown in Figure 3.3B, the multilayer films with low MW PMAA chains, $[LPEI_{25k}/PMAA_{15k}]_{16}$ and $[LPEI_{25k}/PMAA_{32.4k}]_{16}$, do not have significant increase in the dissipation energy, implying that no viscoelastic layer is placed on the quartz crystal sensor because the short PE chains losing electrostatic interactions are rapidly detached from top surfaces of the film into bulk liquid upon post-treatment. On the other hand, $[LPEI_{25k}/PMAA_{100k}]_{16}$ and $[LPEI_{25k}/PMAA_{226k}]_{16}$ show the significant increase in dissipation energy. The dramatic increase in the dissipation energy thus points to the increase in film softness as well as considerable hydration. Furthermore, the large increase in dissipation energy upon water uptake is the typical phenomenon of a structural transformation from a stiff and compactly bound structure into a dissipative non-rigid structure.[38]

The relation of the changes in dissipation energy to the changes in viscoelasticity and the structures of the films could be further detailed by analyzing the frequency dependence in the QCM-D responses of adsorbed films. The viscoelastic adsorbed layer typically shows the value of dissipation energy higher than 2.0×10^{-6} and different responses to overtones.[38, 47-48] In the present study, notable difference in the QCM-D responses with different overtones (n = 3, 5, 7) as well as the significant increase in the dissipation energy was observed during the slow disintegration process of weak PE multilayer films containing high MW PMAA chains, $[LPEI_{25k}/PMAA_{100k}]_{16}$ and $[LPEI_{25k}/PMAA_{226k}]_{16,}$ as compared to low MW PE counterparts (Figure 3.4). The frequency dependency in the overtones indicates that the multilayer films

with high MW PEs, which quickly imbibe pH 2 water at the start of post-treatment, disintegrate very slowly from the top surfaces of the films, as confirmed by NR measurements, while the films gradually transform their initial compactly bound rigid structure into more viscoelastic and dissipative swollen state within the films. The fully swollen film finally reveals the disintegration characteristics with relatively rapid increase in frequency and decrease in dissipation energy, independent to overtones, which corresponds to the disintegration of a soft and viscoelastic film from a quartz sensor to bulk liquid. The completely dissociated or detached multilayer films show the plateaus in both frequency and dissipation energy at the end of QCM-D measurements. Based on the QCM-D monitoring of frequency and dissipation energy as well as of its overtone dependency, we also note that the disintegration mode of the multilayer film is composed of the sequence events, instant water uptake, swelling, rearrangement and decomposition, as well as the kinetics is strongly dependent on the MW of polymer chains incorporated into the multilayer films.

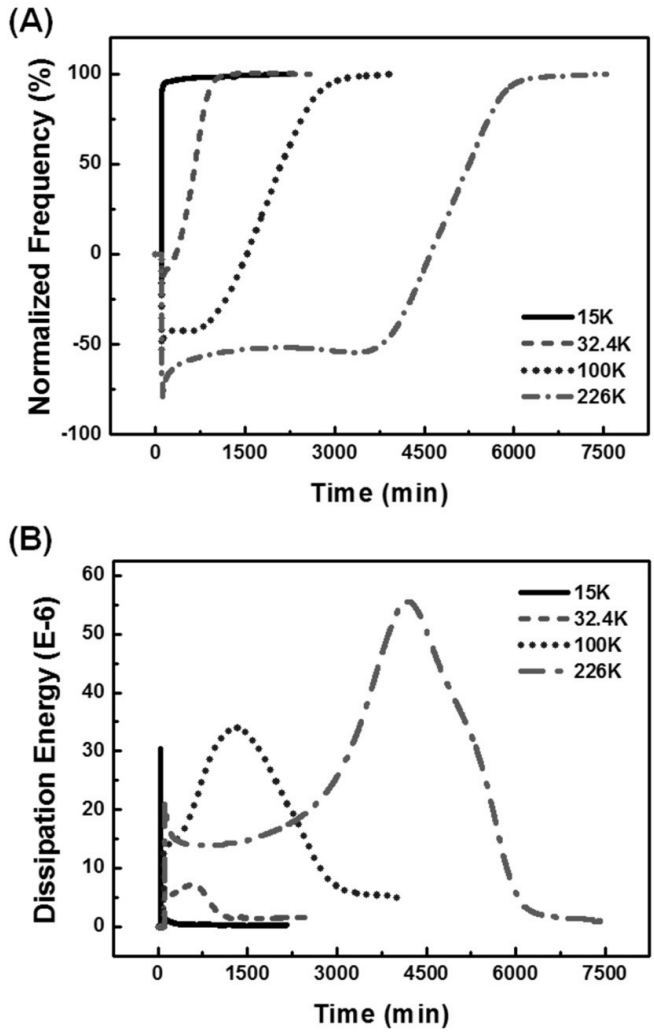

Figure 3.3. QCM-D monitoring on the changes in (A) normalized frequency (%) and (B) dissipation energy of weak PE multilayer films, $[LPEI_{25k}/PMAA_{MW}]_{16}$, with different molecular weights (solid line, 15k; dashes, 32.4k; dots, 100k; dash dots, 226k) of PMAA upon post-treatment of the multilayer films in pH 2.

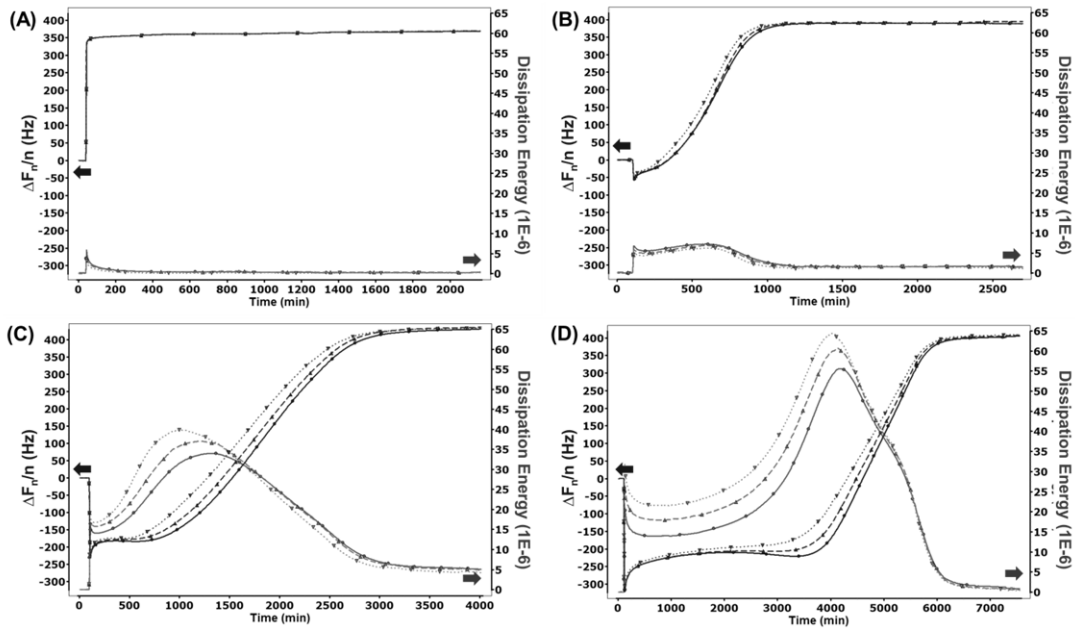

Figure 3.4. Changes in frequency (blue curves) and energy dissipation (red curves) during the release of multilayer thin films with high MWs ($[LPEI_{25k}/PMAA_{MWs}]_{16}$, MW = (A) 15k, (B) 32.4k, (C) 100k and (D) 226k) measured at three different overtones. The different curves within the same color correspond to third, fifth, and seventh overtones (n = 3 (solid line), 5 (dashes), and 7 (dots)) with driving frequencies of 15, 25, and 35 MHz, respectively.

3.3.4. Swelling Kinetics of Model Multilayer Films with Different MWs as a Function of External Solution pH

The swelling behavior observed in the high MW $[LPEI_{25k}/PMAA_{226k}]_{16}$ film triggered at pH 2 was not detected in the case of the low MW $[LPEI_{25k}/PMAA_{15k}]_{16}$ film presumably due to fast disintegration kinetics. To demonstrate the swelling behavior of low MW multilayer films before disintegration as well as to compare the swelling kinetics with high MW multilayer films, the responses in both frequency and dissipation of the multilayer films consisting of 15k and 226k PMAA chains were monitored by the sequential decrease in solution pH down to 2.2 instead of pH 2.0 (Figure 3.5).

The $[LPEI_{25k}/PMAA_{15k}]_{16}$ film shows the drastic changes in both frequency and dissipation energy even at pH value of 2.5 when it is compared with the $[LPEI_{25k}/PMAA_{226k}]_{16}$ film during the same post-treatment time of 10 min. These results clearly indicate that the multilayer film containing shorter MW PMAAs shows the rapid response in swelling at pH above 2.2 while the multilayer film containing higher MW PMAAs tends to maintain its original structure and rigidity for the same post-treatment condition. The slow kinetics in the sequential event involving swelling, rearrangements, and disintegration of high MW multilayer film could be originated from the more electrostatic binding units per PMAA chain as well as the fewer degrees of freedom of conformational rearrangements.

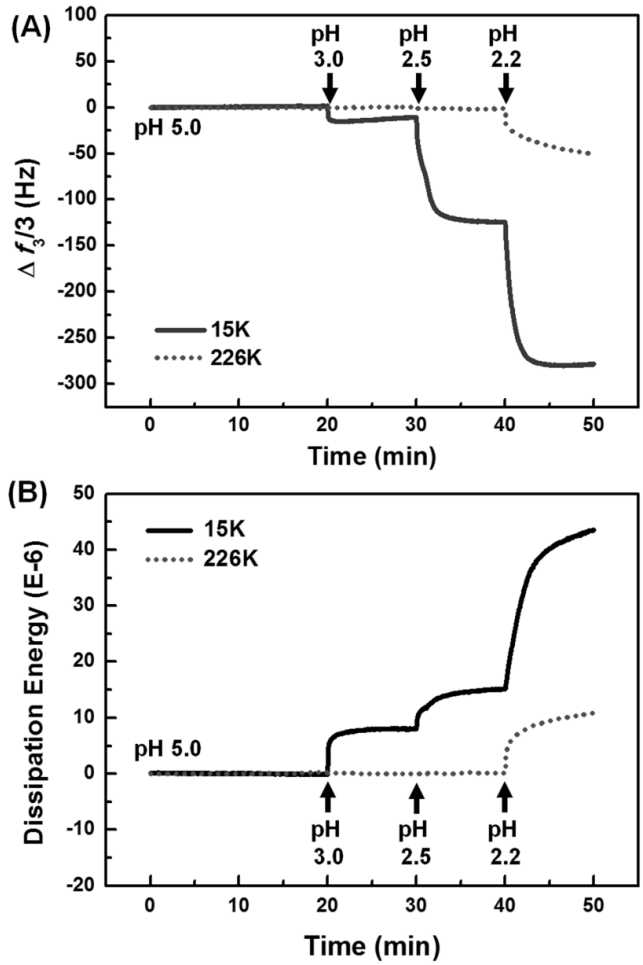

Figure 3.5. Responses in the (A) frequency shift ($\Delta f_3/3$ (Hz)) and (B) dissipation energy of weak PE multilayer films triggered by sequential low pH values (i.e., pH 3.0, 2.5, 2.2, respectively for 10 min): $[LPEI_{25k}/PMAA_{MW}]_{16}$ with low MW (15k, solid line) and high MW (226k, dotted line) of PMAA.

The degree of ionization of PMMA chains incorporated within the multilayer films would significantly affect the film swelling/disintegration behavior as a function of pH. In this regard, the degrees of ionization (%) of PMAA chains in the $[LPEI_{25k}/PMAA_{15k\ or\ 226k}]_{16}$ films were analyzed by FT-IR[49] when those multilayer films were initially prepared at pH 5 and then subject to post-treatment at pH 2.2 (Figure 3.6). We noted that the initial $[LPEI_{25k}/PMAA_{15k}]_{16}$ film containing about 24 % ionized COO^- groups in the PMAA layers represents only 5.3 % of COO^- groups after the post-treatment at pH 2.2. Similar trend was also found with the $[LPEI_{25k}/PMAA_{226k}]_{16}$ film showing around 21 % and 6.5 % of degrees of ionization in the PMAA layers before and after the post-treatment at pH 2.2, respectively. This result points to the fact that, although the degree of ionization of the whole film is solely controlled by pH and independent of PE MW, the higher MW PMAA chains in the multilayer films could retain the swelling and, at the same time, retard the disintegration kinetics much longer because there are more electrostatic binding units per chain when compared with low MW counterparts.

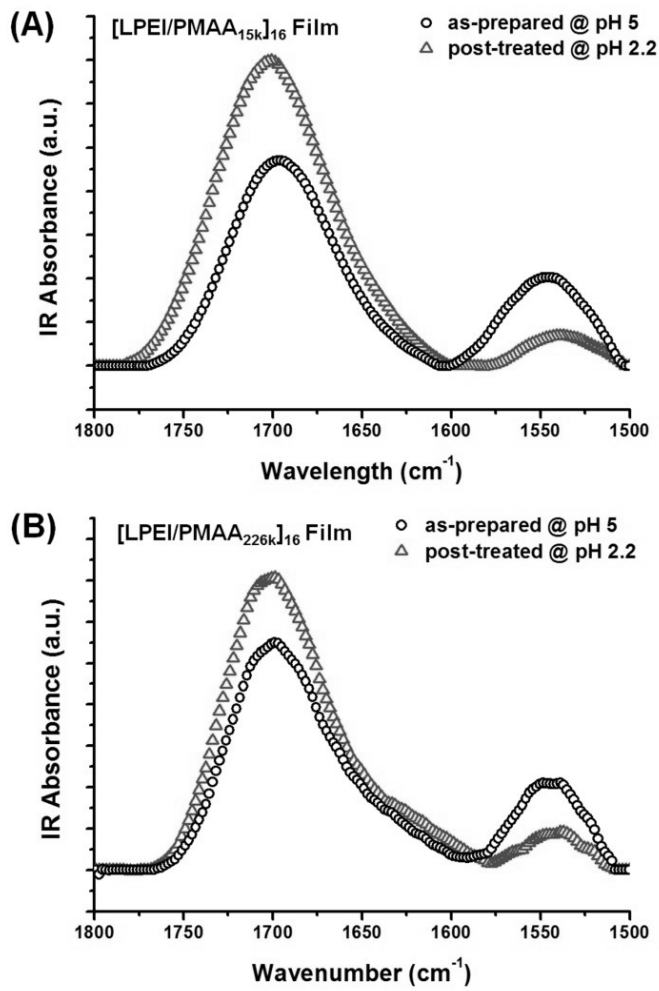

Figure 3.6. FT-IR spectra of PMAA chains of different molecular weights ((A) 15k and (B) 226k) incorporated within $[LPEI/PMAA_{MW}]_{16}$ multilayer films before (black open circle) and after (red open triangle) post-treatment, in the regions at 1701 and 1554 cm^{-1}, associated with COOH and COO^- groups, respectively.

Based on the combined analyses of NR, QCM-D, and FT-IR measurements, the disintegration behavior associated with the structural changes of weak PEs within multilayer films with different MWs is schematically summarized in **Scheme 3.1.** When the multilayer films are immersed into low pH water causing the deionization of PMAA chains along with excess positive charges of LPEI chains, the films tend to disintegrate into bulk solution in the entropy-driven manner. At the same time, the excess charges in LPEI layers could also cause the swelling of films due to charge repulsions, making both protonated PMAA and counter LPEI chains freely diffuse out into bulk solution from the top surfaces of multilayered films. In this disintegration process, the PMAA MW, which determines the number of binding units per chain, plays a major role in controlling the film disintegration kinetics. Furthermore, we also demonstrated that the rate determining step in the disintegration of weak PE multilayer films is the swelling process, which is again totally dependent on the MW of incorporated PE chains.

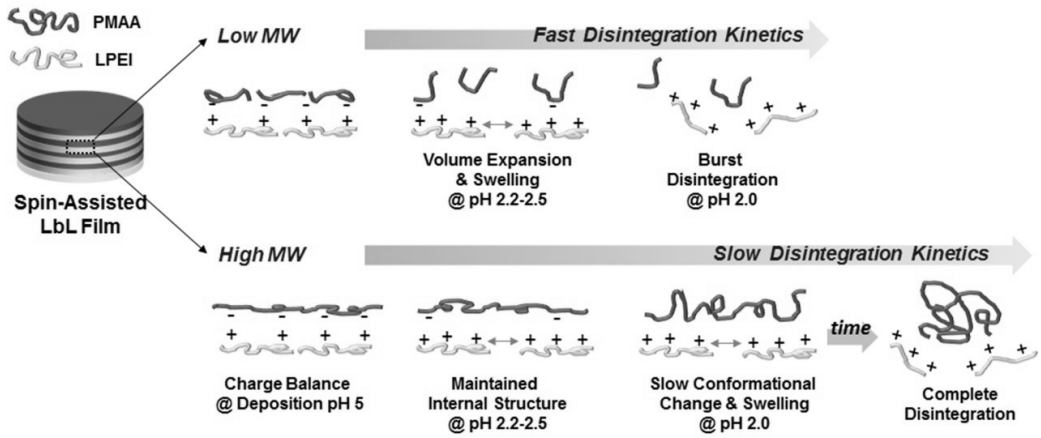

Scheme 3.1. A schematic on the disintegration process of spin-assisted weak PE multilayer films containing different MW PE chains.

3.4. Conclusion

The MW-dependent swelling and disintegration behavior of model weak PE multilayer films, $[LPEI_{25k}/PMAA_{MWs}]_{16}$ (MWs = 15k, 32.4k, 100k, and 226k), has been monitored by NR and QCM-D, yielding information on the nano-scale changes in internal structure and physical properties triggered by pH. The model films were prepared by the spin-assisted LbL deposition, which provides similar adsorption behavior of polymer chains regardless of PE MW and also offers flattened and smooth interfaces to enable precise monitoring of internal structural changes by NR. The multilayer films containing high MW PMAA chains show the surface erosion while low MW PMAA multilayer films demonstrate the burst erosion when they are triggered by low pH, causing massive dissociation between oppositely charged layers. By the QCM-D measurements at different pH combined with FT-IR analysis, we demonstrated that the pH-triggered swelling and disintegration kinetics of the spin-assisted weak PE multilayer films are totally controlled by the MW of PE chains incorporated into multilayered films. The MW-dependent disintegration kinetics originates from different numbers of binding sites per chain along with associated free energy penalty in conformational changes. This fundamental chain- as well as thin film structural-level understanding of the MW dependence on the disintegration kinetics of multilayer films could give insights into ways of developing functional controlled release platforms based on the LbL deposition without additional treatments or the insertion of other diffusion barrier molecules.

3.5. References

(1) G. Decher, *Science* **1997***, 277* (5330), 1232-1237.

(2) D. Yoo, S. S. Shiratori, M. F. Rubner, *Macromolecules* **1998***, 31* (13), 4309-4318.

(3) S. T. Dubas, J. B. Schlenoff, *Macromolecules* **1999***, 32* (24), 8153-8160.

(4) J. Seo, P. Schattling, T. Lang, F. Jochum, K. Nilles, P. Theato, K. Char, *Langmuir* **2010***, 26* (3), 1830-1836.

(5) J. F. Quinn, A. P. R. Johnston, G. K. Such, A. N. Zelikin, F. Caruso, *Chem Soc Rev* **2007***, 36* (5), 707-718.

(6) E. Kharlampieva, V. Kozlovskaya, S. A. Sukhishvili, *Adv Mater* **2009***, 21* (30), 3053-3065.

(7) A. Quinn, G. K. Such, J. F. Quinn, F. Caruso, *Adv Funct Mater* **2008***, 18* (1), 17-26.

(8) C. Y. Jiang, V. V. Tsukruk, *Adv Mater* **2006***, 18* (7), 829-840.

(9) J. A. Jaber, J. B. Schlenoff, *Current Opinion in Colloid & Interface Science* **2006***, 11* (6), 324-329.

(10) S. A. Sukhishvili, *Curr Opin Colloid In* **2005***, 10* (1-2), 37-44).

(11) P. T. Hammond, *Adv Mater* **2004***, 16* (15), 1271-1293.

(12) T. Boudou, T. Crouzier, K. F. Ren, G. Blin, C. Picart, *Adv Mater* **2010***, 22* (4), 441-467.

(13) Z. Y. Tang, Y. Wang, P. Podsiadlo, N. A. Kotov, *Adv Mater* **2006***, 18* (24), 3203-3224.

(14) Y. Jang, S. Park, K. Char, *Korean J Chem Eng* **2011***, 28* (5), 1149-1160.

(15) B. S. Kim, H. Lee, Y. H. Min, Z. Poon, P. T. Hammond, *Chem Commun* **2009***,* 28, 4194-4196.

(16) I. Erel-Unal, S. A. Sukhishvili, *Macromolecules* **2008***, 41* (22), 8737-8744.

(17) A. Zhuk, S. Pavlukhina, S. A. Sukhishvili, *Langmuir* **2009***, 25* (24), 14025-14029.

(18) Z. C. Zhu, S. A. Sukhishvili, *ACS Nano* **2009***, 3* (11), 3595-3605.

(19) W. Lin, Y. Guan, Y. J. Zhang, J. Xu, X. X. Zhu, *Soft Matter* **2009***, 5* (4), 860-867.

(20) A. Fery, B. Scholer, T. Cassagneau, F. Caruso, *Langmuir* **2001***, 17* (13), 3779-3783.

(21) A. A. Antipov, G. B. Sukhorukov, H. Mohwald, *Langmuir* **2003***, 19* (6), 2444-2448.

(22) C. Picart, A. Schneider, O. Etienne, J. Mutterer, P. Schaaf, C. Egles, N. Jessel, J. C. Voegel, *Adv Funct Mater* **2005***, 15* (11), 1771-1780.

(23) J. Hong, N. J. Shah, A. C. Drake, P. C. DeMuth, J. B. Lee, J. Z. Chen, P. T. Hammond, *ACS Nano* **2012***, 6* (1), 81-88.

(24) Y. Jang, B. Akgun, H. Kim, S. Satija, K. Char, *Macromolecules* **2012***,* 45 (8), 3542-3549.

(25) B. Sun, C. M. Jewell, N. J. Fredin, D. M. Lynn, *Langmuir* **2007***, 23* (16), 8452-8459.

(26) P. Kujawa, P. Moraille, J. Sanchez, A. Badia, F. M. Winnik, *J Am Chem Soc* **2005,** *127* (25), 9224-9234.

(27) J. E. Wong, A. M. Diez-Pascual, W. Richtering, *Macromolecules* **2009,** *42* (4), 1229-1238.

(28) L. Y. Shen, P. Chaudouet, J. A. Ji, C. Picart, *Biomacromolecules* **2011,** *12* (4), 1322-1331.

(29) H. Y. Zhang, D. Wang, Z. Q. Wang, X. Zhang, *Eur Polym J* **2007,** *43* (7), 2784-2791.

(30) B. Sun, R. M. Flessner, E. M. Saurer, C. M. Jewell, N. J. Fredin, D. M. Lynn, *J Colloid Interf Sci* **2011,** *355* (2), 431-441.

(31) Z. L. Gui, B. Y. Du, J. W. Qian, Q. F. An, Q. A. Zhao, *J Colloid Interf Sci* **2011**, *353* (1), 98-106.

(32) E. Kharlampieva, J. F. Ankner, M. Rubinstein, S. A. Sukhishvili, *Phys Rev Lett* **2008,** *100* (12), 128303.

(33) M. Rodahl, F. Hook, C. Fredriksson, C. A. Keller, A. Krozer, P. Brzezinski, M. Voinova, B. Kasemo, *Faraday Discuss* **1997,** *107*, 229-246.

(34) E. F. Irwin, J. E. Ho, S. R. Kane, K. E. Healy, *Langmuir* **2005,** *21* (12), 5529-5536.

(35) A. R. Patel, C. W. Frank, *Langmuir* **2006,** *22* (18), 7587-7599.

(36) Commercial materials, instruments and equipment are identified in this paper in order to specify the experimental procedure as completely as possible. In no cases does such identification imply a recommendation or endorsement by the National Institute of Standards and Technology nor does it imply that the materials, instruments, or equipment identified are necessarily best available for the purpose.

(37) D. Johannsmann, *Phys Chem Chem Phys* **2008,** *10* (31), 4516-4534.

(38) F. Hook, B. Kasemo, T. Nylander, C. Fant, K. Sott, H. Elwing, *Anal Chem* **2001,** *73* (24), 5796-5804.

(39) J. Cho, K. Char, J. D. Hong, K. B. Lee, *Adv Mater* **2001,** *13* (14), 1076-1078.

(40) E. Kharlampieva, V. Kozlovskaya, J. Chan, J. F. Ankner, V. V. Tsukruk, *Langmuir* **2009,** *25* (24), 14017-14024.

(41) L. Ruiz-Perez, A. Pryke, M. Sommer, G. Battaglia, I. Soutar, L. Swanson, M. Geoghegan, *Macromolecules* **2008,** *41* (6), 2203-2211.

(42) P. J. Yoo, N. S. Zacharia, J. Doh, K. T. Nam, A. M. Belcher, P. T. Hammond, *ACS Nano* **2008,** *2* (3), 561-571.

(43) A. J. Parnell, S. J. Martin, C. C. Dang, M. Geoghegan, R. A. L. Jones, C. J. Crook, J. R. Howse, A. J. Ryan, *Polymer* **2009,** *50* (4), 1005-1014.

(44) S. S. Shiratori, M. F. Rubner, *Macromolecules* **2000,** *33* (11), 4213-4219.

(45) M. Sedlak, C. Konak, P. Stepanek, J. Jakes, *Polymer* **1987,** *28* (6), 873-880.

(46) H. W. Jomaa, J. B. Schlenoff, *Macromolecules* **2005,** *38* (20), 8473-8480.

(47) H. S. Lee, D. M. Eckmann, D. Lee, N. J. Hickok, R. J. Composto, *Langmuir* **2011,** *27* (20), 12458-12465.

(48) X. Turon, O. J. Rojas, R. S. Deinhammer, *Langmuir* **2008,** *24* (8), 3880-3887.

(49) A. F. Xie, S. Granick, *Macromolecules* **2002,** *35* (5), 1805-1813.

Chapter 4.[*]

Surface Functionalization of Polymer Multilayer Thin Films for *in vitro* Studies of Metastatic Cancer Cells

4.1. Introduction

The preparation and tuning of functional polymer thin films at the molecular level have caught significant attention of many researchers in the field of nanobio-medicine due to numerous potential applications. Ranging from biocompatible implant coatings to tissue engineering scaffolds, considerable efforts have been devoted to design polymeric thin films with new biological functionalities. In other words, the design of thin films with precise control of their structures and properties for targeted biomedical applications has become important and critical issues as researchers started to appreciate the influence of surface or film properties on cellular functions such as adhesion, proliferation, motility, differentiation and so forth.

Among many fabrication techniques available to realize functional polymer thin films for biomedical applications, the layer-by-layer (LbL) assembly has been considered to be the one of the most efficient and practical methods owing to its simplicity in fabrication steps as well as versatility in the choice of both depositing materials and substrates. Moreover, the LbL deposition technique is ideally suited to biomedical applications because the LbL assembly

[*] This chapter is based in part on two papers from Yeongseon Jang, Saibom Park, and Kookheon Char, *Korean Journal of Chemical Engineering* **2011**, 28, 1149-1160 and from Hyojin Lee[†], Yeongseon Jang[†], Jinhwa Seo, Jwa-Min Nam, and Kookheon Char, *ACS Nano* **2011**, 5, 5444-5456. Copyright 2011 Springer and American Chemical Society

could be typically performed in aqueous solution. Consequently, the LbL deposition has been utilized to modify or functionalize the multilayer films for biomedical purpose by the precise control of thin film properties (i.e., modulus, charge density, release characteristics) as well as the incorporation of drugs or active ingredients at a desired position within the multilayer films.[1] In particular, surface topography of the thin films for cell-culture is known to be one of important parameters to influence the adhesion and spreading behavior of cells. As a result, many cell lines have been tested to assess the effect of topologically structured surfaces, which are modified with inorganic nanoparticles, nanotubes, or patterning, due to recent advances in micro- or nano-fabrication techniques allowing us to investigate the cells' behavior in nanostructured environment of interest.[2,3] Such various functionality and unique dimension and size of nanomaterials can enhance the bio-functionality to control the cellular behavior *in vitro* or *in vivo* by combining with the advantages of LbL assembly.

Herein, we designed nano-bio-functionalized LbL polymer platforms to study and control the adhesion of metastatic cancer cells and their behavior changes (i.e., focal adhesion, spreading, surface projections, etc). Metastasis is typically initiated by the detachment of cancer cells from a primary tumor site and subsequent adaptation of cancer cells to a distant new environment. The roles of molecules such as integrin, laminin-binding protein, and cadherins in tumor growth, invasion, and metastasis are under active investigation. Although many cell lines have been studied to assess the effect of nanoenvironments,[4,5] metastatic cancer cells have not been studied in detail within their nanoenvironment. Metastatic cells are different from other non-metastatic cells or normal cells in that they have different adhesion and detachment mechanisms and cell-cell signalings play major roles for these behaviors. In this regard, understanding and controlling the adhesion of metastatic cancer cells is of paramount importance to cancer research, diagnosis, and treatment.

In the present study, biomolecule-functionalized nanofeatures were realized by immobilizing biomolecule-modified gold nanoparticles (AuNPs) on a LbL polymer substrate. To this end, fibronectin (Fn) and ephrin were used in our study. Fibronectin is a cell adhesive molecule that can specifically bind to the integrins of a cell surface. Accordingly, Fn-conjugated AuNPs could serve as nanofeatured extracellular matrix (ECM) adhesion sites. On the contrary, it has been known that ephrin signaling can disrupt the cell adhesion[6] and guide the cell metastasis, and elevated ephrinB3 expression was reported in invasive glioma cells.[7-9] Ephrin ligands (ephrinB3 in this study) are presented to metastatic cells via cell-cell interactions, and it is known that cell curvature and molecular clustering are often important factors for effective cell-cell signaling. Finally, a positively charged polymer surface constructed by the spin-assisted LbL deposition method, which provides a well-ordered thin film that has uniform surface charge and morphology so then can immobilize negatively charged biomolecules (i.e., Fn and ephrinB3) and AuNPs on it. This LbL film underneath nanoparticles offers a handle in controlling the mechanical and chemical property of a cell culturing and signaling substrate. Using this versatile nano-bio functionalized LbL platform, we assembled both cell-ECM and cell-cell interaction systems on a polymer substrate and investigated the effect of nanoscale features as well as biological recognition on the cellular phenotypic changes in adhesion, cytoskeletal organization-based morphology and motility of human breast metastatic cancer cells (CAMA-1). We hope that this study, based on the engineering and bio-functionalization of polymeric multilayer thin films, could ultimately contribute to open up new possibilities to design flexible and multifunctional polymer platforms for many biomedical applications.

4.2. Experimental Section

Materials. Poly(allylamine hydrochloride) (PAH, M_w = 70,000 g/mol) and polyacrylic acid (PAA, M_w = 100,000 g/mol) were purchased from Aldrich. Fibronectin from human plasma (Fn, M_w = 450,000 g/mol) and ephrinB3 (M_w = 49,200 g/mol) were purchased from Sigma and used as received. Cryo-preserved human breast cell line and media were purchased from American Type Culture Collection (Manassas, VA, USA).

Preparation and Characterization of Layer-by-Layer (LbL) Polymer Films. 0.01 M PAA and PAH polymer solutions were prepared by dissolving the polymers in 18 MΩ Mili-Q water, and HCl and NaOH were used for the pH adjustment at pH 7.5 for PAH and at pH 3.5 for PAA. Fn and ephrinB3 were also dissolved in water (0.67 mg/ml) prior to use. Cover glass was used as a substrate to build the LbL film. All the substrates were cleaned by RCA treatments[68] before LbL deposition. $(PAH/PAA)_5/PAH$ LbL polymer films were prepared using an automatic spin coater (Headway Research Inc.). Detail experimental descriptions for LbL deposition process are well documented in our previous report[10]. For the modification of an LbL film with nanoparticles, gold nanoparticles (AuNPs) and protein-modified AuNPs (Fn-AuNP and ephrinB3-AuNP, respectively) in water were added to the PAH top-coated LbL film and spun at 3,000 rpm for 20 s until a sufficiently dried film was obtained. The coated AuNP density was controlled by varying the spin-coating time and concentration of gold particle solution (4.5×10^{10}/ml). The film surface morphology and RMS roughness were measured by an AFM microscope (Nanoscope IIIa, Digital Instruments). Water contact angles were measured using a DE/DSA100 (Früss Inc.) contact angle analyzer.

Preparation of AuNP Probes. First, the pH of AuNP solution (Ted Pella, USA, 15708-55) was increased to pH 9 by NaOH solution for obtaining sufficient interaction between AuNPs and proteins. Then, Fn or ephrinb3 proteins were added to 1 ml gold nanoparticle solution

(conc. 0.7 mg/ml). The amount of protein was determined by salt test to see whether Au nanoparticles are aggregated or dispersed when the final salt concentration of solution reaches 0.2 M. After 1 hour incubation, AuNPs were precipitated by centrifugation at 8,000 rpm, 4 ^{o}C. The supernatant was removed, and then AuNPs were dispersed in distilled water.

Zeta-Potential and DLS Measurements. The surface zeta-potential and hydrodynamic diameters of the AuNPs were measured by Dynamic Light Scattering Spectrophotometer (Ohtsuka Electronics, Japan, DLS-7000). Three kinds of AuNPs (citrate-stabilized AuNP, fibronectin-modified AuNP, and ephrinB3-modified AuNP) were centrifuged and re-dispersed in pure water, respectively. Zeta potential and hydrodynamic diameter values were evaluated three times for each case.

Cell Culture. The CAMA-1 cells (ATCC Num. HTB-21) were purchased from ATCC. CAMA-1 cells (cell conc. 1 x 10^4 cells) were grown in DMEM (ATCC) with 10% fetal bovine serum and 100 units/ml penicillin-streptomycin (Gibco, USA, 15070063) at 37 ^{o}C, 5 % CO_2. For more exclusive observation of substrate effect, CAMA-1 cells were cultured in DMEM media without FBS for 2 days or 7days at 37 ^{o}C, 5 % CO_2.

Analysis of Cell Aspect Ratio. The CAMA-1 cells were cultured for 2 days. And then, we took the optical images of cells using optical microscopy. (10X; Carl Zeiss, Germany, Axiovert 200M) We calculated the aspect ratio of 60 cells present in optical images of each sample. To calculate the aspect ratio, two different line lengths of the cells were measured; the longest line length and the shorter line length. The longest line length is the literally the longest line length of the cell body and the shorter line length is the line length that divides the longest line length in half at 90 degrees. Dividing the longest line length by the shorter one gives the aspect ratio.

Actin Staining. Cell culture medium was harvested, and cells were washed twice with PBS solution. Cells were then fixed by 4 % paraformaldehyde/PBS for 15 min. Cells were washed

with PBS solution three times (5 min for each time). To block nonspecific binding, we used 1 % BSA/PBS/0.3 % tween20 for 15 min, and the cells were washed with PBS solution afterwards. Phalloidin-Tetramethyl rhodamine isothiocyanate (TRITC) (Sigma-Aldrich, USA, P-1951) was diluted to 5 % with PBS solution. The Phalloidin-TRITC solution was added to each well, and the cells were incubated at 37 ^{o}C for 40 min. Next, cells were washed with PBS solution two times after incubation. Finally, the stained cell samples were examined under a confocal laser scanning microscopy (Leica, Germany, TCS SP5).

Sandwich-ELISA. The amount of focal adhesion-associated protein, paxillin, in cell extracts was evaluated with the sandwich ELISA method. CAMA-1 cells were grown in DMEM with 10% fetal bovine serum and 100 units/ml penicillin-streptomycin (Gibco, USA, 15070063) for 2 days. Cells were disrupted by RIPA buffer (Pierce, USA, 89900) at 4 ^{o}C. Lysates were clarified at 14,000 rpm in an eppendorf tube for 10 min at 4 ^{o}C. The supernatant was transferred to a new tube, and the pellet was discarded. We performed the Bradford assay (Bio-Rad, USA, 500-0006) to determine the protein concentration. For the sandwich assay, samples were loaded on 96 wells. We used rabbit anti-human paxillin polyclonal antibody (abcam, United Kingdom, ab2264) and mouse anti-human paxillin monoclonal antibody (abcam, United Kingdom, ab3127) to form sandwich complexes. At the final step, secondary anti-rabbit IgG were conjugated to horseradish peroxidase, and the absorbance at 450 nm was measured.

Paxillin and Phospho-Paxillin Staining. After cell culturing for 2 days, cells were fixed in 3.7% paraformaldehyde in PBS solution at pH 7.4 for 20 min at room temperature. Then, the samples were washed twice with cold PBS solution. The samples were incubated with PBS solution containing 0.25% Triton X-100 for 10 min. Next, cells were washed with PBS solution three times for 5 min each. Theses samples were treated with 1% BSA in PBST for 30 min to block nonspecific binding of the antibodies. Cells were then incubated in the anti

paxillin antibody (abcam, United Kingdom, ab3127) or anti-phospho-paxillin antiboby (Ser126) (Millipore, USA, 07-733SP) solution with blocking buffer for overnight at 4℃. On the following day, cells were washed three times with PBS solution for 5 min each. For paxillin staining, cells were incubated with rhodamine conjugated-secondary antibody (abcam, United Kigndom) in 1% BSA for 1 hour at room temperature without exposing to light. In anti-phopho-paxillin staining case, cells were incubated with FITC conjugated-secondary antibody (Millipore, USA). We decanted the secondary antibody solution and washed three times with PBS solution for 5 min each in the dark. Finally, we mounted a drop of mounting medium (abcam, United Kingdom, ab64230) on a coverslip. Paxiilin was observed by a Total Internal Reflection Fluorescence Microscope (60X; Nikon, Japan, TE2000-E) with the same exposure time. And we took phospho-paxillin images using florescence microscopy. (40X; Carl Zeiss, Germany, Axiovert 200M)

Western Blot. We performed the western blotting to compare the protein amount of cells for each substrate. First, CAMA-1 cells were cultured in the DMEM with 10 % FBS on LbL, Fn/LbL, ephrinB3/LbL, AuNPs/LbL, Fn-AuNPs/LbL and ephrinB3-AuNPs/LbL substrates, respectively at 37 ^{o}C, 5 % CO_2 for 2 days. Then, the cells were collected and transferred to microcentrifuge tubes. To remove cell culture medium, the tubes were centrifuged at 1500 rpm for 3 min. For cell lysis, we added RIPAbuffer (Pierce, USA, 89900) to each tube, and total protein solution was obtained. We diluted an aliquot of the cell lysate sample for the Bradford (Bio-Rad, USA, 500-0006) protein concentration assay. Next, we added an equal volume of 2X sample buffer (125 mM Tris pH 6.8, 4 % SDS, 10 % glycerol, 0.006 % bromophenol blue, and 1.8 % ß-mercaptoethanol) to all samples, and the resulting solution was boiled for 3-5 minutes. 10 μg of total proteins of cells was added to each well of a 10% SDS 0.75-mm thick gel (Hoefer, Germany). The proteins were transferred from gel to PVDF

membrane at 1 Amp constant current for 1 hour or equivalent in transfer buffer (Hoefer, Germany). The blot from the transfer apparatus was removed and immediately placed into blocking buffer (5% non-fat dry milk, 10 mM Tris pH 7.5, 100 mM NaCl, and 0.1% Tween 20). The membrane was incubated in blocking buffer for 1 hour at room temperature. We diluted the antibody according to antibody data sheet in the corresponding blocking buffer [β-actin antibody (rabbit, Santa Cruz, USA) 1:5000 p-paxillin antibody (rabbit, Millipore, USA) 1:500]. After decanting the blocking buffer from the blot, we added the antibody solution, and the resulting solution was incubated with agitation for overnight at 4°C. After decanting the primary antibody solution, the membrane was washed with wash buffer (10 mM Tris pH 7.5, 100 mM NaCl, and 0.1% Tween 20) for 30 min with agitation, changing the wash buffer every 3-5 min. We added diluted-enzyme conjugate anti-rabbit IgG-HRP (1:5000 in wash buffer containing 5% non-fat dry milk), and the resulting solution was incubated with agitation for 1 hour at room temperature. We decanted the secondary antibody solution, added wash buffer (10 mM Tris pH 7.5, 100 mM NaCl, 0.1% Tween 20), and the membrane was washed for 1.5 hr with agitation, changing the wash buffer every 20 min. Finally, we added ECL mix (GE healthcare**,** United Kingdom**)** to the membrane, and the signal of the membrane was immediately exposed to film for 1 min.

Non-Specific Binding Test. We confirmed non-specific interaction between fibronectin and polymer substrates. The samples were incubated in DMEM with 10% NCS (Newborn Calf Serum, Gibco, USA) for 48hr. And then, these substrates were washed twice with PBS for 3min each and incubated with anti fibronectin antibody (Millipore, USA) solution for overnight at 4 ºC. We used rhodamine conjugated-secondary antibody (abcam, United Kingdom) to detect fibronectin. The images were observed by florescence microscopy. (Carl Zeiss , Germany, Axiovert 200M)

4.3. Results and Discussion

4.3.1. Introduction of Nano-Roughness on Polymer Multilayer Thin Films for Controlling Adhesion of Cells

The polymer films were prepared based on the layer-by-layer (LbL) deposition method[11] to build nanostructures in a straightforward fashion. Poly(allylamine hydrochloride) (PAH) and poly(acrylic acid) (PAA) were employed as the basic building block materials for LbL film matrices, and PAH layer is the top layer that presents positive charges in order to facilitate surface modification with negatively charged functional materials. The [PAH/PAA] multilayer thin films has been extensively studied due to their distinctive physical properties such as film thickness and surface morphology according to the film deposition pH conditions.[13-14] In addition, The [PAH/PAA] multilayer film are used as a cell culture platform due to the non-cytotoxic properties.[15]

In order to apply the [PAH/PAA] films to cell culture platforms, we investigated the thickness growth behavior, interface/surface roughness and morphology of [PAH/PAA] multilayer films in Chapter 1 and our previous work[10]. Since the characteristics of the films in physiological environments are also significantly important, the surface morphological changes and swelling properties of the [PAH/PAA] films prepared by either dip- or spin-assisted LbL methods with different pH combinations (6.5/6.5 and 7.5/3.5) were investigated by liquid atomic force microscope (AFM). As a result, the $[PAH/PAA]_{5.5}$ multilayer films are prepared by the spin-assisted LbL deposition for the culture of human breast metastatic cancer cell, CAMA-1, because they could provide uniform surface charges, morphology and film stability in liquid when compared with the conventional dip-assisted method. These polymer films can serve as the hydrated polymer cushions to hinder the artificial solid glass

substrate effect and allow for adjustable cellular interactions with various engineered functionalities.[12]

To introduce the nano-roughness to the LbL films, we modified the positively charged film surfaces with negatively charged pristine AuNPs via electrostatic interactions. A series of substrates with different NP densities on the LbL films were prepared to investigate the changes in metastatic cell adhesion in response to the changes in nanoparticle density as well as surface roughness. For the nanotopographical modification of LbL films, AuNPs in water (80 μl) were added to the PAH top-layered LbL film and spun at 3,000 rpm for 20 s until a sufficiently dried film was obtained (an AuNP stock solution was prepared in DI water at a concentration of $4.5x10^{10}$/ml). In order to vary the density of AuNPs on the LbL film, we varied the repetition number of spin coating using the AuNP stock solution and diluted the AuNP stock solution with DI water. The AuNP densities of all the samples used in cell culture were measured with the AFM images in >3 different regions, as shown in Figure 4.1.

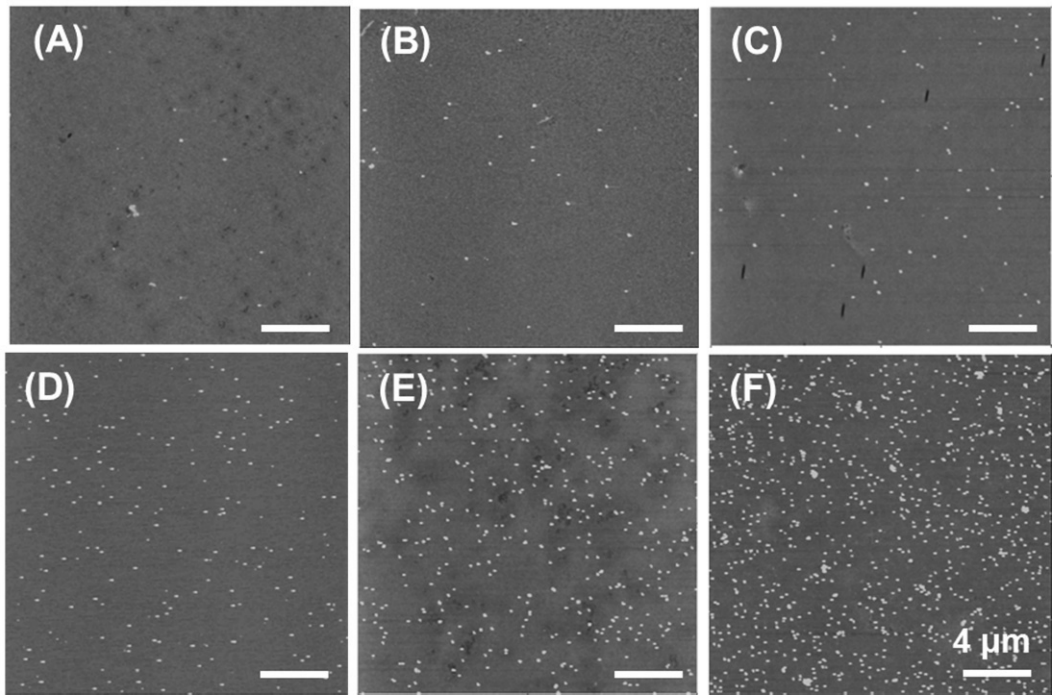

Figure 4.1. AFM images of AuNPs/LbL surfaces with different AuNP densities. (Number of AuNPs/400 μm^2 (RMS roughness): (A) 12 ± 1 (1.3 nm), (B) 31 ± 2 (1.6 nm), (C) 85 ± 12 (2.0 nm), (D) 142 ± 10 (2.4 nm), (E) 391 ± 44 (4.8 nm), (F) 808 ± 3 (6.7 nm))

4.3.2. The Effect of Nano-Topography of Polymer Multilayer Thin Films on the Focal Adhesion of Metastatic Cancer Cells

The AuNP density on the surface was correlated with cell adhesion. As the AuNP density on the LbL film surface was increased, the surface roughness increased accordingly. The RMS roughness value increases from 1.3 nm for 12 AuNPs/400 μm^2 up to 6.7 nm when more than 808 AuNPs/400 μm^2 were attached on the LbL film. Also, the distance between AuNPs would have a critical role in the regulation of focal adhesion of cells.

CAMA-1 cells (1 x 10^4 cells) were cultured on the AuNP/LbL substrates (81 mm^2) at different Au densities for 48 hr. Cell morphology and paxillin distribution in cells were observed by an optical microscope after 48 hr cell culture (Carl Zeiss Axiovert 200M) (Figure 4.2A). Interestingly, cell shape was dramatically changed to have the most polarized morphology for the 142 AuNP density condition. However, cells maintained rather spherical morphologies on the substrates with lower or higher AuNP densities than 142 AuNPs/400 μm^2. Paxillin sandwich ELISA experiments were performed to analyze and quantify the cellular focal adhesion on a respective matrix. Paxillin is a focal adhesion-associated, phosphotyrosine-containing protein that plays roles in several signaling pathways such as the focal adhesion kinase (FAK)-Src signaling, controlling cell adhesion and cell migration process.[16] As a result, the amount of paxillin increases as the particle density is increased (Figure 4.2B). However, when the AuNPs were too densely coated on polymer surface (>391 particles/400 μm^2), the amount of paxillin started to decrease. This result suggests that there exists a certain range in surface roughness for metastatic cancer cells to effectively adhere to the surface, and the cell adhesion could even be aggravated when too many nanoparticles are introduced to the cell adhesion surface. Cells usually respond differently to substrates under various conditions including varying geometry and topography.[17-19] The protein clustering in

focal adhesion of a cell, which is in the range 5-200 nm,[18] could be influenced by nanometer scale features on the cell culture matrices. In particular, the clustering of integrins has shown to play a critical role in the cell adhesion process including focal adhesion.

In our case, as the particle density on the polymer surface is decreased, the spacing between AuNPs becomes larger and it is likely that the clustering of integrins is limited by the sparsely dispersed binding sites.[20] This is why particle density needs to be high for cells to bind to the surface. On the other hand, when the density of AuNPs on a polymer surface is too high and AuNPs are placed very close to each other, cells need to make effort to reach the bottom of substratum through the closely-spaced particles and have many convexities of the cell membrane, each with a very small curvature radius.[21] These could cause a stressful condition in cell adhesion and proliferation and cells try to minimize the contact area with the substrate to reduce the stress.[22] These factors could induce the negative effect on cell focal adhesion, and, consequently, the decreased paxillin amount could be observed for metastatic cancer cells on a substrate with a very high AuNP density. Our results suggest that the optimal AuNP density for the metastatic cell adhesion is ~140 particles per 400 μm^2 of the surface area. The average distance between AuNPs at optimal density is nearly 2 μm in this case, which very large compared to the previous studies with other cells such as osteoblast cells.

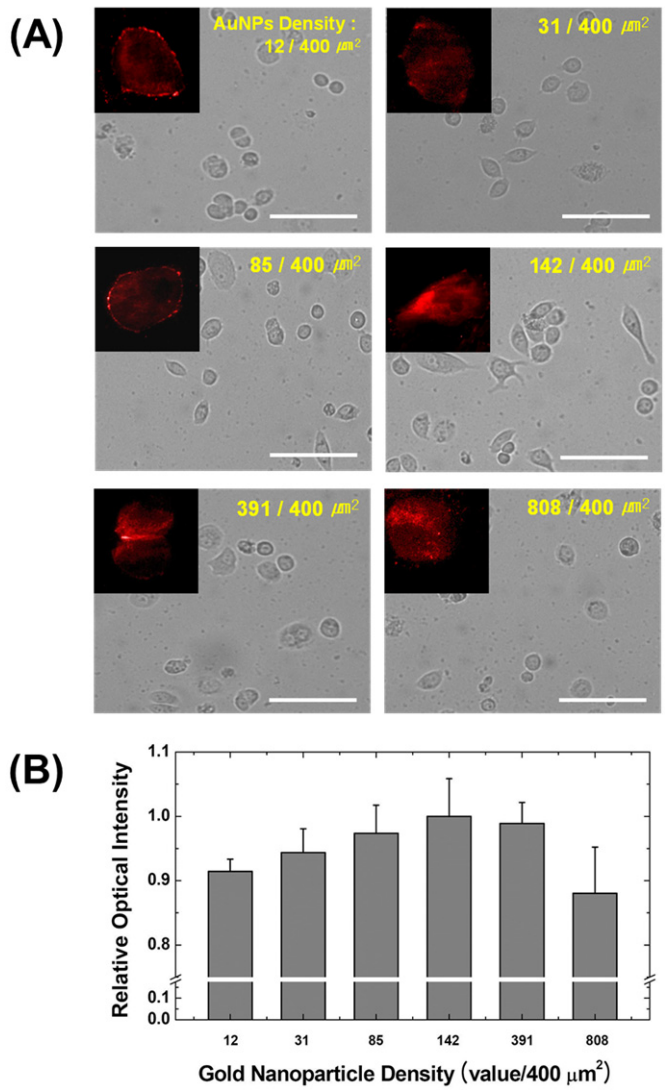

Figure 4.2. Optical images of CAMA-1 cells cultured on LbL substrates with different AuNP densities. Inset images are the total internal reflection fluorescence (TIRF) images of paxilin. The scale bars in all images are 100 μm.

4.3.3. Control on the Surface Nano-Topography and Biochemical Properties of Polymer Multilayer Thin Films

To investigate the metastatic cancer cell adhesion and morphology on the biologically functional nanoparticle surface, CAMA-1 cells are cultured on the citrate-, Fibronectin (Fn)-, and ephrinB3-conjugated AuNP/LbL surfaces with NP densities of 141/400 μm^2 for 2 days or 7 days, respectively. The same cells were also cultured on a bare glass and LbL film substrates with and without biomolecules (*i.e.*, LbL, Fn/LbL, and ephrinB3/LbL substrates) as control experiments (Scheme 4.1).

Fn, an ECM protein, is a cell adhesive molecule that can specifically bind to the integrin of a cell surface. Accordingly, Fn-conjugated AuNPs could serve as ECM adhesion sites. The role of Fn for cancer cell adhesion is different depending on the type of cell line and environment, and it is interesting to see how Fn works on metastatic CAMA-1 cells when these Fn molecules are coated on nanoparticle surfaces. On the contrary, it has been shown that ephrin-Eph receptor signaling decrease cell adhesion[23] and guide cancer metastasis.[24-26] This ephrin-Eph receptor communication sends signals to the receptor tyrosine kinase of Eph receptors, which affect the metastatic cellular activities including the expression of actin cytoskeleton, adhesion to surface, intercellular junctions, and morphological changes. Negatively charged Fn or ephrinB3 was tightly bound to the positively charged LbL film cushions placed on the glass substrates. The Fn or ephrinB3 is electrostatically conjugated to the surfaces of 50-nm-AuNPs. These biomolecule-conjugated AuNPs were then spread on the LbL films also based on the electrostatic interactions. AuNP-modified LbL surface, Fn or ephrinB3-AuNP-conjugated LbL surface and Fn or ephrinB3-coated LbL surface without AuNPs are denoted as AuNP/LbL, Fn-AuNP/LbL, ephrinB3-AuNP/LbL, Fn/LbL and ephrinB3/LbL surfaces, respectively. The surface morphology and hydrophilicity of the prepared the functionalized polymer matrices were characterized by AFM and water contact

angle measurements, as shown in Figure 4.3. The electrostatic interactions between AuNPs and the LbL polymer surface are necessary and strong enough to hold the particles on the surface when cells were interfaced with the particles in a cell culture medium. Using these versatile biomolecules and AuNP-functionalized LbL platforms, we assembled both cell-ECM and cell-cell interaction systems on polymer substrates and investigated the effect of nano-features as well as biological recognition on the cell behavioral changes in adhesion, cytoskeletal organization-based morphology and motility of human breast metastatic cancer cells (CAMA-1).

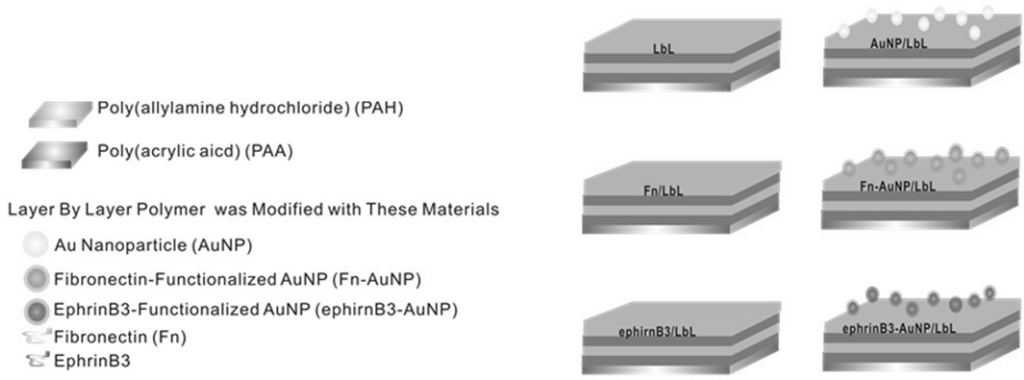

Scheme 4.1. A schematic representation of nanoparticle-functionalized polymer thin films investigated in this study.

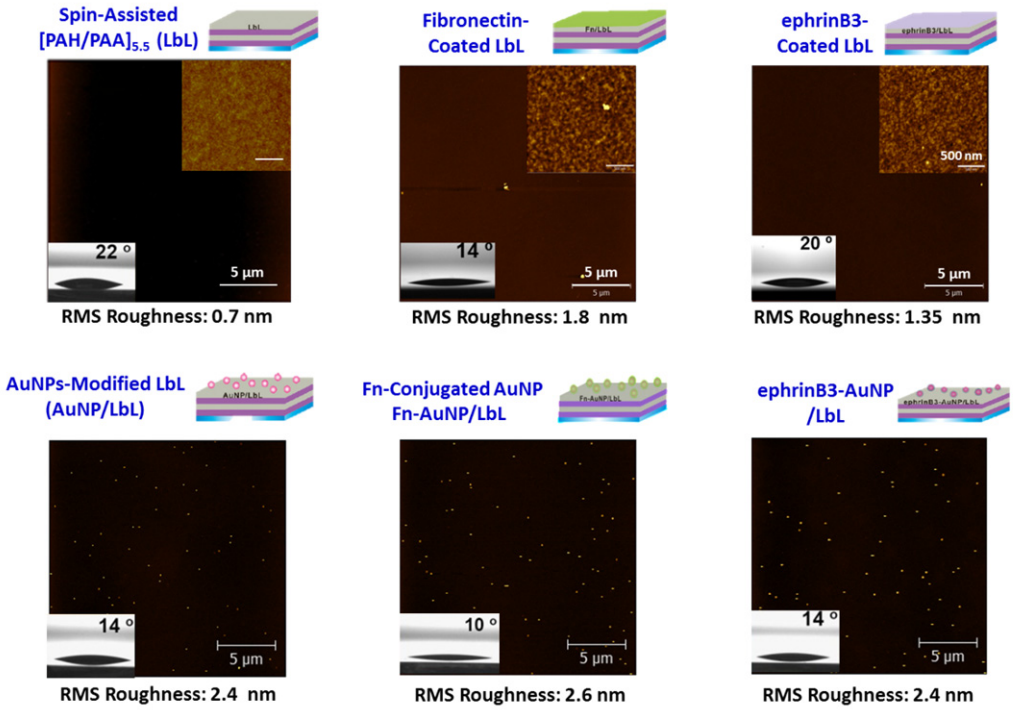

Figure 4.3. AFM height images of the LbL, AuNP/LbL, Fn-AuNP/LbL, and ephrinB3-AuNP/LbL substrates, respectively (scan area: 20 µm × 20 µm). The insets in all figures show water contact angles of each surface.

4.3.4. Synergetic Effect of Nano-Topography and ECM Proteins on the Interactions between Cell and Extracellular Matrix

The morphological changes of breast metastatic cancer cells after 2 days or 7 days of culture were observed and analyzed by an optical microscope and these optical images were used to calculate the aspect ratio of cells captured in the images of each sample for the quantitative analysis of cell morphological changes (Figure 4.4). To further demonstrate the effect of nanotopological surface on the cellular cytoskeletal organization and expression, the actin of CAMA-1 cells were stained with fluorescently-labeled phalloidin-TRITC and analyzed under a confocal microscope **(**Leica TCS SP5) (Figure 4.5). In the case of the PAH-top-layered LbL substrate without AuNPs (*i.e.*, LbL), CAMA-1 cells were attached to the positively charged LbL surface and showed elliptical morphology, which is in good agreement with our previous results.[10] However, cell surface projection features (*e.g.*, lamellipodia and filopodia) were not clearly observed, and this indicates that the cells on this surface may not be highly mobile. The cells that we examined here are from a metastatic cancer cell line that is often less sticky to the surface when compared with normal or non-metastatic cells.[27-28] In this regard, the metastatic CAMA-1 cells exhibit the spreading morphology even with fewer integrins on the cell surface on the positively charged LbL polymer surface while they do not show such morphology on the glass surface.

Remarkable cellular protrusions were observed from the spreading CAMA-1 cells on both AuNP/LbL and Fn-AuNP/LbL surfaces as shown in Figures 4.5 while no clear cell surface projections were observed for Fn/LbL, LbL and glass substrates. The cells on the AuNP/LbL and Fn-AuNP/LbL surfaces show significantly elongated anisotropic morphologies compared to those on the LbL substrate. CAMA-1 cells formed many large lamellipodia and filopodia that protrude out from the cell surface on the AuNP/LbL and Fn-

AuNP/LbL substrates. We note that cells also take high aspect ratios on the AuNP/LbL and Fn-AuNP/LbL substrates, as evidenced in Figure 4.4. Importantly, actin-staining results show that the strong actin bundle formation is involved with the cell spreading on the AuNP/LbL and Fn-AuNP/LbL substrates. Our previous results suggest that the CAMA-1 cells were not seriously affected by the existence of Fn proteins on a substrate for their proliferation and spreading.[43] Similarly, the change in cellular shape is almost identical for the AuNP/LbL and Fn-AuNP/LbL surfaces, indicating that the adhesion of metastatic cells is mainly governed by the AuNP-based nanofeatures on the surface.

It has been well-known that ephrin facilitates the signaling for the detachment of metastatic cells from the surface. The roles of ephrin in reverse signaling of cancer cells have been well documented to promote the cell transformation and cancer cell migration/invasion.[29-30] Two cases were examined in the present study: Ephrin molecules were directly applied on the LbL substrate (ephrinB3/LbL) and ephrinB3-conjugated AuNPs were modified to the LbL surface (ephrinB3-AuNP/LbL). For both cases, the metastatic cancer cells did not adhere to the surface effectively and they show the round-shaped morphology as shown in Figures 4.5. These results are comparable to the control substrates without nanoscale surface feature (*i.e.*, glass, Fn/LbL, and ephrinB3/LbL).

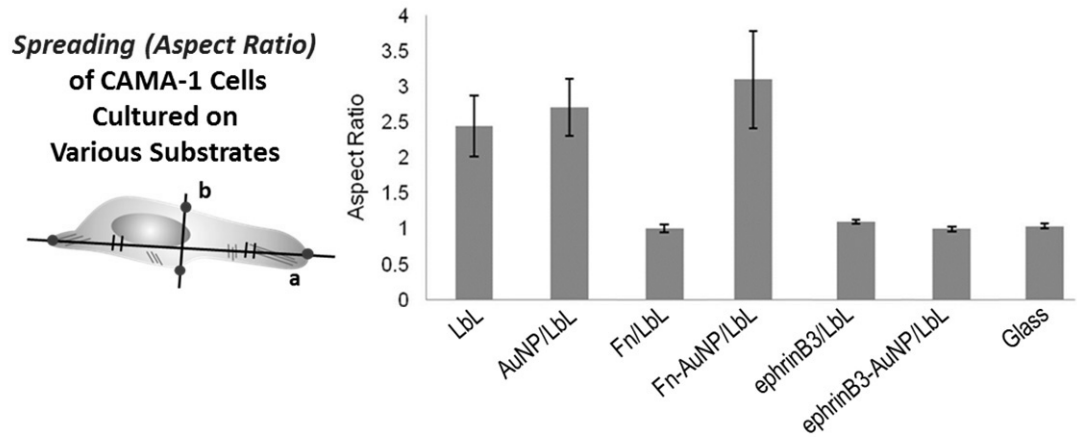

Figure 4.4. Aspect ratios of CAMA-1 cells after 2 days of culture on the glass, LbL, or Fn-, ephrinB3-coated LbL films and three different AuNPs (i.e., pristine AuNP, Fn-AuNP, ephrinB3-AuNP)-coated LbL films.

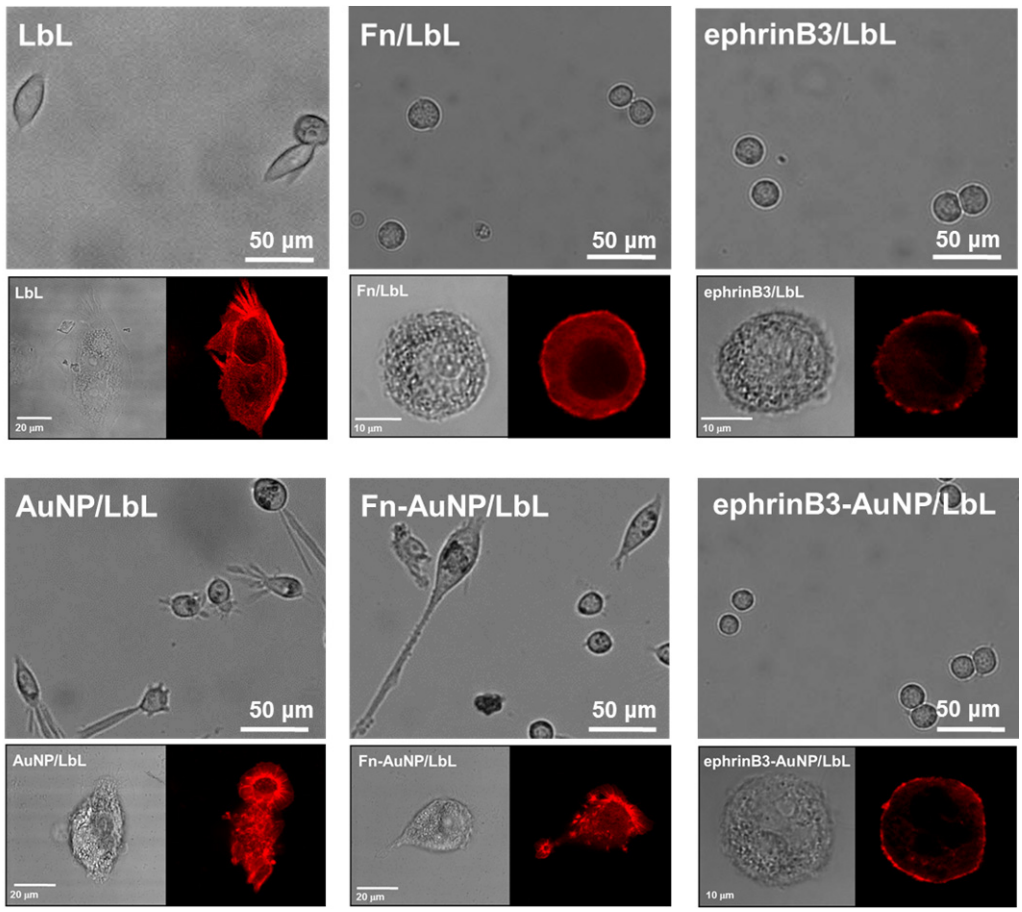

Figure 4.5. Optical images of CAMA-1 cells after 2 days of culture on on the glass, LbL, or Fn-, ephrinB3-coated LbL films and three different AuNPs (i.e., pristine AuNP, Fn-AuNP, ephrinB3-AuNP)-coated LbL films. Red fluorescence images were obtained at the actin-stained CAMA-1 cells.

Typically, cell adhesion is initiated by the ECM proteins. As mentioned earlier, focal adhesion kinase (FAK) can affect the cytoskeleton, membrane protrusions, and cell adhesion. In the cell adhesion process, FAK also mediates the phosphorylation on a specific serine residue of paxillin that binds to proteins that contribute to the organization of actin cytoskeletons, which, in turn, promote focal adhesion remodeling and cell motility.[31-32] Therefore, we performed paxillin sandwich ELISA (Figure 4.6A) and stained the cell with anti-paxillin antibody for observing fluorescent signal using a total internal reflection fluorescence (TIRF) microscope (Figure 4.6B) to indentify the correlation between focal adhesion and the amount change of paxillin in our system. In the paxillin quantitative experiment as shown in Figure 4.6, the highest values of paxillin amount were found from both AuNP/LbL and Fn-AuNP/LbL substrates. In TIRF images monitoring the interfaces between cells and a surface with high resolution and in great details, rigorous formation of paxillin clusters was found for the cells placed on AuNP/LbL and Fn-AuNP/LbL substrates while no distinct paxillin cluster formation was observed for the cells on other substrates. Paxillins were heavily clustered in the lamellipodium and filopodium regions and this demonstrates that nanoparticle-featured surfaces induce pronounced paxillin clustering as well as the intimate cell adhesion to the surface.

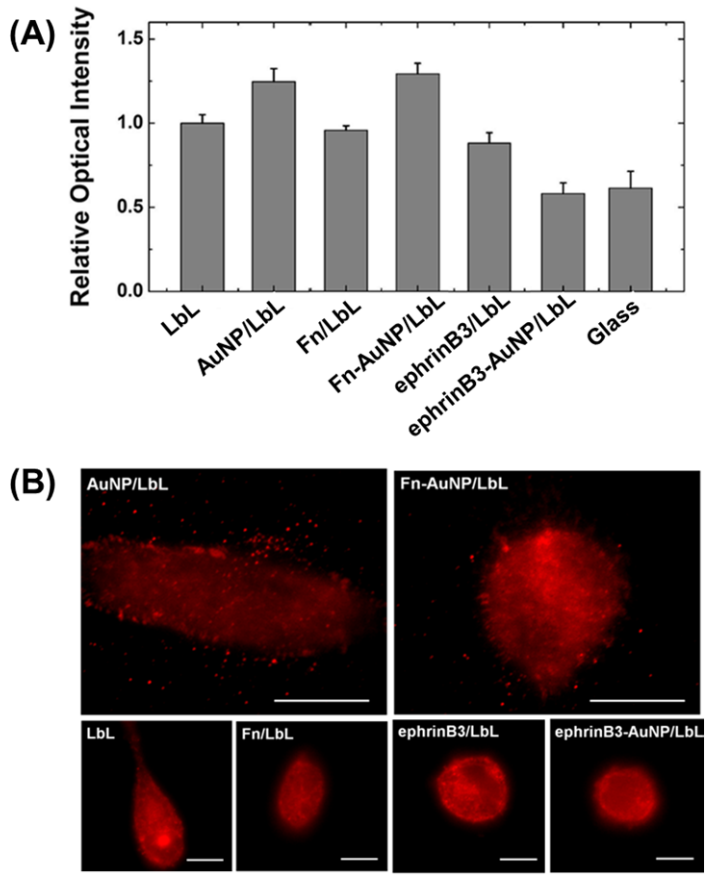

Figure 4.6. Paxilin analysis and imaging for CAMA-1 cells cultured on various types of functionalized LbL films. (A) Relative paxilin amounts in CAMA-1 cells obtained by ELISA analysis. (B) Total internal reflection fluorescence (TIRF) images of paxilins in CAMA-1 cells. The scale bars in all images are 20 μm.

Moreover, we took the fluorescence images of phospho-paxillin (p-paxillin) that is a paxillin-modified form in the focal adhesion cascade signaling of cells and detected the amount p-paxillin using the western-blot method (Figure 4.7). The p-paxillin bands were darker and thicker for the cells on AuNP/LbL and Fn-AuNP/LbL substrates when compared with other substrates. The results again agree well with the fluorescence image results for p-paxillin. In our data, AuNP/LbL and Fn-AuNP/LbL substrates induced the increased paxillin expression as well as phospohrylation of paxillins. In other words, AuNPs could activate the integrin function of metastatic cancer cells. The integrin activation stimulates the FAK signaling process, which could, in turn, result in more pronounced cellular focal adhesion. Next, we quantified the amount of integrin in CAMA-1 cells after 7 days of cell culture in order to confirm the integrin expression on the AuNP-functionalized LbL platforms through the sandwich-ELISA and immunofluorescence assay (data not shown). Since metastatic cancer cells usually express notably less number of integrins on their surfaces compared to normal or nonmetastatic cancer cells,[22] change in the amount of integrin between samples was too little to be detected using conventional methods. This result indicates that AuNP/LbL and Fn-AuNP/LbL substrates stimulate the focal adhesion associated-signal pathway while these substrates would not affect the integrin expression to a larger extent. Notice that the focal adhesion plays a key role in the regulation of proliferation, migration and metastasis of cancer cells.[33-35] The amount of paxillin, interacting with FAK, is closely correlated with cell proliferation[36] and it is believed that nanofeatured substrates are more suitable for the proliferation of metastatic cells than substrates without NPs. This result suggests that the nanoscale surface topography is much more important for the adhesion and proliferation of metastatic cells than the presence of cell adhesion proteins such as Fn only on the polymer substrate.

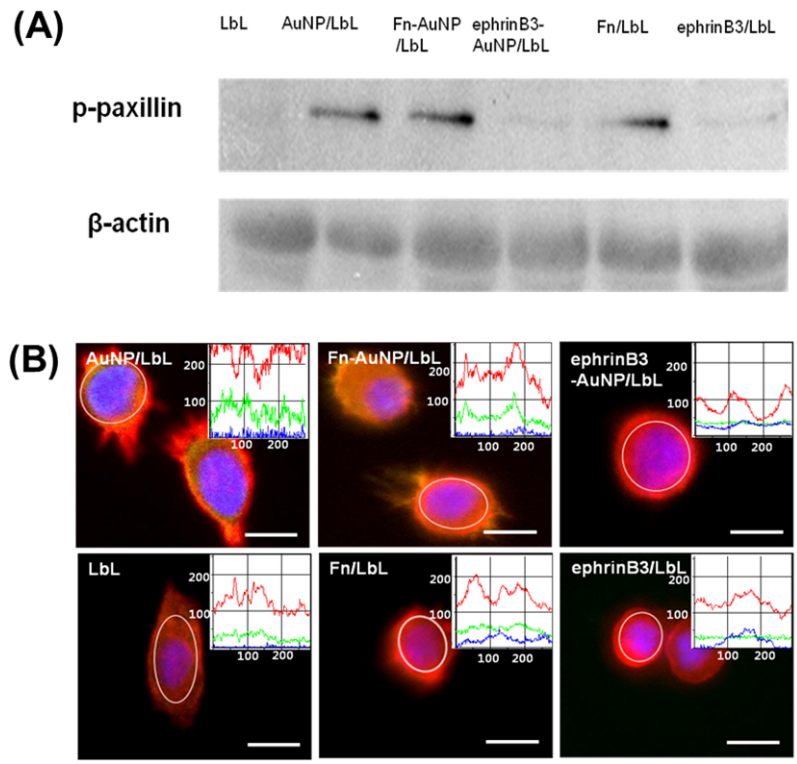

Figure 4.7. (A) Western blotting data for the detection of phosphor-paxilin in CAMA-1 cells after 2 days culture on various types of functionalized LbL films. β-actin was used as a control protein. (B) Fluorescence images and intensity profiles of actin (red), phospho-paxillin (green) and nucleus (blue) of the CAMA-1 cells after 2-day culture on various substrates. Fluorescence images are circle line profiling data (white circles in respective inset images). The fluorescence intensity of CAMA-1 cells was obtained by circle line profiling (Image Pro Plus). We analyzed fluorescence images that had the same exposure time in the same distance intensity. (X axis: Distance (Pixel), Y axis: fluorescence intensity) The highest value of red (actin) and green (phospho-paxillin) signal was observed from AuNP/LbL and Fn-AuNP/LbL. The scale bars in all the images are 20 μm.

Importantly, the amount of paxillin was distinctively lower on the ephrinB3-AuNP/LbL surface than on the ephrinB3/LbL surface (Figure 4.6). All these results indicate that the ephrin signaling for focal adhesion is more effective when ephrin molecules are present on the nanostructured surface. On the other hand, the amount of detected paxillin is similar for both Fn/LbL and ephrinB3/LbL substrates. The p-paxillin fluorescence images of the cells placed on the ephrinB3-AuNP/LbL substrate also indicate that the cytoskeletal actins are mainly distributed around the edge line of a cell and the amount of p-paxillin in the western blot data was lower than the value on AuNP/LbL and Fn-AuNP/LbL (Figure 4.7). It attests that focal adhesion of CAMA-1 cells was stronger for ephrin-free AuNP surfaces than other substrates. Paxillin is the first component to appear visibly organized in protrusive regions of the cells.[37] The paxillin seemed to remodel from older to new adhesion at the leading edge, when a new protrusion formed. In our study, CAMA-1 cells have a polarized shape and extend protrusions with lamellipodia, filopodia on the AuNP/LbL and Fn-AuNP/LbL substrates. It is for this reason that the amounts of paxillin and p-paxillin on AuNP/LbL and Fn-AuNP/LbL are high and more paxillin clusters than on other substrates were observed in cellular protrusion areas (Figures 4.6 and 4.7).

4.4. Conclusion

AuNP-modified LbL polymer substrate offers a nanotopgraphical, biologically functional and flexible platform for understanding and controlling the phenotypic changes of human breast metastatic cancer cells. The LbL polymer films could provide a handle to control surface charge and mechanical property that allows for mimicking in-vivo-like extracellular matrix. We demonstrate the flexible and versatile LbL platforms which offer a cell culture substratum to easily modify nanoparticles and to create the intimate contacts between cells and surface. Our results suggest that the AuNP surface density and nano-clustered proteins on a spherical AuNP are critical factors for the efficient signaling and interfacing metastatic cells. In particular, the existence of nano-topographical features is very important in inducing more dramatic changes in metastatic cell adhesion, protrusion, polarity and motility. We further found that AuNP-modified LbL surfaces caused the effective cell adhesion through the stimulation of phosphorylation of paxillin by tyrosine kinase with rigorous cell surface projections that is similar to Fn-AuNP-modified LbL surfaces, indicating high cell motility, even in the absence of Fn on the surface. Moreover, the ephrin signaling for reduced focal adhesion and cell detachment was found to be more effective when the ephrinB3 was exposed to metastatic cells in an ephrinB3-modified AuNP form while the negative focal adhesion signaling was not effective when ephrin was directly attached to the LbL surface. The results imply that nano-topolograpy and 3-dimensional protein clusters are critical in controlling and understanding phenotypic changes and intracellular signaling of metastatic cancer cells and their invasion mechanism. We believe that the strategies and results shown in this study are important in constructing more nature-like metastatic cell-interfacing platforms, studying and controlling metastatic cancer cells, and eventually could give insights for metastatic cancer research, diagnosis, and treatment.

4.5. References

(1) Y. Jang, S. Park, and K. Char, *Korean J. Chem. Eng.* **2011**, *28*, 1149-1160

(2) E. K. F. Yim, E. M. Darling, K. Kulangara, F. Guilak, and K. W. Leong, *Biomaterials* **2010***, 31*, 1299-1306.

(3) L. Yang, B. W. Sheldon, and T. J. Webster, *Journal of Biomedical Materials Research Part A* **2009***, 91A*, 548-556.

(4) E. K. F. Yim, E. M. Darling, K. Kulangara, F. Guilak, K. W. Leong, K. W., *Biomaterials* **2010**, *31* (6), 1299-1306.

(5) L. Yang, B. W. Sheldon, T. J. Webster, *Biomaterials* **2009**, 30 ,20, 3458-3465.

(6) M. Lackmann, A. W. Boyd, *Sci. Signal.* **2008**, 1 ,15, re2-.

(7) M. Nakada, K. L. Drake, S. Nakada, J. A. Niska, M. E. Berens, *Cancer Res.* **2006**, *66*, 8492-8500.

(8) Merlos-Suárez, E. Batlle, *Curr. Opin. Cell Biol.* **2008**, 20 ,2, 194-200.

(9) J. Aoto, L. Chen, *Brain Res.* **2007**, 1184, 72-80.

(10) J. Seo, H. Lee, J. Jeon, Y. Jang, R. Kim, K. Char, J.-M. Nam, *Biomacromolecules* **2009**, 10 ,8, 2254-2260.

(11) J. Cho, K. Char, J. D. Hong, K. B. Lee, *Adv. Mater.* **2001**, 13 ,14, 1076-1078.

(12) M. Tanaka, E. Sackmann, *Nature* **2005,** *437*, 7059, 656-663.

(13) S. S. Shiratori, M. F. Rubner, *Macromolecules* **2000**, 33, 4213.

(14) J. Choi, M. F. Rubner, *Macromolecules* **2005**, 38, 116.

(15) J. D. Mendelsohn, S. Y. Yang, J. Hiller, A. I. Hochbaum, M. F. Rubner, *Macromolecules* **2003**, 4, 96.

(16) A. Schneider, G. Francius, R. Obeid, P. Schwinte, J. Hemmerle, B. Frisch, P. Schaaf, J. C. Voegel, B. Senger, C. Picart, *Langmuir* **2006,** *22*, 1193-1200.

(17) C. S. Chen, M. Mrksich, S. Huang, G. M. Whitesides, D. E. Ingber, *Science* **1997,** *276* , 1425-1428.

(18) M. Arnold, E. A. Cavalcanti-Adam, R. Glass, J. Blümmel, W. Eck, M. Kantlehner, H. Kessler, J. P. Spatz, *ChemPhysChem* **2004,** *5* , 383-388.

(19) M. Arnold, M. Schwieder, J. Blummel, E. A. Cavalcanti-Adam, M. Lopez-Garcia, H. Kessler, B. Geiger, J. P. Spatz, *Soft Matter* **2009,** *5* , 72-77.

(20) M. Arnold, V. C. Hirschfeld-Warneken, T. Lohmu¨ ller, P. Heil, J. Blu¨mmel, E. A. Cavalcanti-Adam, M. Lo´ pez-Garcı´a, P. Walther, H. Kessler, B. Geiger, J. P. Spatz, *Nano Lett.* **2008,** *8* , 2063-2069.

(21) T. P. Kunzler, C. Huwiler, T. Drobek, N. D. Spencer, *Biomaterials* **2007,** *28*, 5000-5006.

(22) J. Zimmerberg, M. M. Kozlov, *Nat. Rev. Mol. Cell Biol.* **2006,** *7* , 9-19.

(23) M. Lackmann, A. W. Boyd, *Sci. Signal.* **2008,** *1* , re2-.

(24) M. Nakada, K. L. Drake, S. Nakada, J. A, Niska, M. E. Berens, *Cancer Res.***2006,** *2006*, 8492-8500.

(25) A. Merlos-Suárez, E. Batlle, *Curr. Opin. Cell Biol.* **2008,** *20*, 194-200.

(26) J. Aoto, L. Chen, *Brain Res.* **2007,** *1184*, 72-80.

(27) Y. Abe, T. Tsutsui, J. Mu, A. Kosugi, H. Yagita, K. Sobue, O. Niwa, H. Fujiwara, T. Hamaoka, *Cancer Sci.* **1997**, 88 , 64-71.

(28) I. S.-P. Dobrzyńska, S. Sulkowski, Figaszewski. *Mol. Cell Biochem.* **2005**, 276, 113-119.

(29) T. N. Campbell, S. Attwell, M. Arcellana-Panlilio, S. M. Robbins, *Biochem. Biophys. Res. Comm.* **2006**, 350 , 623-628.

(30) M. Tanaka, K. Sasaki, R. Kamata, R. Sakai, *J. Cell Sci.* **2007**, 120 , 2179-2189.

(31) S. K. Mitra, D. A. Hanson, D. D. Schlaepfer, *Nat. Rev. Mol. Cell Biol.* **2005**, 6 , 56-68.

(32) G. W. McLean, N. O. Carragher, E. Avizienyte, J. Evans, V. G. Brunton, *Nat. Rev. Cancer* **2005**, 5 , 505-515.

(33) B. Geiger, J. P. Spatz, A. D. Bershadsky, *Nat. Rev. Mol. Cell Biol.* **2009**, 10 , 21-33.

(34) Z. K. Melkoumian, X. Peng, B. Gan, X. Wu, J.-L. Guan, *Cancer Res.* **2005**, 65 , 6676-6684.

(35) D. Wang, J. Grammer, C. Cobbs, J. Stewart, Z. Liu, R. Rhoden, T. Hecker, Q. Ding, C. Gladson, *J. Cell Sci.* **2000**, 113 , 4221-4230.

(36) B. D. Cox, M. Natarajan, M. R. Stettner, C. L. Gladson, *J. Cell Biochem.* **2006**, 99 , 35-52.

(37) P. Friedl, K. Wolf, *Nat. Rev. Cancer* **2003**, 3 , 362-374.

Chapter 5.

Multilayered Co-Culture Platforms with Nanoporous Membranes for Analysis of Cell-Cell Communications

5.1. Introduction

Cells within a tissue interact with neighboring cells or extracellular matrices (ECM) through diverse biochemical and/or mechanical cues to maintain homeostasis and tissue function.[1] In many biological systems, cells communicate with each other generally through direct contact (i.e., gap junction, tight junction) or trade of soluble factors (i.e., cytokines, chemokines, growth factors).[2] Particularly, tumor development including cancer initiation, promotion and progression has been considered as the result of an evolving crosstalk between carcinoma cells and various types of stromal cells in the surroundings (i.e., fibroblast, myoblast, immune cell and mesenchymal stem cell to name a few).[3-4] In this regard, the importance developing of cell co-culture platforms and tools for analyzing communications between cancer and stromal cells has frequently been emphasized in recent cancer research as a way towards fully understanding and controlling tumor cell behavior and as a method for providing pivotal and unheralded information concerning the basic biology of cancer.[5]

Many previous studies regarding cell-to-cell communication involving paracrine soluble factors were mainly based on membrane-separated cell co-culture platforms with indirect contact between different cell types.[6] Such systems allow for ready control over cell environment and cell-to-cell communications, providing insights into the molecular bases and

governing factors of cancer cell development. However, the lack of cytokine-mediated cell-cell interactions in this co-culture systems was reported as a major reason for the loss of *in vivo*-like-functionality of cells of interest.[4] The limited cell-cell interaction is attributed mainly to the separating membrane which feature low pore density and micrometer-scaled thickness. Moreover, optically non-transparent cell culture substrates impose difficulties in imaging and analyzing specific cells of interest. As an alternative approach, various kinds of cells were directly cultured on a tissue culture substrate for *in vitro* studies.[7] However, such direct contact co-culture systems have numerous technical issues including cross-contamination of cells by xenogenic reactions, difficulty in isolating of a specific cell line, lack of flexibility in ways of choosing cell lines of interest, and hardship regarding isolated analysis on each cell line. The most serious problem in the direct contact systems is the evaluation of the relative synthesis of soluble factors because the total cytokine expression content of each cell type cannot be distinguished.[8]

Herein, we have developed a transparent and transferable nanoporous (TTN) cellulose acetate (CA) membrane-based cell co-culture platform to address aforementioned issues in cell co-culture assays. The TTN CA membrane described in this chapter provides for a very thin and highly porous membrane for membrane-separated co-culture platform mediating cytokine-based cell-cell communications. The TTN membrane based platform allows for facile cell-cell communication across the separating membrane while enabling isolation of specific cell lines and distinguishing the expression of various soluble factors according to each cell type.

5.2. Experimental Section

Preparation and Characterization of Porous Freestanding Polymer Thin Films Cellulose acetate (CA) with average number of molecular weight (M_n) of 30,000 g/mol (39.8 wt % acetyl labeling extent) was obtained from Aldrich and used as received. CA is dissolved in a good solvent, acetone, with concentration of 4 wt%. To obtain porous structure of CA thin films, the spin-casting of CA solutions was performed with spinning rate 3000 rpm for 20 s using an automatic spin coater in closed humid chamber with controlled relative humidity (RH) as shown in Figure 5.1. Since water is a non-solvent for CA polymers, the porous structure in the CA thin films can be developed by non-solvent vapor induced phase separation (VIPS) and the number of pores was controlled by the RH (i.e., water vapor) in the closed chamber packed with different types of supersaturated salt solutions ($CaCl_2$ and KCl for RH 25-45 % and 55-85 %, respectively). The freestanding CA thin films were obtained by immersing the CA-coated NaCl substrates into water for 10 min after efficient drying of the samples. The surface morphologies of CA thin films were characterized by AFM (diInnova, Veeco Instruments Inc.) and FE-SEM (JSM-6701F, JEOL). The thicknesses of the CA thin films were obtained from step height measurement (AlphaStep IQ (Rev. Al-1), KLA Tencor). To enhance cell adhesion, the CA membranes were first coated by polydopamine in dopamine hydrochloride solution for up to 16 hrs. The dopamine hydrochloride (Sigma) was dissolved in 10 mM Tris buffer with concentration of 2 mg/ml, and the solution pH was adjusted at 8.5 with dilute NaOH solution. The basic principle and detailed characteristics of polydopamine coating have been described in detail elsewhere.[9]

Cell Culture The MDA-MB-231(ATCC Num. HTB-26), NIH-3T3 (ATCC Num. CRL-1658), and C2C12 (ATCC Num. 1772) were purchased from American type culture collection and human mesenchymal stem cell (hMSC) was purchased from Merk Millipore (Part # SCC034,

MA, USA). The MDA-MDA-231, metastatic breast carcinoma cell, was culture in 10% fetal bovine serum (FBS) contained RPMI media (Gibco, USA) with 100 units/ml penicillin-streptomycin (Gibco,USA) The NIH-3T3 and C2C12 were grown in DMEM (Gibco, USA) with 10% FBS and antibiotics. The hMSC were cultured in mesenchymal stem cell expansion medium (SCM015, Merk Millipore, USA). And we used the hMSC between 4^{th} and 8^{th} passages. All cell lines were incubated at 37 ^{o}C, 5 % CO_2.

Layer Stacking for Cell Co-Culture Breast cancer cells (Cell Conc. = 6.6 X 10^4) and stromal cells (Cell Conc. = 3.3 X 10^4), cell number ratio was 2:1, were seed into CA film respectively. After 4 hrs of cell seeding (this time was enough for cell adhesion on the CA film, so could prevent directly contact between metastatic cancer cell and stromal cells), cancer cultured film and stromal cultured film were stacked in a clean well to observe cell-cell interactions. To prevent floating of film in cell culture media during cell culture, we made the stainless-contained PDMS ring which could press the stacked layer. For more exclusive observation of co-culture effect, cells were cultured for 2 days at 37 ^{o}C, 5 % CO_2.

Cytokine Assay To detect seventeen different cytokines, we used Milliplex Map (Merk Millipore, USA). After 2 days of cell culture, we collected media to quantify of cytokine in culture medium. Milliplex Map is based on the luminex that uses proprietary techniques to internally color-code microspheres with two fluorescent dyes. The sample was incubated with bead which was coated with specific biotinylated-antibody. And then, the reaction mixture was incubated with streptavidin PE conjugate. The signal from microspheres was detected by a laser, which excite internal dyes marking the microsphere set. We repeated six times this experiment for test of reproducibility and error bars. And we obtained the standard curve of each cytokine and background signal from cell culture media for normalization of data.

Actin Staining After cell co-culture via layer stacking, cell culture medium was harvested, and cells were washed twice with PBS solution. Cells were then fixed by 4 % paraformaldehyde/PBS for 15 min. Cells were washed with PBS solution three times (5 min for each time). To block nonspecific binding, we used 1 % BSA/PBS/0.3 % tween20 for 15 min, and the cells were washed with PBS solution afterwards. And then each layer was separated and was moved to empty well to label cell individually. Phalloidin-Tetramethyl rhodamine isothiocyanate (TRITC) (Sigma-Aldrich, CA, USA) and phalloidin-Fluorescein isothiocyanate (FITC) (Sigma-Aldrich, CA, USA) was diluted to 5 % with PBS solution. The Phalloidin-TRITC solution was added to MDA-MB-231 contained well and the Phalloidin-FITC solution was used to stain of three stromal cell lines. After incubation, cells were washed with PBS solution two times. Finally, the stained cell samples were mounted by mounting buffer (Abcam, United Kindom) and were examined under a confocal laser scanning microscopy (Nikon, Japan).

Migration Assay First, each cell line was cultured on CA film (Cell Conc. = 1.0 X 10^5) and cells on three different co-culture conditions (breast cancer cell: stromal cell ratio = 2:1, Total cell conc. = 1.0 X 10^5) were grown for 2 days. After 2 days of cell culture, the media was collected and 500 μL was transferred to the lower chamber of migration assay kit (ECM 508, Merk-Millipore, USA) for observing the effect of cytokine in media on cancer cell migration. The suspension of MDA-MB-231 cells (300 μL) was added into each insert chamber with micro pore. The plate was covered and was incubated for 24 hours at 37°C in a CO_2 incubator (5% CO_2). The cells and media from the top side of the insert were removed carefully by pipetting out the remaining cell suspension. And the insert chamber was moved into a clean well containing 400μL of cell stain solution. After incubation for 20 minutes at room temperature, the chamber was dipped into a beaker of water several times to rinse. After washing, non-migration cells layer was removed through a cotton-tipped swab. And

then transfer the stained insert chamber to a clean well containing 200 μL of Extraction buffer for 15 minutes at room temperature. The stain from the underside was extracted by gently tilting the insert back and forth several times during incubation. Finally, extracted solution (100μL) transferred to 96-well plate for colorimetric measurement at 560nm.

Gelatin Zymography After culture of cells on co-culture condition or not for 2 days, the media was collected. For zymography assays which could determine the expression of MMPs, all of the conditioned medium were quantified and were diluted by the addition of sample buffer (sample buffer 0.5M contains Tris HCl 0.2 M, SDS 4%, Glycerol 40%, Bromophenol blue 0.004%) that did not contain mercaptoethanol and was not boiled. The prepared samples were loaded into 10% SDS-polyacrylamide gels containing 0.2% gelatin substrate and were separated (Hoefer, MA, USA). After electrophoresis, the gels were washed in 50 mM Tris-HCl (pH 7.4) containing 2.5% Triton X-100. The gels were then washed in 50 mM Tris-HCl (pH 7.4) buffer, followed by incubation in buffer containing 50 mM Tris-HCl (pH 7.4), 0.02% sodium azide and 10 mM $CaCl_2$. After washes in deionized water, the gels were stained with 0.25% Coomassie Blue, destained in 10% methanol containing 10% acetic acid.

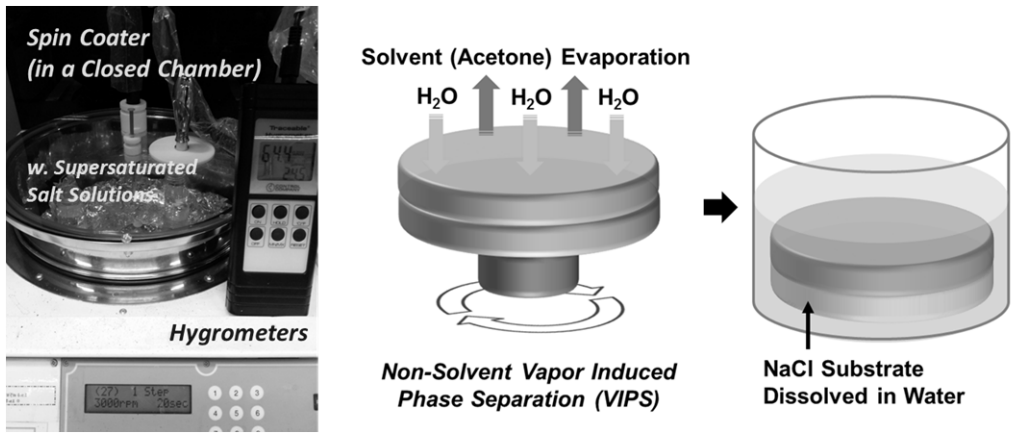

Figure 5.1. Equipment and a schematic representation on the preparation of porous cellulose acetate (CA) membrane.

5.3. Results and Discussion

5.3.1. Development of Porous Membrane Platforms for Cell Co-Culture

We have developed cellulose acetate (CA) membrane-based cell co-culture platform to address aforementioned issues in cell co-culture assays. CA is a commercially available biocompatible polymer and is useful for the preparation of filter membranes due to its low static charges and high mechanical strength.[10] In order to prepare a CA membrane for cell culture, CA solution in acetone (4 % w/w) was spin-coated on a NaCl substrate in a closed chamber with a controlled relative humidity (RH) of 65 %. The porous structure of a CA membrane was formed by non-solvent (water) vapor-induced phase separation (VIPS), and the freestanding CA membranes were obtained by dissolving the substrate. These freestanding CA membranes with porous structures have unique characteristics such as transparency and transferability in an aqueous environment such as cell-culture media (Figure 5.2). The transparency of the CA membranes was originated form the nanometer scale dimension in film thickness (482 ± 7 nm) and pore size (≤ 500 nm), and the properties of CA, such as high mechanical strength, low static charges and low water solubility allows for easy handling (i.e., transferability) of the prepared freestanding membrane in an aqueous environment even with its nanometer-scale thickness**.**

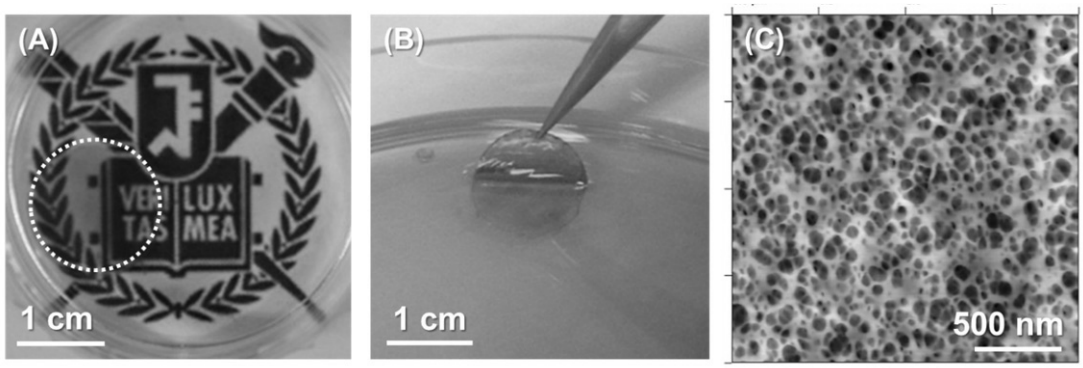

Figure 5.2. (A) Transparency, (B) transferability and (C) nanoporous structures of CA membranes in aqueous environments.

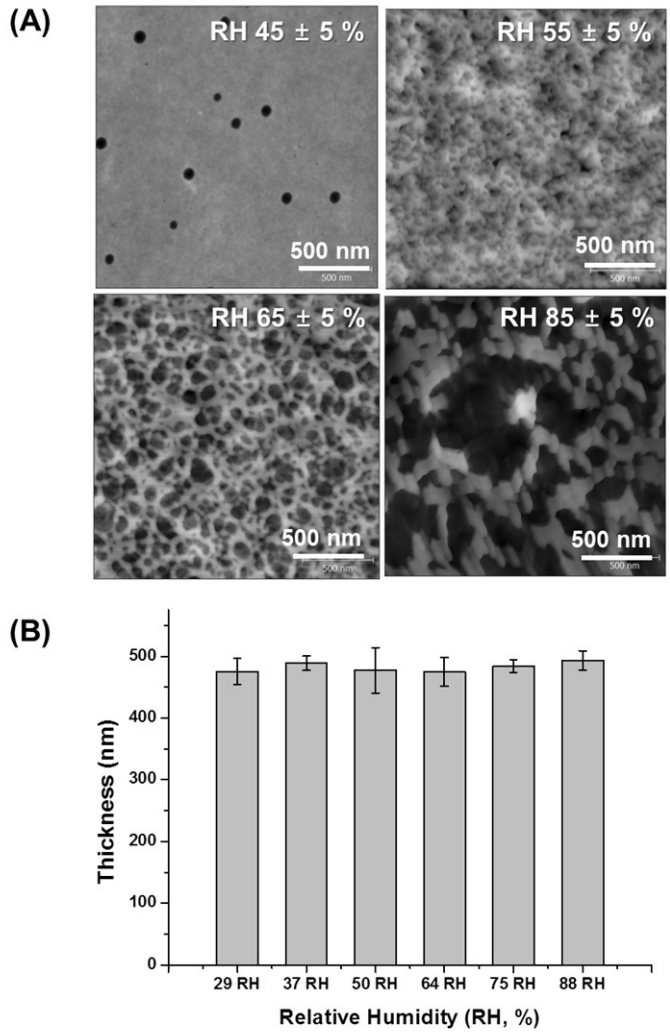

Figure 5.3. (A) AFM images of nanoporous CA membranes prepared in different conditions, RH = 45, 65 and 85 %. (B) Uniform thicknesses of the CA membranes prepared from solutions of identical concentration (4 % w/w in acetone), regardless of RH in the spin coating chamber.

As proof-of-concept experiments, human breast metastatic cancer cell (MDA-MB-231) and human mesenchymal stem cell (hMSC) were co-cultured by stacking the TTN membranes containing each cell line. The CA membrane with different pore sizes and thicknesses were used to study the effect of the pore size, pore morphology and pore density on cell-cell communications. The pore size of CA membranes could be controlled by varying RH during spin-coating whereas their thicknesses were maintained at around 500 nm, regardless of RH (Figure 5.3). All the CA membranes used for cell culture were pre-coated with polydopamine to enhance cell adhesion, and polydopamine coating significantly increased the stability of cells on the membrane while keeping the porous morphologies of CA membranes as was seen through atomic force microscopy (AFM; data not shown in this thesis). Comparison of cells cultured on control culture dish, polydopamine-coated CA membranes, and as-prepared CA membranes confirmed the stability of cell adhesion on our stacked co-culture system (Figure 5.4). The density of cells decreased on bare CA film, whereas it was maintained on poy(doplamine)-coated CA film. The data indicate that polydopamine-modified CA membrane platforms enhance cell adhesion and stability during co-culture assay. In addition, CA membrane in this study is about 30 times thinner and has larger number of pores compared to the commercially available membrane culture inserts (Figure 5.5). The high porosity and adequate pore size are required for cell seeding and nutrient diffusion. Our nanoporous membrane could permit signaling molecules between co-cultivated cells via diffusion while preventing intermixing of the cells, making possible the isolation of pure population of two or more cell types on nanoporous film.

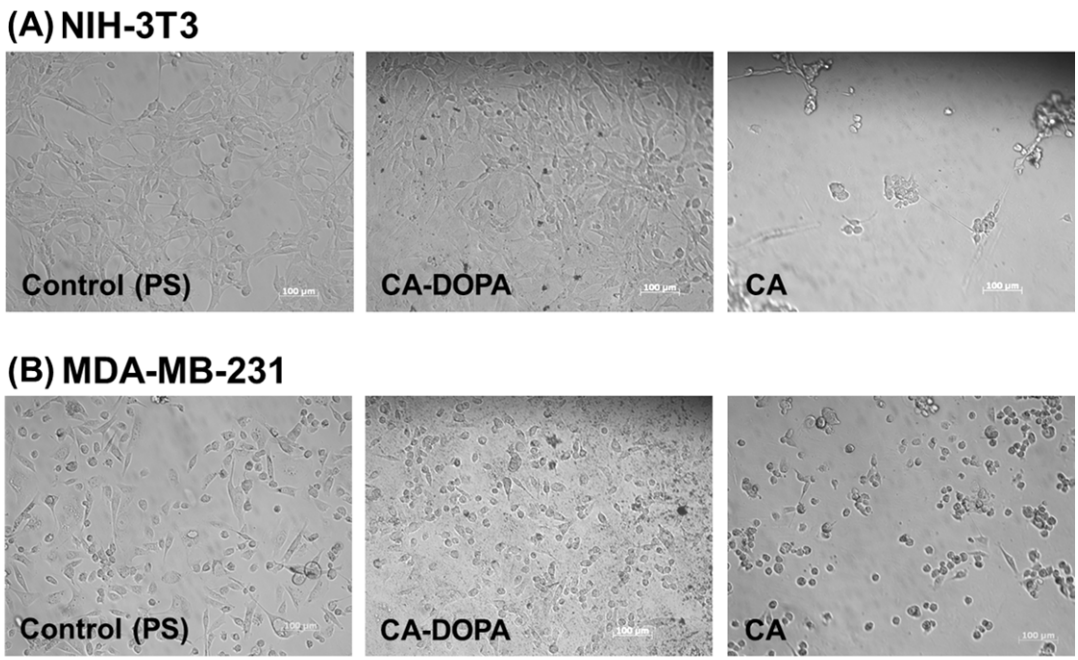

Figure 5.4. The effect of poly(dopamine)-coating on the cell adhesion. DIC images of (A) NIH-3T3 and (B) MDA-MB-231 cells cultured on dishes for cell culture, polydopamine-coated CA membranes and as-prepared CA membranes.

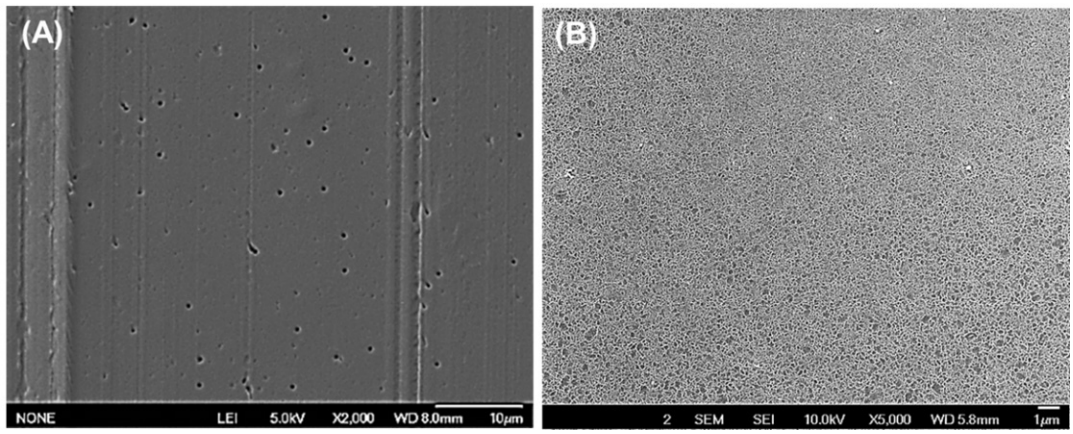

Figure 5.5. SEM images of (A) commercially available PET membrane cell-culture insert and (B) CA membrane platform designed in the present study.

5.3.2. The Effect of Pore Size, Pore Density and Film Thickness of Polymer Membranes on the Cell-Cell Communication

Cell-cell communications between MDA-MB-231 and hMSC via RANTES were analyzed by luminescence-based cytokine assay (Figure 5.6A). RANTES, also known as CCL5, is triggered in hMSCs by surrounding MDA-MB-231 cells and the action of RANTES is responsible for much of the cancer cell growth, metastasis and the tumorigenesis.[4,10] In particular, it is well-documented that RANTES might contribute to breast cancer metastasis through the recruitment of a number of stromal cells to sites of primary tumor growth.[12] However, it was clearly reported that this RANTES induction requires close physical contact between MSCs and MDA-MB-231 cells, because the RANTES secretion fails when the two cell lines were separated by commercial permeable membranes.[4] In this regard, detecting the RANTES expression when the hMSCs are co-cultured with MDA-MB-231 cells through porous CA membrane stacking is important for demonstrating the efficacy of our CA membranes for analysis of the cell-cell communications. While commercially available PET membrane resulted in low RANTES secretion, our CA membrane, 482 nm thick and prepared at RH 65%, displayed large amounts of RANTES secretion, similar to that observed when two cell lines were co-cultured in a direct contact. The typical PET membranes have 10 μm thickness and low pore density**,** resulting in low amounts of the RANTES secretion (Figure 5.6B). It should be also noted that 10-μm-thick CA membranes were used in this study to eliminate the effect of membrane thickness on the results. The porous 10-μm-thick CA films were prepared by non-solvent liquid induced phase separation (N-LIPS): the 20 % w/w CA solution dissolved in 2-ethyl-1,3-hexanediol (EHD) was dropped onto a Si wafer constructed with 10-μm-sidewalls and casted by doctor blade method. The prepared CA films were immersed into water for 1 hour then dried in vacuum for 12 hours, a procedure which made the film easily detachable from the substrate. The results of membrane-thickness dependence

clearly show that there is a linear relationship between membrane thickness and cytokine communication between cells (Figure 5.6C)**.** From these results, we learned that the CA membrane with thickness around 500 nm, prepared with a 4 % w/w solution at RH 65 %, is optimal for our studies, generating high RANTES expression result without compromising membrane durability and transparency. The membrane developed in this study could play a major role as a new membrane-separated co-culture platform mediating cytokine-based cell-cell communications, because the direct cell co-culture methods still have many technical difficulties concerning isolation of a specific cell line and distinguishing the expression of various soluble factors according to each cell type. The membrane developed in this study could play a major role as a new membrane-separated co-culture platform mediating cytokine-based cell-cell communications. This CA membrane optimized for the analysis of cytokine-based cell-cell communication is denoted as *"TTN (transparent, transferable and nanoporous) membrane"* in this study with respect to its unique properties as compared to previous cell-culture insert membranes.

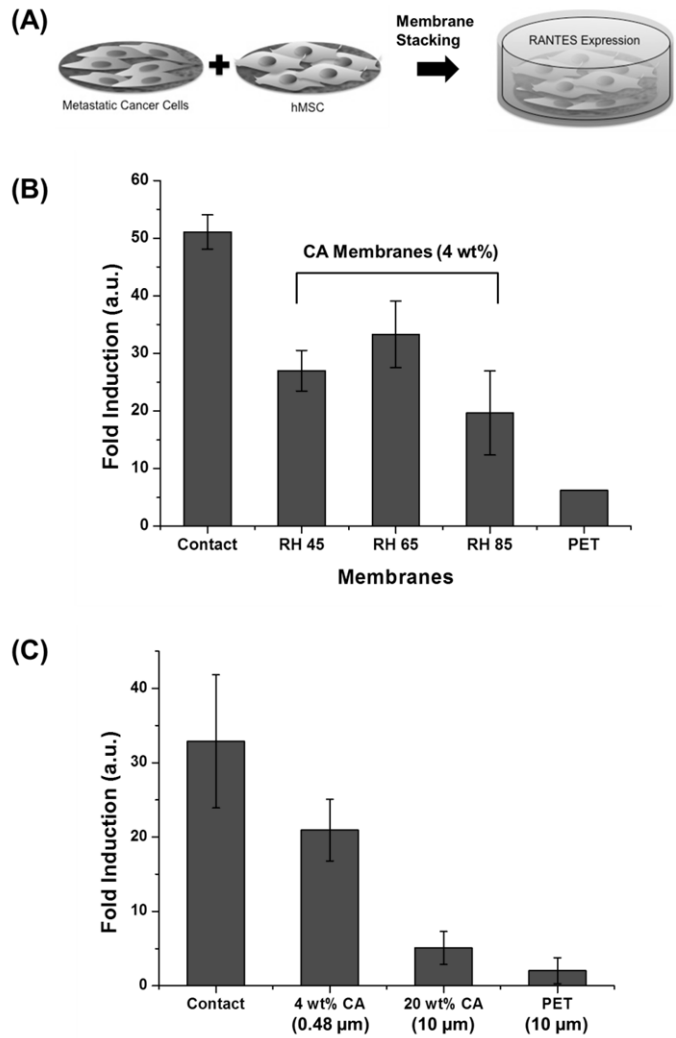

Figure 5.6. (A) Schematic description of the co-culture of MDA-MB-231 and hMSCs using a CA membrane for cytokine analysis. (B) The effect of pore size on the RANTES expression triggered by the cytokine-mediated communications between MDA-MB-231 and hMSC. (C) The effect of film thickness on the RANTES expression.

5.3.3. Novel Co-Culture Platforms for Analysis of Cell-Cell Communications Based on the Transferable, Transparent and Nanoporous Polymer Membrane

We have further investigated the interactions between human breast metastatic cancer cell [MDA-MB-231 (M)] and three different types of stromal cell lines [hMSC (H), fibroblast NIH-3T3 (N), and myoblast C2C12 (C)] in cell co-culture assays with a variety of cell types using the TTN membrane (Scheme 5.1). Communications and interactions among cancer cells and various types of stromal cells have been considered to play an important role in cancer initiation, promotion, and progression. In particular, cancer metastasis depends on the presence of cross-talk between carcinoma cell and stromal cell in primary tumor site and metastatic target organs.[11,14] The growing tumor cells actively recruit hMSCs, considered as a tumor-associated stromal cell type, through the secretion of various endocrine and paracrine signals.[15] Fibroblasts and myoblasts also significantly affect the growth and progression of tumor *via* releasing of cytokine *in-vivo*.[16] In this regard, we chose the four cell lines [metastatic breast cancer cell, hMSC, fibroblast, and myoblast)] to investigate the orchestrated reaction between cancer cells and stromal cells. As a typical experiment, to better understand the crosstalk between breast cancer cell and stromal cells, the cell cultured media which have different (co-)cultivated cell lines were screened to analyze the levels of various cytokines, chemokines and growth factors using luminex-based suspension array system (Figure 5.7).

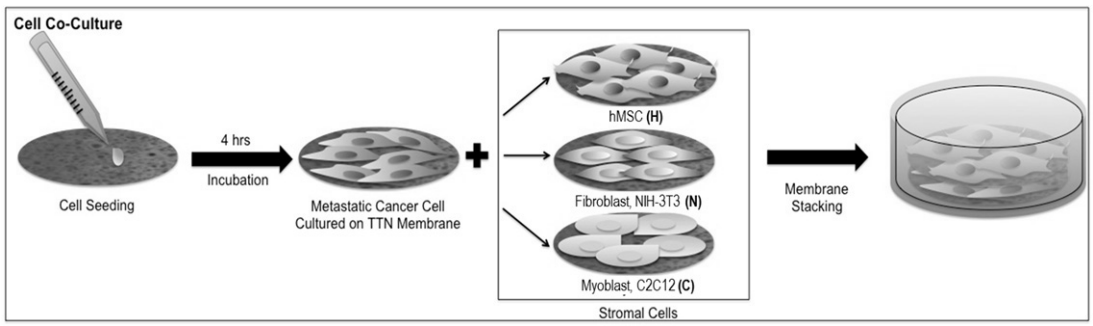

Scheme 5.1. A schematic diagram of the co-culture of metastaic cancer cells (MDA-MB-231) and three different types of stromal cells using stacked TTN membranes containing each cell line.

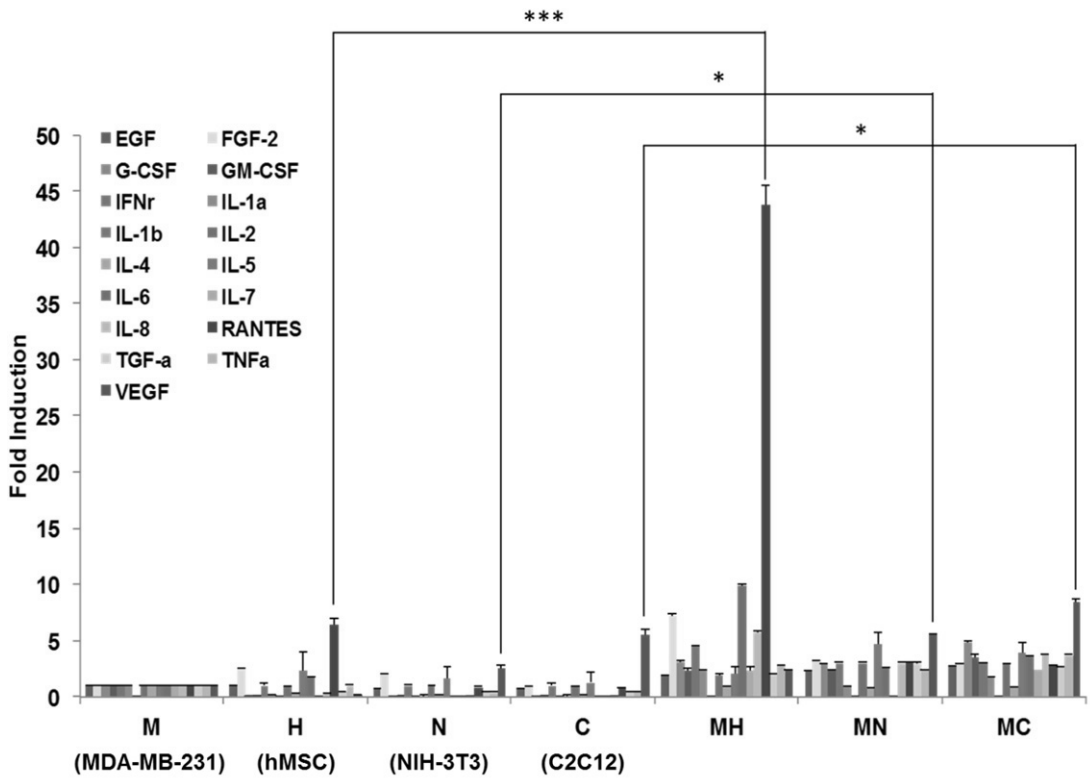

Figure 5.7. The results of cytokine assay using the luminescence-based method. The data was obtained from cell culture media after the co-culturing MDA-MB-231 (M) with three different stromal cell lines [hMSC (H), NIH-3T3 (N) and C2C12 (C), named as MH, MN and MC, respectively] for 2 days. Data are representative of multiple independent experiments and are expressed as mean ± standard deviation. (*; P <0.05, ***; P< 0.01)

In the cytokine-assay, the fold induction of each cytokine species was normalized to the detected cytokine expression level in MDA-MB-231 cell culture media. First, from single cell line assay results on TTN membranes, remarkably high RANTES level was observed with hMSC cells while relatively larger amount of vascular endothelial growth factor (VEGF) was obtained for NIH-3T3 and C2C12 cells. The cell co-stacking assay results show that there is significant increase in RANTES amount for the $M_{bot}H_{top}$ case, and the noticeably increased VEGF amount was measured for $M_{bot}N_{top}$ and $M_{bot}C_{top}$ cases. These experimental results suggest that the induction and change in amount of characteristic cytokines from metastatic MDA-MB-231 cells are closely associated with neighboring stromal cell types as well as that the TTN membranes can serve as co-culture platforms which allow for accurate analysis of the cytokine-based cell-cell communications.

Further, we studied the effect of stacked TTN membrane co-culture on the migration and invasiveness of metastatic MDA-MB-231 cells by using the transwell assay and the gelatin zymography to detect matrix metalloproteinase (MMP) (Figure 5.8A). In the migration assay, the optical density (O.D.) of co-cultured samples ($M_{bot}H_{top}$, $M_{bot}N_{top}$ and $M_{bot}C_{top}$) was higher than single cell line-cultured cases (M, N and C), indicating that the migration of MDA-MB-231 cells is positively affected by the co-culture of stromal cells. Tumor cells also need to cross basement membranes to invade into surrounding tissues as the tumor mass expands in size.[17] Since the MMP has the ability to degrade the components of basement membrane and acts as a facilitator of tumor cell invasion and metastasis, MMP has been considered as a marker of tumor metastasis.[17-18] As the result of co-activated interactions between MDA-MB-231 cells and stromal cells, the stronger active MMP bands were observed in co-culture conditions than single cell line-cultured cases in gelatin zymography (Figure 5.8B).

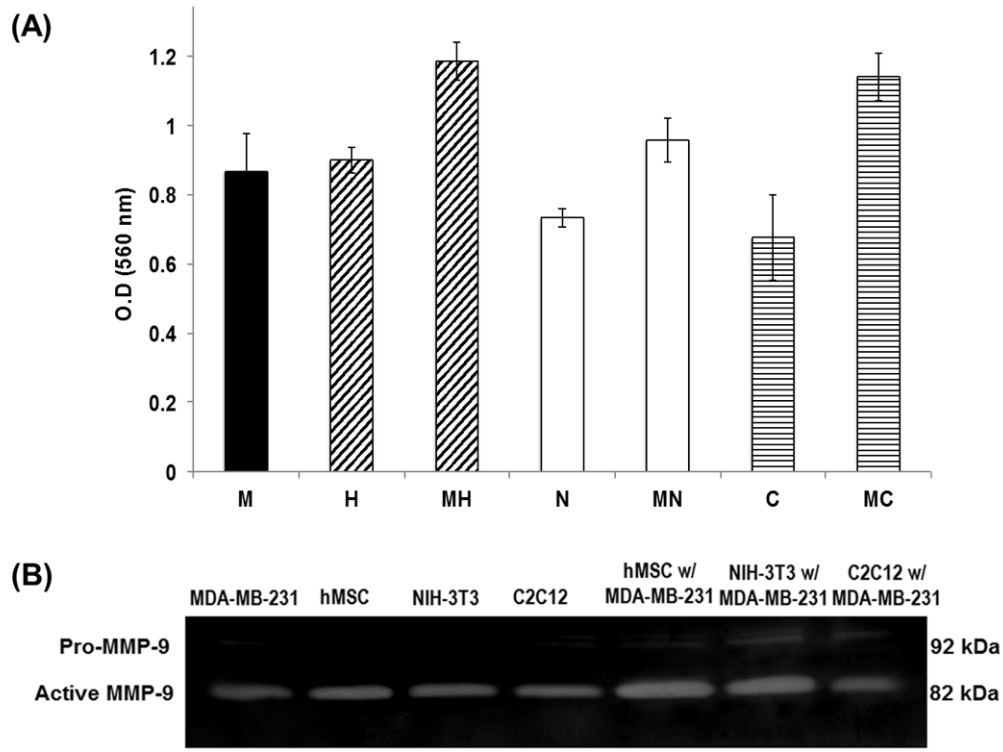

Figure 5.8. (A) The migration assay of M using a transwell system. The optical density (O.D) at 560 nm represents the degree of migration and (B) the gel image of gelatin zymography for comparison invasiveness between each condition. The band intensity highly depends on the activity of active MMP.

It is well known that RANTES acts in a paracrine fashion on cancer cells to increase their mobility, invasion and metastasis, and increased RANTES secretion could also promote expression of MMP 9.[19] Also, VEGF, which is typically secreted from mammary or stromal (myo)fibroblasts, stimulates angiogenesis, and is an important factor for tumor proliferation and migration.[20] Our results suggest that increased VEGF levels in $M_{bot}N_{top}$ and $M_{bot}C_{top}$ co-cultures played an important role in activating the migration and invasiveness of MDA-MB-231 cells. We anticipate that the TTN membrane-based cell co-stacking assay could selectively identify key cytokine or growth factor for inducing a specific cell phenotypic result via cell-cell communications.

We also applied the TTN membranes as a multicellular-co-culture platform to overcome the limitations of conventional cell co-culture methods (i.e., direct contact or membrane-separated co-culture methods) by utilizing the optical transparency, transferability, and structural flexibility of the TTN membrane. The transparent nature of TTN membrane allows for *in-situ* monitoring of the cell morphology on each stacked-layer through optical microscopy and the confocal laser scanning microscopy techniques (Figure 5.9). In addition, it was confirmed that every cell line is alive and maintains each proliferation rate without cross-contamination during co-culturing on by TTN membranes stacked up to 4 layers. The cytokine assay in which TTN-based multicellular co-culture system demonstrated intercommunication between multi-stacked cells are also maintained, as shown in Figure 5.10**.** The result indicates that during co-culturing with TTN membranes, cell lines recognize each other by paracrine signaling, and, in this reason, produce the different types of cytokines in various amounts depending on the co-cultured cell types. Such multi-stacked TTN platforms would offer a novel method of culturing cells more than two types simultaneously, which would provide a useful platform for understanding cell behavior in *in-vivo*-like environment.

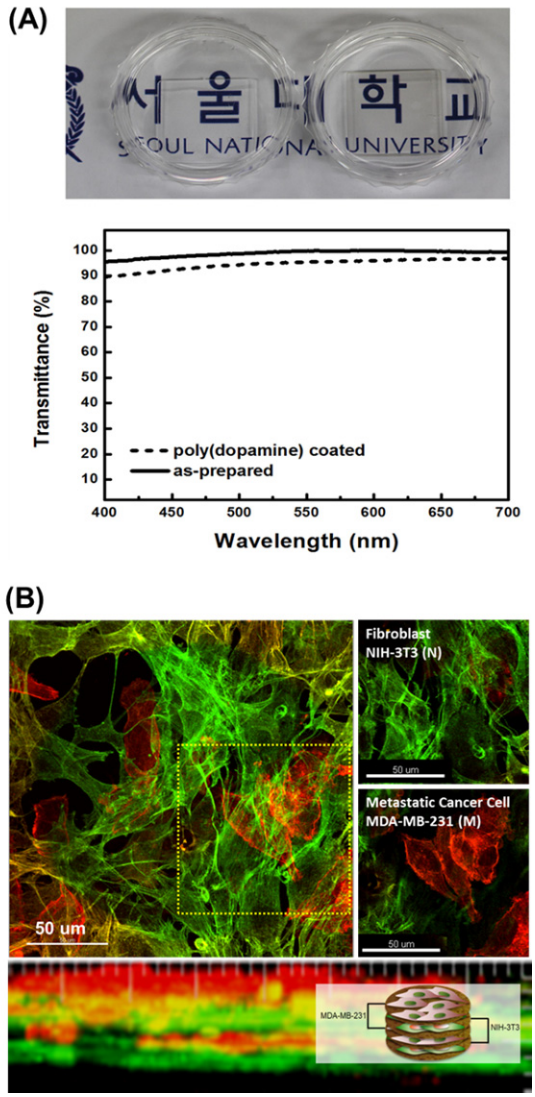

Figure 5.9. (A) Optical images of TTN membranes before (left) and after (right) poly(dopamine) coating in PBS solution. Transmittance (%) of TTN membranes coated onto quartz substrates before (solid) and after (dashed) poly(dopamine) coating measured by UV-Vis spectroscopy. (B) The fluorescence images of multi-stacked TTN membranes containing alternately stacked two different cell lines (N: Green and M: Red), obtained by confocal laser scanning microscopy (CLSM).

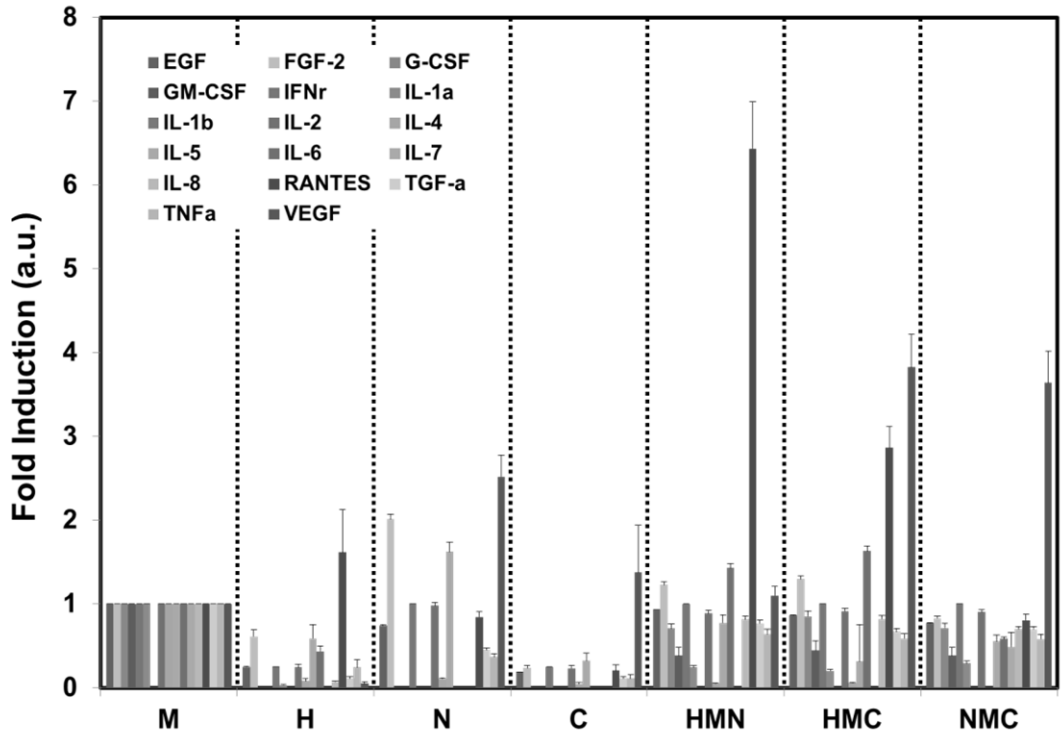

Figure 5.10. The cytokine assay after co-culture with three different cell lines multi-stacked with TTN membrane.

Based on the transferability of the TTN membrane, we have designed another experiment named as "*TTN membrane shuffling co-culture*" that enables evaluation of the significance of the sequential culture of stromal cell with M (Figure 5.11). Previously, it was reported that endothelial cells activated by tumor cells in co-culture condition induce self-activation of non-co-cultured endothelial cells through autocrine loops.[21] However, this experimental system cannot provide a tool for studying the interaction between tumor and many different types of stromal cells simultaneously. By *the shuffling co-culture* method, it is clearly confirmed that different levels of cytokine expressions are detected according to the designed sequence of co-cultured stromal cell, even in cases where the combination of co-cultured cell lines are identical. For example, the release of FGF-2 was increased in MH under the sequence effect of MN interaction whereas IL-5 was stimulated under the same MH conditions by the influence of MC communications. Notably, the level of specific cytokines, FGF2 and IL-5, on each condition reflected a synergistic interaction between stromal cells in *shuffling co-culture*, as they are higher than those produced by M culture alone. On the contrary, RANTES in MH and VEGF in MC are consistently released regardless of the shuffling sequence of the TTN membranes onto other stromal cells.

The TTN membrane-based co-culture platform facilitates the detailed analysis of the intercommunication between metastatic cancer cell and several types of stromal cells based on the advantages of facile stacking and destacking of the membranes. We anticipate that our study could serve as a way to develop a straightforward and cost-effective method for cell-co-culture and analysis.

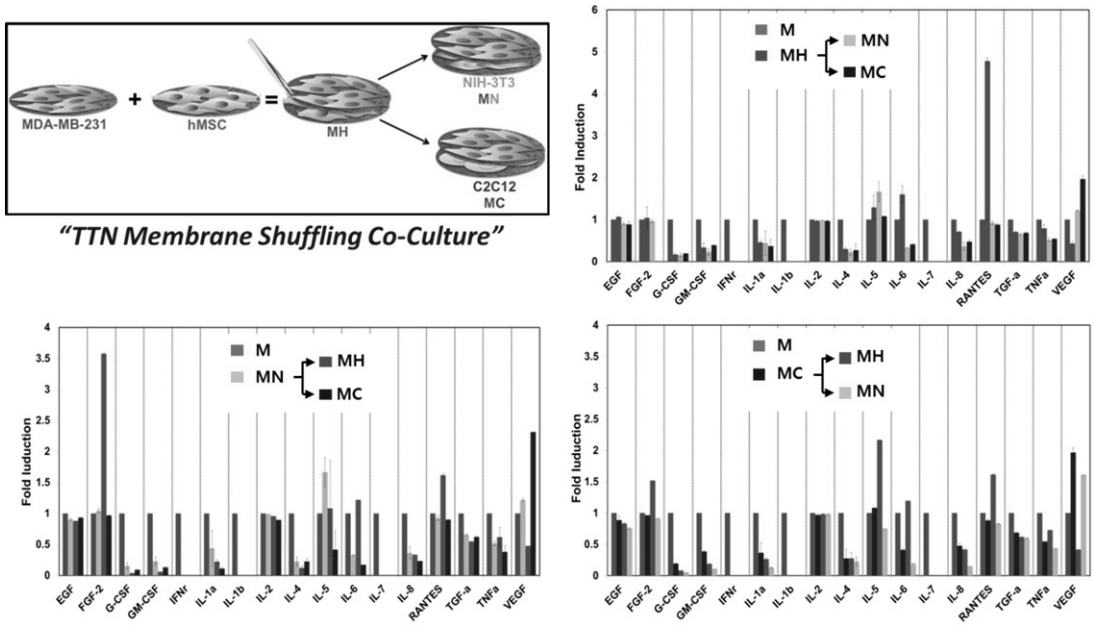

Figure 5.11. A schematic diagram of TTN membrane transfer and shuffling. The TTN membrane containing M was cultured with a stromal cell (H, N or C) and then transferred to another stromal cell-contained TTN layer. The graph shows the result of cytokine assay as a function of stromal cell type co-cultured with M for 1 day.

5.4. Conclusion

To study crosstalk and coevolution of tumor and stromal cells, we have developed cellular co-culture platforms based on nanoporous and freestanding cellulose acetate (CA) thin films. We cultured breast metastasis cancer cell (MDA-MB-231) and three different stromal cells (i.e., human mesenchymal stem cell (hMSC), fibroblast (NIH-3T3), and myoblast (C2C12)) on CA membranes. The freestanding CA membranes allow each cell layer to stack and separate, maintaining the interaction between two different cell lines and removing the limitation of cultured-cell types in a well. We also observed that human breast cancer cells co-cultured with stromal cells via CA membranes show increased metastatic potency. The amount of chemokine RANTES (also called CCL5) from mesenchymal stem cells and VEGF (vascular endothelial growth factor) from fibroblasts and myoblasts was increased in co-culture systems. These molecules, secreted from stromal cells, act in paracrine fashion to promote motility, invasion, and metastasis of metastatic cancer cells. The high pore distribution and low thickness of the membranes allowed for a cooperative induction of RANTES between breast cancer cells and hMSC, a process which requires close contact between the cell lines. The co-culture systems based on transparent, transferable and nanoporous (TTN) membranes facilitate screening of cytokines and proteins from various conditions and give better understanding of the contributions of stromal cells to cancer progression. The platforms designed in this study could help elucidate underlying processes involved in diseases related to cell-cell interactions and help identify novel therapeutic targets.

5.5. References

(1) L. G. Griffith,M. A. Swartz, *Nat Rev Mol Cell Bio* **2006**, 7 (3), 211-224.

(2) M. M. Mueller,N. E. Fusenig, *Nat Rev Cancer* **2004**, 4 (11), 839-849.

(3) S. L. Liu,C. Ginestier,S. J. Ou,S. G. Clouthier,S. H. Patel,F. Monville,H. Korkaya,A. Heath,J. Dutcher,C. G. Kleer,Y. H. Jung,G. Dontu,R. Taichman,M. S. Wicha, *Cancer Res* **2011**, 71 (2), 614-624.

(4) A. E. Karnoub, A. B. Dash, A. P. Vo, A. Sullivan, M. W. Brooks, G. W. Bell, A. L. Richardson, K. Polyak, R. Tubo, R. A. Weinberg, *Nature* **2007**, 449 (7162), 557-U4.

(5) Y. Miki, K. Ono, S. Hata, T. Suzuki, H. Kumamoto, H. Sasano, *J Steroid Biochem* **2012**, 131 (3-5), 68-75.

(6) S. Kim, S. E. Ahn, J. H. Lee, D. S. Lim, K. S. Kim, H. M. Chung, S. H. Lee, *Stem Cells* **2007**, 25 (10), 2601-2609.

(7) C. S. Wallace, G. A. Truskey, *Am J Physiol-Heart C* **2010**, 299 (2), H338-H346.

(8) E. Cenni, F. Perut, N. Baldini, *Acta Pharmacol Sin* **2011**, 32 (1), 21-30.

(9) K. J. Edgar, C. M. Buchanan, J. S. Debenham, P. A. Rundquist, B. D. Seiler, M. C. Shelton, D. Tindall, *Prog Polym Sci* **2001**, 26 (9), 1605-1688.

(10) H. Korkaya, S. L. Liu, M. S. Wicha, *J Clin Invest* **2011**, 121 (10), 3804-3809.

(11) S. H. Ku, J. Ryu, S. K. Hong, H. Lee, C. B. Park, *Biomaterials* **2010**, 31 (9), 2535-2541.

(12) E. Azenshtein, G. Luboshits, S. Shina, E. Neumark, D. Shahbazian, M. Weil, N. Wigler, I. Keydar, A. Ben-Baruch, *Cancer Research* **2002**, 62 (4), 1093-1102.

(13) G. Luboshits, S. Shina, O. Kaplan, S. Engelberg, D. Nass, B. Lifshitz-Mercer, S. Chaitchik, I. Keydar, A. Ben-Baruch, *Cancer Research* **1999**, 59 (18), 4681-4687.

(14) H. Korkaya, S. L. Liu, M. S. Wicha, *J Clin Invest* **2011**, 121 (10), 3804-3809.

(15) S. Bergfeld, Y. DeClerck, *Cancer Metastasis Rev* **2010**, 29 (2), 249-261.

(16) A. Nicolini, A. Carpi,G. Rossi, *Cytokine & Growth Factor Reviews* **2006**, 17 (5), 325-337.

(17) J. R. MacDougall, L. M. Matrisian, *Cancer and Metastasis Reviews* **1995**, 14 (4), 351-362.

(18) M. Egeblad, Z. Werb, *Nat Rev Cancer* **2002**, 2 (3), 161-174.

(19) Azenshtein, G. Luboshits, S. Shina, E. Neumark, D. Shahbazian, M. Weil, N. Wigler, I. Keydar, A. Ben-Baruch, *Cancer Research* **2002**, 62 (4), 1093-1102.

(20) P. Mishra, D. Banerjee, A. Ben-Baruch, *Journal of Leukocyte Biology* 89 (1), 31-39.

(21) N. N. Khodarev, J. Yu, E. Labay, T. Darga, C. K. Brown, H. J. Mauceri, R. Yassari, N. Gupta ,R. R. Weichselbaum, *Journal of Cell Science* **2003**, 116 (6), 1013-1022.

국 문 초 록

기능성 고분자박막은 높은 생산성과 가격효율성 측면에서 다양한 분야로의 응용에 많은 주목을 받고 있다. 특히 현대사회에서 요구하는 다양하고 복잡해지는 수요에 부합하기 위해서는 고분자박막 내부의 나노미터 수준의 구조와 물리화학적 성질에 대한 상관관계에 대한 이해가 필수적이라고 할 수 있다. 다양한 형태의 기능성 고분자박막 중에서도, 약물방출플랫폼, 질병진단플랫폼, 조직공학 등과 같은 생의학 분야로의 응용을 위해서는 박막 내부에 삽입된 약물의 방출거동 및 표면에서의 세포거동을 순차적으로 프로그래밍할 수 있는 다층화된 구조가 가장 유리하다고 할 수 있다. 또한, 다층박막을 이용하여 새로운 기능성을 갖는 바이오메디컬 플랫폼을 구현하기 위해서는 실제 응용에 앞서 반드시 세포의 거동을 체외에서 분석하는 것이 필요하다. 이러한 맥락에 비추어, 본 공학박사 학위논문에서는 해리속도 및 해리방식이 조절 가능한 다층박막을 구현하고자, 외부자극에 의한 고분자 다층박막의 물성 및 구조적 특징의 변화를 그 내부를 구성하고 있는 고분자의 특성에 따라 체계적으로 분석하였다. 또한, 새로운 생화학적, 나노구조적 특징을 갖는 다층박막을 설계 및 제조하여 기질박막의 특성 및 공배양되는 기질세포의 종류가 암세포의 거동 및 생화학적 신호체계에 미치는 영향에 대한 연구를 다음과 같이 진행하였다.

제 1 장에서는 다층박막의 외부자극에 따르는 팽창 또는 해리 메커니즘을 나노미터 수준의 내부구조 변화로부터 도출하기 위하여, 중성자반사율장치로 정확한 측정 및 분석이 가능한 모델박막을 구현하기 위한 연구를 수행하였다. 정전기적 인력 기반의 layer-by-layer (LbL) 조립을 하는 경우, 같은 고분자사슬 간 정전기적 반발력이 상대적으로 적은 고분자약전해질이 고분자강전해질보다 다층박막 내부에서 잘 정돈된 계면구조를 보인다는 것을 확인하였으며, 스핀기법이 담지기법보다 외부에서의 흡착을 유도하는 힘들로 인하여 더 잘 정렬된 다층구조를 보인다는 것을 확인하였다. 또한, 외부 습도에 따르는 고분자다층박막 내부의 계면구조변화를 분석해 본 결과, 고분자약전해질로 구성된 다층박막이 고분자강전해질보다 더욱 물 분자를 박막내부로

흡수시키는 경향이 크다는 것을 확인할 수 있었으며, 팽창이 일어나는 과정에서도 그 내부구조를 잘 유지할 수 있음을 확인하였다.

제 2 장에서는 외부 pH 에 매우 빠른 반응속도를 보여 해리속도 및 방출거동을 조절하기 힘든 고분자약전해질 다층박막을 표면에서부터 해리가 일어나는 형태로 구현하고자, 층간 계면의 정전기적 인력의 크기 및 외부 pH 에 대한 의존성을 고분자강전해질과 약전해질의 혼합을 통해 조절하였다. 스핀 LbL 적층법을 통하여 나노미터 수준의 내부구조 변화를 중성자반사율장치를 통해 정밀하게 관찰할 수 있도록 잘 정렬된 내부구조를 갖는 고분자강전해질과 약전해질이 혼합된 모델다층박막을 구현하였다. 이를 기반으로 박막내부에 삽입된 고분자전해질의 혼합비율을 체계적으로 변화시켜가면서 해리되는 다층박막의 내부구조 및 성분변화를 분자적 수준에서 규명함으로써, 고분자강전해질의 계면에서의 강한 깍지낌현상(interdigitation)이 전체적인 다층박막의 해리거동을 제어할 수 있음을 규명하였다.

제 3 장에서는 고분자사슬이 다층박막에서 용액으로 해리되려고 할 때 엔트로피 측면에서의 자유에너지 증가도는 두 고분자 층간 계면 사이의 결합을 이루고 있는 반복단위의 수와 밀접한 관계가 있다는 것을 증명하는 실험을 수행하였다. 이를 위해 고분자약전해질 다층박막의 해리현상을 분자량에 따라 분석하였고, 분자량이 클수록 스핀 LbL 적층법에 의해 다층박막 내부에 제한되어 있던 고분자약전해질 사슬의 입체구조가 본래의 차원 및 크기로 되돌아가면서 해리되는데 소요되는 시간이 커지게 되고, 이 단계로 인해 전체 다층박막의 팽윤현상 및 해리속도가 결정된다는 사실을 처음으로 수정진동자 미세저울을 이용한 소산에너지 분석을 통해 증명하였다. 이러한 연구는 약물방출제어 플랫폼을 구현하기 위해 필수적으로 필요한 다층박막의 해리현상을 결정하는 대표적인 물리적 요인에 대한 체계적 이해를 제공하였다는 데 의의가 있다.

제 4 장에서는 세포가 배양되는 환경에서도 안정적으로 다양한 물리적, 생화학적 인자를 공급해줄 수 있는 스핀 LbL 기반의 다층박막을 이용하여 유방암전이세포(CAMA-1)의 흡착과 탈착, 이동도, 증식도 등에 미치는 환경적 요인에 대한 분석연구를 수행하였다. 정전기적 인력을 기반으로 한 다층박막의 표면치환이

용이하다는 장점을 활용하여, 암전이세포의 흡착과 탈착에 관여하는 대표적인 세포외기질 단백질 (흡착유도: 피브로넥틴(fibronectin), 탈착유도: 에프린 B3(ephrinB3))을 다양한 차원의 구조로 도입하여 그 효과를 살펴보았다. 세포의 흡착과 탈착에 있어서 가장 중요한 요인은 세포막에 있는 인테그린의 군집화로써, 세포외기질 단백질이 다층박막 표면에 2 차원적으로 도포되어 있는 경우보다는 50 nm 크기의 금나노입자 표면에 3 차원적인 구조로 군집화 되어 있을 때 유방암전이세포와 세포외기질사이의 시그널링 및 세포골격계의 발달이 증대된다는 사실을 규명하였다.

제 5 장에서는 높은 수 밀도의 나노기공을 갖는 박막을 이용하여 암전이세포(MDA-MB-231)와 기질세포(fibroblast; NIH-3T3, myoblast; C2C12, human mesenchymal stem cell)로 구성된 독립형 박막구조의 세포시트를 구현하였고, 이를 다층화된 구조로 적층함으로써 암전이세포와 기질세포간의 사이토카인을 이용한 신호전달체계를 분석하였다. 독립형 박막에 나노미터 수준의 크기를 갖는 기공을 도입하고, 기공의 크기 및 박막의 두께를 조절함으로써 암전이세포와 기질세포간의 사이토카인을 이용한 신호전달을 유도할 수 있음을 확인하였고, 이를 통하여 공배양되는 기질세포의 종류가 암전이세포의 증식, 이동도와 생화학적 신호체계에 미치는 영향에 대한 연구를 체계적으로 발전시킬 수 있는 가능성을 제시하였다. 또한, 본 플랫폼의 공학적 응용 및 발전을 위하여, 개발된 박막이 갖는 투명함, 이동가능함의 장점을 부각시켜 세 가지 이상 세포의 공배양 및 세포별 독립적 분석이 가능하다는 것을 확인하였다.

주요어: 고분자 다층박막, 나노구조 조절 및 분석, 중성자 반사율장치, 수정진동자 미세저울, 약물방출 플랫폼, 체외분석법, 유방암전이세포, 세포-기질 상호작용, 세포-세포 상호작용

학번: 2008-21109